ADSORPTION KINETICS OF METHANE REFORMER OFF-GASES ON ALUMINUM BASED METAL-ORGANIC FRAMEWORKS

A Thesis Submitted to
the Graduate School of Engineering and Sciences of
İzmir Institute of Technology
in Partial Fulfillment of the Requirements for the Degree of

MASTER OF SCIENCE

in Materials Science and Engineering

by
Deniz ANGI

July 2017
İZMİR

We approve the thesis of **Deniz ANGI**

Examining Committee Members:

_____
Prof. Dr. Seher Fehime ÇAKICIOĞLU ÖZKAN
Department of Chemical Engineering, İzmir Institute of Technology

_____
Prof. Dr. Günseli ÖZDEMİR
Department of Chemical Engineering, Ege University

_____
Assist. Prof. Dr. Umut ADEM
Department of Materials Science and Engineering, İzmir Institute of Technology

21 July 2017

_____
Prof. Dr. Seher Fehime ÇAKICIOĞLU ÖZKAN
Supervisor, Department of Chemical Engineering
İzmir Institute of Technology

_____
Prof. Dr. Mustafa Muammer DEMİR
Head of the Department of Materials Science and Engineering

_____
Prof. Dr. Aysun SOFUOĞLU
Dean of the Graduate School of Engineering and Sciences

ACKNOWLEDGEMENTS

I would like to express sincere gratitude to my supervisor Prof. Dr. Fehime ÇAKICIOĞLU ÖZKAN for her precious guidance and support, invaluable advices, immense knowledge, endless understanding and motivation throughout my graduate education. I also would like to extend my sincerest thanks to Assist. Prof. Dr. Ufuk ŞENTÜRK for all his valuable recommendations and contributions as co-advisor.

I am thankful to my colleagues; Gaye KANALTI, Canbike BAR and Pınar ÇETİN for their help, generosity and friendship, and Özgün DELİİSMAİL for his support during the entire time.

Thank you to Kaan YALTRIK, for all his endless love, support, belief and encouragement.

Above all, I wish to offer my most heartfelt thanks to my dear family for their unflagging love and unconditional support and encouragement throughout my life, and my sister Pınar ANGI for always being there for me as a friend.

The studies in this thesis was financially supported by the Scientific and Technological Research Council of Turkey (TUBITAK) in the scope of project 112M294.

ABSTRACT

ADSORPTION KINETICS OF METHANE REFORMER OFF-GASES ON ALUMINUM BASED METAL-ORGANIC FRAMEWORKS

Over the last decades, with the development in industrialization, the combustion of fossil fuels has generated an increasing level of emission of greenhouse gases into atmosphere. Considerable efforts have been endeavored to advance alternative cleaner energy source to relieve the stress on environmental concerns and depletion of oil reserves. Hydrogen is regarded as an ideal clean energy carrier. A great majority of ultrapure hydrogen is produced by hydrogen rich steam methane reformer (SMR) off-gas mainly composed of 60-80% H_2, 15-25% CO_2, 3-6% CH_4 and 1-3% CO, which severely requires an efficient separation and purification process associated with gas adsorption principle. A novel class of porous adsorbents known as metal-organic frameworks (MOFs) represent outstanding separation performance due to possessing large surface area and tunable pore size. Aluminum based metal organic frameworks (Al-TPA) are widely utilized in gas separation/purification applications due to its breathing characteristics by adjusting cell volume reversibly. The highest surface area of Al-TPA was found to be 1270 m^2/g by performing solvothermal synthesis route. Diffusion studies of SMR off-gas components on the Al-TPA were carried out at different flow rates (80, 168 and 175 mL/min), temperatures (34, 70 and 100 °C) and concentrations (15 and 28%). High value of parameter L demonstrated that system was under kinetic control. The diffusivity values were found to be ranging from 5.73×10^{-13}-8.04×10^{-13} for CO_2, 5.03×10^{-13}-6.64×10^{-13} for CH_4, 1.36×10^{-12}-1.56×10^{-12} for H_2 and 1.01×10^{-13}- 5.03×10^{-13} m^2/g for CO respectively with increasing temperature.

ÖZET

METAN REFORMER ÇIKIŞ GAZLARININ ALÜMİNYUM ESASLI METAL-ORGANİK AĞ YAPILARI ÜZERİNDE ADSORPSİYON KİNETİĞİ

Son birkaç on yıl içerisinde sanayileşmede yaşanan gelişmelere paralel olarak, fosil yakıtların yakılması, artan bir düzeyde sera gazının atmosfere salınımına yol açmıştır. Çevresel kaygılar ve petrol rezervlerinin tükenmesi üzerindeki stresi hafifletmek amacıyla alternatif temiz enerji kaynaklarının geliştirilmesi konusunda kayda değer çabalar sarf edilmiştir. Hidrojen gazı ideal ve temiz bir enerji taşıyıcısı olarak kabul edilir. Ultra saf hidrojen gazının büyük çoğunluğu gaz adsorpsiyon prensibi ile etkili bir ayırma ve saflaştırma işlemi gerektiren 60-80% H_2, 15-25% CO_2, 3-6% CH_4 ve 1-3% CO oranlarındaki buhar metan reformer (SMR) çıkış gazları kullanılarak üretilmektedir. Yeni geliştirilen metal-organik ağ yapısı (MOF) olarak bilinen gözenekli adsorbentler, geniş yüzey alanına ve ayarlanabilir gözenek boyutuna sahip oldukları için üstün ayırma performansı gösterirler. Nefes alma özelliğiyle ilişkilendirilmiş ayarlanabilir gözenek hacmi sayesinde alüminyum esaslı metal organik ağ yapıları (Al-TPA) gaz ayırma/saflaştırma çalışmalarında yaygın olarak kullanılmaktadır. Bu çalışmada, solvotermal sentez metodu uygulanarak en yüksek yüzey alanına sahip (1270 m^2/g) Al-TPA üretilmiştir. Al-TPA üzerindeki SMR çıkış gazı bileşenlerinin difüzyon çalışmaları farklı gas akış hızlarında (80, 168 ve 175 mL/dakika), sıcaklıklarında (34, 70 ve 100° C) ve konsantrasyonunda (%15 ve %28) gerçekleştirilmiştir. L parameteresinin yüksek değeri sistemin kinetik kontrol altında olduğunu göstermiştir. Difüzivite değerlerinin artan sıcaklık ile birlikte CO_2 için 5.73×10^{-13}-8.04×10^{-13}, CH_4 için 5.03×10^{-13}-6.64×10^{-13}, H_2 için 1.36×10^{-12}-1.56×10^{-12} ve CO için 1.01×10^{-13}- 5.03×10^{-13} m^2/g arasında değiştiği bulunmuştur.

TABLE OF CONTENTS

LIST OF FIGURES

LIST OF TABLES

CHAPTER 1

INTRODUCTION

With the incessant growth of world population and rapid industrialization, the use of fossil fuels has released greenhouse gases which is considered as the major environmental threat through the global warming effect. Fossil fuels include oil used by gasoline engine vehicles, natural gas and machines and the coal used in power plants for supplying electricity. The anthropogenic emissions and combustion of fossil fuels generates an increasing level of carbon dioxide in the atmosphere. Carbon dioxide (CO_2) is the main component of greenhouse gas that contributes 60% to rise in the temperature of the Earth (Ruthven 2006). Environmental concerns and limited oil reserves will involve developing an alternative clean and renewable energy sources for future decades. It is considered that replacing the ingrained combustion engine with modern energy storage technologies including batteries for electrical vehicles and hydrogen based fuel cells (Hirscher et al. 2010). Hydrogen (H_2) is a promising energy carrier and clean fuel in the near future, and widely employed in mobile and portable fuel cell technology especially for transportation applications. It is regarded as one of the most reasonable alternative fuel to fossil resources due to its nonpolluting carbon-free nature, high energy density and its abundancy (Long et al. 2009, Zhou et al. 2012). Hydrogen can be primarily produced from the two consecutive reactions, steam-methane reformation $H_2O + CH_4 \rightarrow 3H_2 + CO$ and water-gas shifting $H_2O + CO \rightarrow H_2 + CO_2$. The resulted hydrogen rich synthetic gas (syngas) is termed as steam methane reformer off-gas, composed of 15-25% CO_2, 3-6% CH_4 and 1-3% CO gases, and hydrogen must be separated from the syngas to yield high-purity hydrogen (Jiang 2009). Herein, concentrating on the upgrading the waste gas into high purity components, the separation/purification of gas stream, and transportation and on-board storage of hydrogen constitute the main issues for commercializing fuel-cell engines (Hirscher and Panella 2005, Sayılgan 2013).

Several methods are available for gas sepearation purification including membrane separation, cryogenic distillation, absorption and adsorption. Increasing demand for high purity gases adsorption technologies for gas separation, which requires

less energy consumption and high efficiency with low cost, has engendered interest in commercial applications (Drioli and Barbieri 2011, Moulijn et al. 2013). The design and operation of this process involves profoundly understanding of the adsorption and diffusion of the SMR-off gas components. Porous adsorbents possessing high selectivity and high adsorption capacity is the key factor for an efficient design and application of adsorptive gas separation (Schneemann et al. 2014). Recently developed hybrid organic/inorganic adsorbents known as metal-organic frameworks (MOFs) have attracted great deal of attention due to their unprecedented features. MOFs are crystalline coordination polymers composed of inorganic metal cluster and organic linker. Possessing high surface area, tunable pore size and structural robustness MOFs present unique performance in adsorption based applications such as gas storage, gas purification, catalyst and sensor (Baiker et al. 2010, Bajaj et al. 2010, Rodrigue et al. 2012, Miljanić et al. 2014). Aluminum based metal organic frameworks (Aluminum terephthalate, Al-TPA) are one of the commercially avaliable MOFs have been widely utililized due to its large pore diameter of 0.85 x 0.85 nm, surface area of 1600 m^2/g, high thermal stabilities and unique breathing properties providing tunable pore structure. Aluminum terephthalate, constructed from $AlO_4(OH)_2$ octahedra clusters interconnected by benzene-1,4-dicarboxylate groups, was synthesized in three main steps, crystallization, purification and activation, under hydrothermal or solvothermal conditions (Loiseau et al. 2004, Baiker et al. 2010).

Thermodynamic and kinetic parameters including Henry's constant and diffusion coefficient must be emphasized for the development of adsorptive separation processes. Zero-length column (ZLC) method has been widely carried out in a simple and efficient manner to estimate such parameters surpassing the external mass transfer resistance and heat effects (Hirscher and Panella 2005, Trens et al. 2008). Through this work the optimum conditions for the synthesis of aluminum terephthalate were determined by altering the synthesis conditions to obtain aluminum terephthalate possessing high surface area and reasonable crystal structure. As adsorption kinetics and diffusion studies on MOF adsorbent are very limited in literature, this study also aims to investigate the effects of temperature, flow rate and concentration on the diffusion behaviour of the components of steam methane reformer off-gas (CO_2, CH_4, H_2 and CO) on the aluminum terephthalate and estimate the influence of such experimental conditions on Henry's constant and diffusion coefficient of gas components.

This study comprehend the information on MOFs and aluminum terephthalate (Chapter 2), adsorption kinetics and ZLC technique (Chapter 3), experimental studies (Chapter 4), results and discussions (Chapter 5) and conclusion (Chapter 6).

CHAPTER 2

METAL-ORGANIC FRAMEWORKS (MOFs)

Over the past decade, porous adsorbent materials including activated carbon, zeolites, MOFs, silica gel and activated alumina have been proposed for adsorptive separation and purification processes (Mandal et al. 2014). Among these adsorbents MOFs have attracted considerable attention as a promising porous adsorbent due to their unique properties (Ahn et al. 2012). This chapter summarized the properties and application of MOFs, and especially aluminum based MOF (aluminum therephthalate (Al-TPA)) which is produced in this study.

2.1. Properties of MOFs

MOFs, also known as crystalline coordination polymers, have emerged as an interface between molecular coordination chemistry and material science. They possess several important characteristics such as large pore volume, high porosity, tunable pore size, extremely high surface area (up to 10,500 m^2/g), and good adsorption capacity (Saha and Deng 2010, Farha et al. 2012). Beside these substantial properties, MOFs have dynamic behavior and structural flexibility in which reversible expansion or contraction take place in the presence of external stimuli, such as pressure or guest molecules, and can reversibly alter their pore dimensions. The surface area and pore volume of MOFs are much higher than that of zeolite (Shadid 2015). Most of MOFs, however, have lower thermal and hydrothermal stability as compared to zeolites (Pearce 2009).

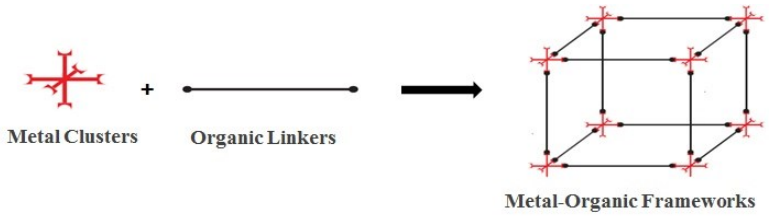

Figure 2.1. Basic illustration of the formation of MOF structure.

MOFs are hybrid organic-inorganic materials constructed from inorganic metal clusters linked together via organic linkers to form one (1D), two (2D) and three (3D) dimensional network structure (Figure 2.1) (Loiseau et al. 2004). Inorganic linker part of the structure offers thermal and mechanical stability, chemical functionality or electronic or optical properties whereas organic part of the structure provides properties related with shape (i.e., potential ligand coordination angle), size (i.e., expansion of a ligand) and sorption properties (Eubank 2008). The great variety of organic ligands and metal ions yield a range of different possible combination of network composition and structure with distinctive features, in that there are 10,000 experimentally known MOF types in literature (Farha et al. 2012). The first row transition metal ions such as Zn(II), Cu(II), Co(II), Cd(II), Ti(III), etc. and other metals including Mg(II), Ca(II), Ln(III), Al(III), Zr(IV), etc. are commonly used for the synthesis of MOFs. The functional group of the organic ligands commonly used in the synthesis of MOFs are mostly O or N donors such as carboxylates, amines, cyanides, pyridines, imidazoles, phosphonates and sulfonates (Manos et al. 2017). Ligands with carboxylate functional group is the most common organic ligand used in the construction of MOFs due to its stable and rigid characteristics. Multitopic linkers (i.e. possessing two or more functional groups) with rigid carbon backbones (i.e. aromatic or alkenyl chains with double bonds) also provide stable and durable framework that retain its integrity upon exchange of guest molecules (Pham 2013, Shadid 2015). The flexible organic linkers such as polytopic ligands cause unstable and undesired flexible frameworks which result in losing crystallinity, changing their morphology or experiencing a phase change in the absence of guest molecules (Eubank 2008). MOFs structure produces by these ligands can also be complicated by dense packing or interpenetration. The functional groups of ligands coordinate with the metal ions and creates clusters with two or more metal atoms called as secondary building units (SBUs). The coordination number and geometry of the metal ions and the type of the functional groups determine the geometry of the SBUs. Each SBU connects with each other to carbon backbones of the ligand to create a network structure. The SBUs can adopt different types of coordination geometry such as tetrahedral, octahedral, trigonal bipyramidal, square, and pyramidal (Pham 2013). An almost unlimited number of MOF structures with distinctive topology and properties such as porosity, pore structure and rigidity can be built up by the coordination of great diversity of metal-containing SBUs with different type of ligand build up. For instance, starting with 1,4-benzenedicarboxylic

acid organic linker a variety of MOF structure, aluminum terephthalate (Al-TPA), copper terephthalate (Cu-TPA), titanium terephthalate (Ti-TPA) and zinc terephthalate (Zn-TPA) can be produced by using different metal sources (Table 2.1).

Table 2.1. MOF structures composed of 1,4-benzenedicarboxylic acid organic linker and different metal sources.

Metal Source	Organic Linker	MOFs
Aluminum Nitrate Nonahydrate ($Al(NO_3)_3•9H_2O$)	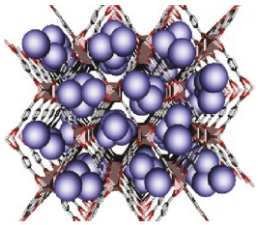 (1,4-benzenedicarboxylic acid)	**Al-TPA** **(Mota et al. 2011)**
Copper(II) Nitrate Trihydrate ($Cu(NO_3)_2•3H_2O$)		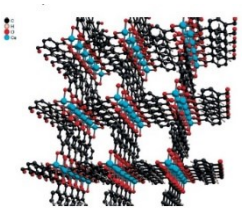 **Cu-TPA** **(Carson et al. 2009)**
Titanium Isopropoxide ($Ti(O\text{-}i\text{-}Pr)_4$)		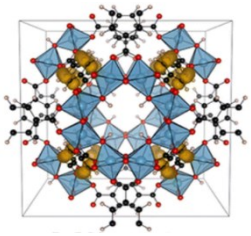 **Ti-TPA** **(Walsh et al. 2013)**
Zinc Nitrate Hexahydrate ($Zn(NO_3)_2•6H_2O$)		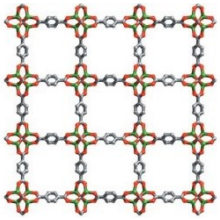 **Zn-TPA** **(Banerjee et al. 2014)**

Adsorption or separation mechanism for MOFs based on two types, size/shape exclusion or adsorbate-surface interactions. Size and shape exclusion, also known as steric separation, in which certain components of a gas mixture are blocked out from the pores of the MOF whereas other components are adsorbed in the pores. In addition to size exclusion, interaction between the adsorbate molecule and the MOF structure results in preferential adsorption of one component over others in a gas mixture. Adsorption behavior and selectivity are related with the type and solubility of gas molecules,

thermodynamic affinity, quadruple moment, polarity, H-bonding, van der Waals interaction and π-π interaction (Shadid 2015).

2.2. Aluminum based Metal Organic Frameworks (Al-TPA)

Aluminum based metal organic frameworks or aluminum terephthalate was first developed by Materials of Institute Lavoisier and designated as MIL-53(Al). Compared to other MOFs, having better thermal (up to 500°C) and sructural stability, higher surface area and larger pores, Al-TPA become a promising adsorbent for adsorptive applications (Arstad et al. 2008, Ruthven 1984).

Aluminum, which is the most abundant element in the Earth's crust, is commonly found in the form of gibbsite, $Al(OH)_3$, and boehmite, AlO(OH). Aluminum salt which is used in the synthesis of Al-TPA can be obtained by acid leaching of metallic aluminum or $Al(OH)_3$. In the hydrothermal synthesis of Al-TPA, aluminum presents as $Al(H_2O)_6^{+3}$ ion in the aqueous solution and the water molecules of $Al(H_2O)_6^{+3}$ ion is replaced to form $AlO_4(OH)_2$ centers (Loiseau et al. 2004). Al-TPA has large pore diameter of 0.85 nm and specific surface area up to 1600 m^2/g (Rodrigue et al. 2012). The Al-TPA framework structure was indicated in Figure 2.2. Al-TPA framework is composed of chains of trans corner sharing $AlO_4^-(OH)_2$ octahedra via OH bridges interconnected by benzenedicarboxylate (BDC) ligands; namely, trivalent Aluminum metal atom is coordinated to four oxygens from 1,4-benzenedicarboxylates and two oxygens from the trans bridging μ2-hydroxyl groups, which results in 3D framework containing 1D diamond shaped tunnels along [001] direction (Mandal et al. 2014, Calleja et al. 2017).

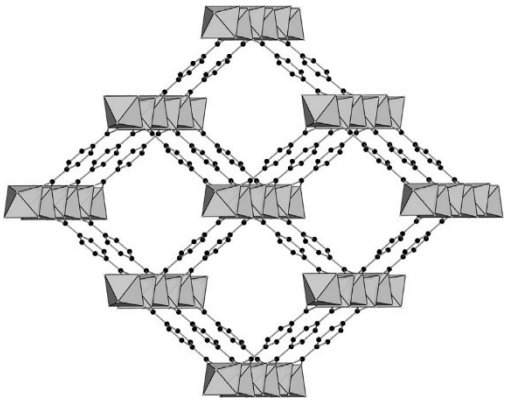

Figure 2.2. Framework structure of Al-TPA
(Source: Reinsch and Stock, 2013).

Al-TPA have become much exciting due to its flexible structure, good stability and breathing character. It can arrange its cell volume up to 40% reversibly to increase the interactions between the guest molecules and the host framework with no evidence of loss of crystallinity or bond breaking (Denayer et al. 2009). Structural transformation of Al-TPA framework from large pore (lp) domain to the narrow pore (np) domain (lp →np) and vice versa by adsorption of guest molecule, or by changing temperature or pressure. This is called breathing phenomena (Ahn et al. 2012). The strength of the hydrogen bonding of metal backbone, the ionic radii or electronic structure of metal and hydroxyl groups of framework can also affect the structural breathing behavior. The effect of the breathing on the structure of Al-TPA framework was indicated in Figure 2.3. The tunnels of Al-TPA which are occupied by unreacted BDC molecules possess free dimensions of 7.3 x 7.7 $Å^2$ (Figure 2.3.a). Entrapped molecules can be reversibly removed upon heating to high temperature and fully open large pore structure having 8.5 x 8.5 $Å^2$ channel dimensions (Figure 2.3.b). At room temperature water molecules trapped into these tunnels through the hydrogen bonding between water and the hydrophobic part of the aromatic walls of the tunnels, that is narrow pore domain is satisfied and the pore dimensions become 2.6 x 13.6 $Å^2$ (Figure 2.3.c) (Loiseau et al. 2004). Upon cooling to 5 K or upon rehydration the structure of Al-TPA also returns to its closed narrow pore form. In this case, the transformation from lp domain to np domain decreases the cell volume of Al-TPA by 35%. The large pore structure is more stable than narrow pore structure (Ahn et al. 2012, Mandal et al. 2014).

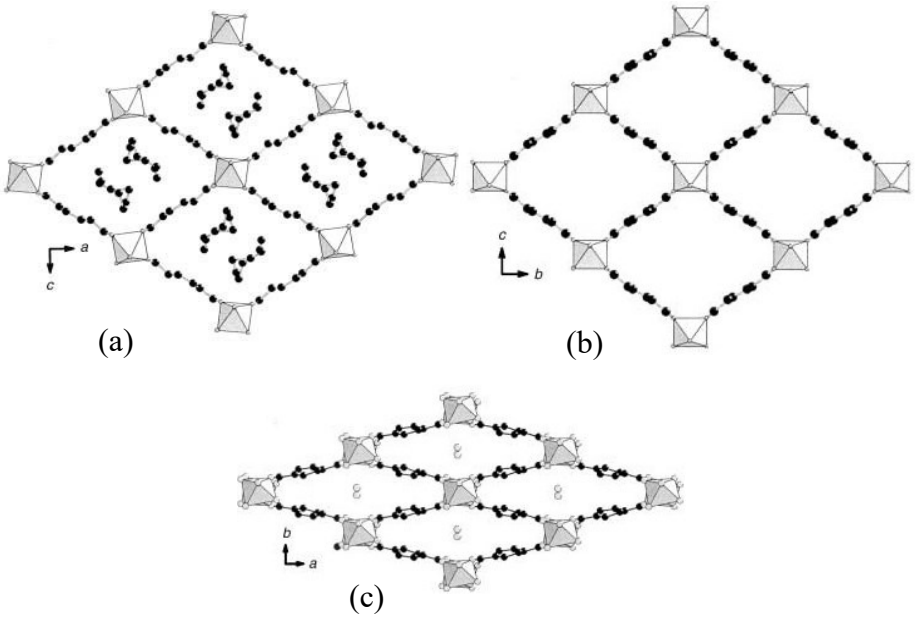

Figure 2.3.The channel system of Al-TPA framework a) The pores of Al-TPA are occupied by free BDC b) Al-TPA with empty and large pore at high temperature c) The pores of Al-TPA are occupied by water molecules at room temperature (narrow pore). (Gray octahedra represents $AlO_4(OH)_2$, and gray and black circles oxygen and carbon, respectively) (Source: Loiseau et al., 2004).

Methane adsorption can also be increased at or above room temperature, where lp domain is favored, over the whole pressure range (Hadjiivanov et al. 2016). In addition to temperature, changing the pressure can also affect the adsorption behavior of Al-TPA. At lower pressure (0-0.8 bar) where np domain predominates, the adsorption capacity and selectivity of CO_2 over N_2, CH_4, CO and O_2 is enhanced whereas at higher pressure of 1-8 bar where lp form predominates, the CO_2 uptake is increased. The selectivity and adsorption capacity of different guest molecules can be enhanced by designing an appropriate pressure or temperature (Yan et al. 2015).

2.2.1. Synthesis Methods of Al-TPAs

MOFs can be alternatively synthesized by several methods including solvothermal methods, hydrothermal methods, microwave-assisted synthesis, sono-chemical synthesis, microwave assisted method, slow evaporation method, electrochemical and mechanochemical procedures (Hartmann et al. 2009, Manos et al.

2017). The are three main steps, crystallization, purification and thermal activation in the synthesis of MIL-53(Al) accomplished by hydrothermal, solvothermal and hydro-solvothermal synthesis methods (Ahn et al. 2012) as explained in the Chapter 4.

The hydrothermal synthesis of MIL-53(Al) was first introduced by Loiseau et al. (2004) using Aluminum nitrate nonahydrate, $Al(NO_3)_3.9H_2O$ as aluminum source at 220 °C for 72 h (with molar composition of 1 Al:0.5 BDC:80 H_2O). The effect of activation on Al-TPA samples synthesized by hydrothermal synthesis procedures mentioned above were summarized in Table 2.2. The disadvantage of this synthesis is the energy and time consumption during purification; removal of BDC molecules from the pores of the structure. In the procedure of Loiseau et al. (2004) calcination of Al-TPA was applied. However, this problem can be overcome by alternative methods such as solvent extraction and then solvent exchange or calcination. Utilization of alumina, aluminum hydroxide or boehmite instead of aluminum nitrate decreases the BET surface area Al-TPA as stated by Li et al. (2015).

Table 2.2. Hydrothermal synthesis studies of MIL-53(Al) in literature.

References	Activation	Metal Source	BET surface area (m^2/g)
Loiseau et al. (2004)	Thermal at 330 °C for 72 h	$Al(NO_3)_3.9H_2O$	1140
Liu et al. (2008)			1270
Huang et al. (2013)			1294
Li et al. (2015)	Solvent (DMF) extraction and exchange	Al_2O_3, $Al(OH)_3$, AlO(OH), $Al(NO_3)_3.9H_2O$	905
Rallapalli et al (2010)		$Al(NO_3)_3.9H_2O$	1235
Gumma et al. (2013)		$Al(NO_3)_3.9H_2O$	1284
Mandal et al. (2014)			
Somani et al. (2011)		$Al(NO_3)_3.9H_2O$	1235

The solvothermal synthesis method proposed by Rodrigue et al. (2012) using N,N-dimethylformamide (DMF) instead of water as solvent. Using 1,3,5-tris[40-carboxy(1,10-biphenyl)-4-yl] benzene (TCBPB) as organic linker enhances the BET surface area up to 2311 m^2/g (Saha et al. 2012). The solvothermal synthesis of Al-TPA

synthesized in this study yields 1270 m^2/g, which is slightly lower than the results of Rodrigue et al. (2012). The effect of organic linker on Al-TPA synthesized by solvothermal studies were tabulated in Table 2.3.

Table 2.3. Solvothermal synthesis studies of MIL-53(Al) in literature.

References	Organic Linker	BET surface area (m^2/g)
Rodrigue et al. (2012)	TPA	1365
Saha et al. (2012)	TCBPB	2311

Decreasing the amount of DMF solvent Kaliaguine et al. (2011) proposed a new hydro-solvothermal synthesis method using both DMF and water lowers the BET surface area to 950 m^2/g. By increasing the amount of the starting materials and decreasing the crystallization temperature, the BET surface area was increased to 984 m^2/g (Zhu et al. 2016). Increasing thermal activation temperature slightly decreases the BET surface area of MIL-53(Al) to 931 m^2/g (Zhou et al. 2013). Instead of calcination step, washing with methanol solvent enhances the BET surface area to 1071 m^2/g in the study of Liu et al. (2016). The procedure stated by Kaliaguine et al. (2011) was followed and yield approximately 730 m^2/g in this study. Hydro-solvothermal studies using dmf/water were summarized in Table 2.4.

Table 2.4. Hydro-solvothermal synthesis studies of MIL-53(Al) in literature.

References	Investigated Effect	BET surface area (m^2/g)
Kaliaguine et al. (2010)	Hydro-solvothermal synthesis	950
Zhu et al. (2016)	Amount of starting material	984
Zhou et al. (2013)	Activation temperature	931
Liu et al. (2016)	Washing step	1071

2.3. Applications of MOFs

MOFs have been utilized for various kind of applications including gas storage, catalysis, sensing, drug delivery and clean energy (Della Rocca et al. 2011). The potential clean transportation fuel sources in the near future are considered as methane and hydrogen. The storage and transportation of hydrogen and methane are the most challenging task for fuel cell applications. MOFs constitute extremely large storage capacity for hydrogen and methane via physisorption (Rosi et al. 2003, Hirscher and Panella 2005, Bajaj et al. 2010). Ferey et al. (2003) reported MIL-53(Al) having hydrogen adsorption capacity of 3.8 wt% at 16 bar and 77 K. Methane storage capacity on MIL-53(Al) was determined as 158 cm^3/cm^3 at 303 K and 35 bar (Bajaj et al. 2010, Yaghi et al. 2014). Beside storage studies, MOFs are widely used in the separation of different gases. Gumma et al. (2013) investigated the structural transformation of MIL-53(Al) from large pore to narrow pore form to enhance the CO_2 adsorption capacity for the pressure range of 1-8 bar. Ferreira et al. (2014) investigated the CO_2/CH_4 separation using the MIL-53(Al) tablets provided by BASF Basolite A100 which showed a CO_2 adsorption capacity of 4.3 mol/kg at 3.5 bar (Ferreira et al. 2015).

MOFs are recently served as **catalysts** due to their uniform and tunable pores, large internal surface area, flexibility and stability (Verpoort et al. 2015). Unsaturated metal sites found in MOF enable them to be used in catalytic reactions. Diversity in MOF types also is a virtue for size and shape selective catalysis (Timofeeva et al. 2017). Calleja et al. (2017) studied the effect of ratios of organic ligands on the catalytic activity of amino-based MIL-53(Al). Miao et al. (2017) synthesized Bronsted acid catalyst (Al-MIL-53-RSO3H) derived from the reaction of amino based MIL-53(Al) for the production of secondary amine products. Corma et al. (2012) compared the three types of Copper-based MOF for the production of indoles and imidazopyridines, proved that copper terephthalate, Cu(BDC), indicated the best performance as a catalyst by preventing the side reactions. MOFs based on different metal souces (Nickel and Indium) were also utilized in the reduction of nitroaromatics and oxidation of sulfides (Monge et al. 2017, Truong et al. 2017).

Purification of water and water reuse from **wastewater** is the most attractive treatment to overcome water stress issues. Wastewater contains many organic contaminants stemmed from industrial including dyes, phenols and nitrobenzene,

agricultural including herbicides and pesticides, and pharmaceutical waste stream. MOFs interact with those organic contaminants via pore size and shape selectivity, hydrophobicity/hydrophilicity, π-π interaction (Dias and Petit 2015). Somani et al. (2011) utilized MIL-53(Al) for the removal of nitrobenzene through such interactions. Moreover, Jhung et al. (2015) studied the liquid-phase adsorption of such several contaminants from water using chromium based MOF, MIL-101.

MOFs having **luminescent** properties also serve as chemical sensor since they can readily accomodate guest molecules into its pores. Owing to their different functional groups, MOFs can selectively detect and remove even very low levels of toxic heavy metals such as Hg^{+2}, Pb^{+2}, Cd^{+2}, As^{+3}, organic dyes including methylene blue, methyl orange and RhodamineB, pollutants such as CrO_4^{2-} and $Cr_2O_7^{2-}$ ions and visible light emitting lanthanide cations such as Tb^{3+} ions from water with high sensitivity (Yi et al. 2015, Li et al. 2016). MOFs can be utilized as biosensor to detect immune deficiency, as an electrode material having redox activity or integrated with electronic chemiresistive sensor array (Chen et al. 2015, Dincă et al. 2015, Zhang et al. 2017).

MOFs have been recently utilized in **Lithium ion batteries, supercapacitors and fuel cells, or energy conversion** devices. They have been used as anode material in LIBs by serving as self-sacrificing template providing large lithium storage capacity due to their large porosity and rigidity (Bu et al. 2015, Wang et al. 2015). MOFs have been also used as electrode in supercapacitors by fabricating on carbon cloth or as a support for electrocatalyst for ethanol oxidation which has offered increased electrochemical activity and enhanced fuel cell performance (Wang et al. 2015, Nadeem et al. 2016).

Nanoscaled MOF types containing biocompatible content have recently developed for **biomedical** applications including drug delivery. Owing to their large internal surface area and tunable pore volume, MOFs can readily accomodate various kind of drug molecules into its porous framework. MOFs constitute an effective nest for anticancer and anti-inflammatory drug (Damirin et al. 2017). Serre et al. (2008) produced flexible nanoporous chromium or iron terephthalates, (BDC) MIL-53(Cr,Fe), to be used in the adsorption of Ibuprofen. Stoddart et al. (2017) studied the Ibuprofen loading in the cyclodextrin based MOF (CD-MOF(K)). Long et al. (2016) introduced mesoporous MOF with different metal sources (Mg, Fe, Co, Ni and Zn) for the loading of olsalazine anti-inflammatory and anticancer drug (86%).

CHAPTER 3

GAS ADSORPTION

The adsorption phenomena is mainly adopted in this chapter. To properly understand a gas adsorption process, equilibrium and kinetic mechanisms should be considered. The gas adsorption equilibrium deals with the ability of material to hold preferentially different components of a system, which is one of the essential mechanism for understanding the adsorption capacity of a solid adsorbent. The gas adsorption kinetic process of single or multicomponent systems can be described by adsorption diffusion models correlated with diffusional resistances. Either macropore or intracrystalline diffusion resistances may control the transport behavior of a system depending on the particular system and the conditions. Zero Length Column (ZLC) technique have been developed to study the diffusion properties of gases in porous adsorbents.

3.1. Principles of Adsorption

Adsorption is essentially a surface phenomenon involving accumulation of a gas or liquid stream on the surface of solid phase, which arises due to the presence of residual (unbalanced) forces at the surface of solid. The atoms at the surface, which possess residual forces (surface energy), are not wholly surrounded by atoms above them and can readily accommodate the adsorbate atoms. Contacting with the surface the residual forces that are responsible for the interactions between the adsorbate molecules and the adsorbent surface are satisfied by attracting and retaining the molecular species. The coordinatively unsaturated surface atoms of a solid become saturated by the interactions of the molecules of the environment. During adsorption the residual forces on the surface tend to decrease, i.e. the surface energy decreases which appears as heat. Adsorption therefore is an exothermic process and the enthalpy (ΔH) of adsorption is always negative. When gas molecules are adsorbed since the movement of the gas molecules are restricted the entropy (ΔS) of the adsorption process also decreases i.e ΔS is negative.

Molecules which is actually adsorbed onto the solid surface are known as *adsorbat*e and the substance on the surface of which the adsorption takes place is referred to as *adsorben*t. The molecule in gas phase is capable of being adsorbed is *adsorptive*. The adsorbed phase can be released by *desorption*. The adsorption system was given in Figure 3.1. The nature of the interaction between adsorbate and adsorbent dictates the type of the adsorption, namely, physical adsorption (physisorption) and chemical adsorption (chemisorption).

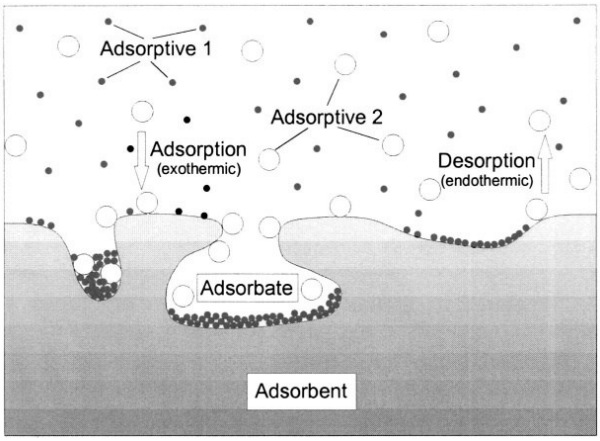

Figure 3.1. Basic concepts of adsorption phenomena
(Source: Keller and Staudt, 2005).

For physical adsorption, the gas molecules are held on the surface of solid on account of weak Van der Waals forces (dispersion-repulsion forces), which are fundamental property of all matters, supplemented by electrostatic contributions (field-dipole, polarization and field gradient-quadrupole interactions) hence it is not specific to any gas or adsorbent. Not involving chemical bond formation physical adsorption has low enthalpy of adsorption, about 20-40 kJ/mol. Multilayer adsorption is common. Physical adsorption of a gas by solid is reversible. As the physical adsorption is an exothermic process and does not involve exceeding the activation energy, it can readily take place at low temperature. Increasing the pressure results more gas to be adsorbed as the volume of gas decreases according to Le-chatelier's principle. The adsorbed gas can be easily desorbed either by decreasing the pressure or by increasing the temperature.

Chemical adsorption involves chemical bonding (covalent or ionic) between adsorbate gas and the adsorbent by electron sharing or electron transfer. Enthalpy of

adsorption is therefore high, about 40-400 kJ/mol. Due to the high enthalpy of adsorption and activation energy higher temperature favors the amount of gas adsorbed. Chemical adsorption depends on the chemical nature of the substances and is highly specific that occurs only when there is possibility of chemical bond between the adsorbate and adsorbent. It results into monolayer coverage of the solid surface. As chemical adsorption requires bond formation, it is usually irreversible in nature. Gas adsorbed at low temperature by physical adsorption can be then adsorbed by chemical adsorption at higher temperature (Madan 1999, Keller and Staudt 2005, Karge and Weitkamp 2008).

3.2. Gas Adsorption Equilibrium

Gas adsorption equilibrium is generally described by adsorption isotherms that indicates the amount of gas adsorbed by adsorbent as a function of gas phase concentration or partial pressure.

The Langmuir isotherm reduces to Henry's Law isotherm at very low adsorbed gas phase concentration limit or at very low pressure that is the adsorption isotherm for physical adsorption approaches linearity. The linear region is known as the Henry's Law region and the constant of proportionality, or the limiting slope, between the amount of gas adsorbed and gas phase concentration of the equilibrium line is known as Henry's constant (K) given in Equation 3.1,

$$\lim_{c \to 0} (\partial q / \partial c)_T = K \tag{3.1}$$

$$\lim_{p \to 0} (\partial q / \partial p)_T = K' \tag{3.2}$$

The relationship between two constants considering Equation 3.1 and 3.2 yields Equation 3.3,

$$K = (RT)K' \tag{3.3}$$

The Henry's constant is therefore the thermodynamic equilibrium constant and it corresponds to van't Hoff temperature dependence is stated in Equation 3.4 and 3.5.

$$K = K_{\infty} e^{-\Delta U/RT} \tag{3.4}$$

$$K' = K'_{\infty} e^{-\Delta H/RT} \tag{3.5}$$

ΔU and ΔH are internal energy change and enthalpy change for adsorption at low loading concentration, respectively.

At higher solute loadings beyond Henry's Law region the equilibrium isotherms which become curved are generally in the Type I form of Brunauer's classification, and the amount adsorbed attains the saturation capacity at high partial pressure, that is the surface of adsorbent is fully covered by adsorbate molecules (monolayer coverage). The Langmuir isotherm, the basic and most used adsorption model, explains the monolayer gas adsorption on homogeneous flat surface on the basis of kinetic consideration. It is stated that the rate of adsorption equals to the rate of desorption at equilibrium. The basic assumptions for the Langmuir model are: 1. Homogeneous surface where all adsorption sites are energetically identical; 2. Molecules or atoms are adsorbed at definite, localized sites; 3. Each site can hold only one atom or molecule (Monolayer coverage); 4. No interaction between the adsorbed molecules. The ideal Langmuir expression is given in Equation 3.6.

$$\Theta = \frac{q}{q_s} = \frac{bc}{1+bc} = \frac{b'p}{1+b'p} \tag{3.6}$$

q_s represents the saturation capacity, Θ is the fractional coverage, p is the pressure and b (and b′) is the affinity constant related with Henry constant by bq_s=K (and $b'q_s$=K′).

The extension of the Langmuir Model assuming the multilayer adsorption yields the Brunauer, Emmett, and Teller isotherm with the following assumptions: 1. Adsorbed molecules are localized on their adsorption sites; 2. Gas molecules are adsorbed on a solid in layers infinitely; 3. No interaction between each layer; 4. Langmuir theory can be applied to each layer. These assumptions lead to the following BET expression stated in Equation 3.7.

$$\frac{q}{q_m} = \frac{b(\frac{p}{p_s})}{\left(1-\frac{p}{p_s}\right).\left(1-\frac{p}{p_s}+\frac{b.p}{p_s}\right)} \tag{3.7}$$

q_m is the amount adsorbed monolayer and p_s is the saturation vapor pressure of adsorbate (Do 1998, Brandani 2002, Karge and Weitkamp 2008).

3.3. Gas Adsorption Kinetics

Studying the gas adsorption kinetic properties of a system is essential for the rational design and optimization of adsorptive separation processes. Before considering the kinetic behavior in detail an understanding of basic diffusion theory is essential background for gas adsorption kinetic studies. The overall rate of gas adsorption is controlled by diffusional resistances associated with mass or heat transfer instead of intrinsic adsorption kinetics at the active surface since the intrinsic rate of physical adsorption at a surface is generally rapid. Many adsorbents have bimodal pore size distribution which is made from small particles of the microporous solid formed into macroporous particles. Such biporous adsorbent offers three distinct resistances to mass transfer: external fluid film diffusion, diffusion through the macropores of the formed particles, diffusion through the intracrystalline micropores (Figure 3.2). The relative magnitude of these resistances are correlated with the particular system and the conditions.

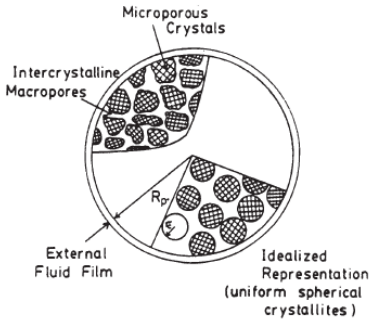

Figure 3.2. The schematic representation showing the three principal resistances to mass transfer in a porous adsorbents. (Source: Rodrigues et al., 1989).

3.3.1. Fundamental Principles of Diffusion

Diffusion is related to the random (Brownian) motion of molecules which leads to a net flux down the concentration gradient of different nonuniform molecules.

Molecular transport is correlated with the diffusion coefficient or transport diffusivity (D) defined in accordance with Fick's first equation stated as Equation 3.8 where z is the spatial coordinate.

$$J = D\frac{\partial q}{\partial z} \tag{3.8}$$

However, regarding thermodynamic considerations the actual driving force for molecular transport has been approved as the gradient of chemical potential in Equation 3.9.

$$J = -B_q\frac{\partial \mu}{\partial z} \tag{3.9}$$

The chemical potential for an ideal vapor phase is stated in Equation 3.10.

$$\mu = \mu_0 + RTlnp \tag{3.10}$$

Combining the Equation 3.8, Equation 3.9 and Equation 3.10 the expression for the flux (J) can be written as in Equation 3.11.

$$J = -BRT\frac{d\ lnp}{d\ lnq}\frac{dq}{dz} \tag{3.11}$$

Equation 3.12 defines the transport diffusivity.

$$D = BRT\frac{d\ lnp}{d\ lnq} = D_0\frac{d\ lnp}{d\ lnq} \tag{3.12}$$

$D_0 = BRT$ is the corrected or intrinsic transport diffusivity and $d\ lnp/\ d\ lnq$, known as thermodynamic correction factor, represents the gradient of the equilibrium isotherm in logarithmic coordinates. Within Henry's law region at low concentration regime (where $q \propto p$) $d\ lnp/\ d\ lnq \rightarrow 1.0$ and $D = D_0$. This simple Fickian approach with constant diffusivity has been valid for the systems near the saturation limit or for the low loadings (diluted gas system with low partial pressure) where the interaction between

diffusing molecules is negligible. However at higher loadings the system approaches to saturation limit and follows the Langmuir isotherm as in Equation 3.13, and diffusivity therefore become dependent on the concentration.

$$D = \frac{D_0}{1-q/q_s} \tag{3.13}$$

Equation 3.13 indicates that the Fickian diffusivity approaches infinity as the saturation limit approaches ($q \rightarrow q_s$) and $d\ lnp/\ d\ lnq \rightarrow \infty$ for this region.

Moreover, the temperature dependence of diffusivity is described by Arrhenius equation given in Equation 3.14 which also yields diffusional activation energy (E_a).

$$D = D_\infty e^{-E_a/RT} \tag{3.14}$$

For self-diffusion (tracer diffusion), there is no concentration gradient of species, it is defined by monitoring the migration of isotopically marked molecules. The self-diffusion may also occur via random migration. The microscopic situations of diffusion phenomena was illustrated in Figure 3.3 (Rodrigues et al. 1989, Karger and Ruthven 1992, Lee 2003, Karge and Weitkamp 2008).

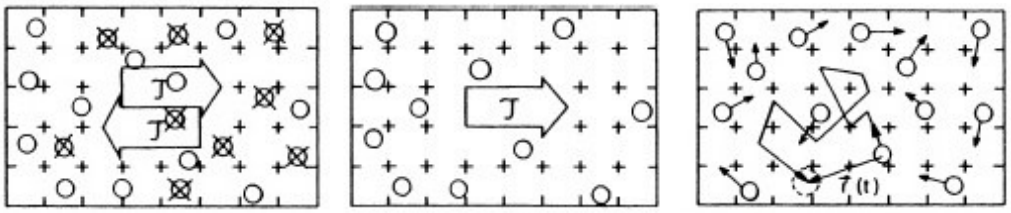

(a) (b) (c)

Figure 3.3. Schematic diagram representing a) tracer diffusion b) transport diffusion c) self-diffusion (Brownian motion) (Source: Karge and Weitkamp, 2008).

3.3.2. Diffusional Resistances in Porous Media

According to the International Union of Pure and Applied Chemistry (IUPAC) classification, the porous adsorbents are classified as followed: micropores (d < 2 nm), mesopores (2 nm < d < 50 nm) and macropores (50 nm < d). Internal diffusional

resistances in porous media can be evaluated by the diffusion mechanism including viscous flow, molecular diffusion, Knudsen diffusion, surface diffusion and intracrystalline diffusion, related to the pore size range (microporous, mesoporous and macroporous), and dominated by the different types of forces (Figure 3.4) (Kärger et al. 2012).

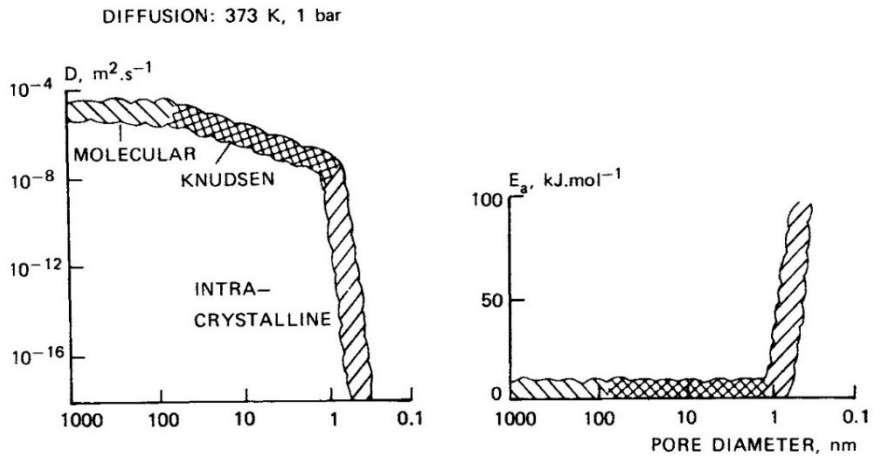

Figure 3.4. The influence of pore diameter on diffusivity and activation energy for diffusion regimes (Source: Ruthven, 2001).

Macropores play important role in transport properties and contribute very little to adsorption capacity. The main mechanisms within the macropore range, or in larger pores, are viscous flow and molecular diffusion (Figure 3.5). Molecular diffusion is predominant transport mechanism in macropore solids with large pore diameters which is much greater than the mean free path, or the average distance travelled between molecular collisions, of the molecules (Figure 3.4). Collisions between the molecules occur more frequently than collisions with the pore wall. Viscous flow is due the difference in total pressure across a particle. The fluid mixture hence flow through the larger pores as a bulk without separation at the same speed.

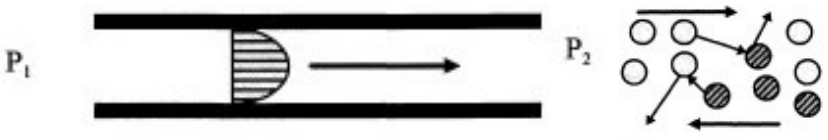

(a) (b)

Figure 3.5. The mechanism of a) viscous flow b) molecular diffusion (Source: Do, 1998).

On the other hand, capillary forces become important within the mesopore range where Knudsen and surface diffusion become dominant with the decrease of pore size (Figure 3.4). As the pore diameter is small relative to the mean free path, Knudsen diffusion arises due to the collision of gaseous molecules with the wall of the porous medium (Figure 3.6). The molecules do not interact with each other as molecules collide more frequently with pore walls than with diffusing molecules. The driving force for the Knudsen diffusion is the concentration gradient. The flow depends on the molecular weight of the diffusing species. Surface diffusion is based on the different mobility of different molecules on the surface of pore walls due to their different extent of interaction with the surface (Figure 3.6). The strongly adsorbing species preferentially cross the pore network by jumping from site to site.

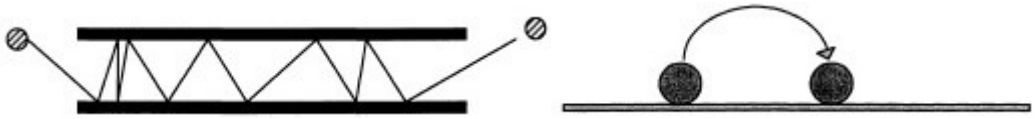

(a) (b)

Figure 3.6. The mechanism of a) Knudsen diffusion b) Surface diffusion (Source: Do, 1998).

Diffusion within micropore range has been variously termed as configurational diffusion, intra-crystalline diffusion or micropore diffusion. As the pore diameter become similar to the molecular diameter, the force field at the pore wall inhibits the molecule to escape. Steric hindrance is therefore dominant and diffusion coefficient decreases with increasing molecular size (Figure 3.4). Within the micropore range diffusion becomes an activated process where the molecules jump randomly toward the low potential energy sites due to the steric effects caused by the interactions between the diffusing molecule and the pore wall. As being an activated process, the diffusional activation energy, stemmed from steric hindrance, is directly connected with the pore size and intracrystalline diffusion become a rapid and dominant process (Figure 3.4). As the pore diameter of the adsorbent phase decreases, the diffusing molecules never escape from the force field of the pore walls and it is therefore considered as a single adsorbed phase within the pore. It is difficult to distinguish the molecules on the surface and molecules in the gas phase in central region of the pores (Karger and Ruthven 1992, Do 1998, Ruthven 2001, Kärger et al. 2012). It is therefore required to consider the total intracrystalline concentration (q). Transport equation is in accordance with Fick's first

law in Equation 3.8. Fickian diffusivity become independent of the concentration and written as Equation 3.15.

$$D = D_0 \frac{d\,lnp}{d\,lnq} \tag{3.15}$$

Under the conditions of micropore diffusion the relevant mass transfer equation for uniform spherical particle can be obtained by Fick's second law stated in Equation 3.16 where r is the pore radius, D_c is the intracrystalline diffusivity and $q(r,t)$ is the adsorbed phase concentration.

$$\frac{\partial q}{\partial t} = \frac{1}{r^2}\frac{\partial}{\partial r}\left(r^2 D_c \frac{\partial q}{\partial r}\right) \tag{3.16}$$

If small changes in the adsorbed phase concentration occurs the intracrystalline diffusivity become constant.

For external film resistance, deposition of strongly adsorbed species on the external surface of the particle or collapse of the pore structure close to the particle boundary interrupts the mass transfer through the particle, causes the blockage of the pore mouth. Under these conditions transport rate through the particle boundary can be determined as shown in Equation 3.17 where k_s and $(q^* - q)$ represent surface rate coefficient and the difference between the equilibrium concentration of the adsorbed phase and the actual boundary concentration, respectively.

$$J = k_s(q^* - q) \tag{3.17}$$

The surface rate coefficient ($k_s = R_s D_s/\delta$) is correlated with reduced diffusivity (D_s) and thickness of solid surface layer (δ). In addition to surface resistance, if the diffusion is very rapid or if there is more than one component in the fluid or if the adsorbent is nonporous, the adsorption can occur only on the external surface and the transport rate will therefore dictated by diffusion through the laminar fluid film (or boundary layer) around the particle. The external resistance is associated with mass transfer coefficient (k_f) and Equation 3.18 defines the sorption rate where c and c^* are

the sorbate concentration in bulk phase and the fluid phase concentration at equilibrium, respectively.

$$J = k_f(c - c^*) \tag{3.18}$$

Except for nanoporous adsorbents, the external film resistance can be neglected since diffusion within the pores of the particle is slower than diffusion through the external fluid film. On the contrary surface resistance is very common and sometimes completely rate controlling (Rodrigues et al. 1989, Kärger et al. 2012).

3.3.4. Intracrystalline Diffusion Measurement Techniques

Many experimental techniques have been developed to study the diffusion in porous solids. A summary is given in Table 3.1. These techniques are classified according to the type of the process (transport or self-diffusion), the nature of the measurement (transient or steady state) and the scale of the measurement (micro, meso or macro) (Lee 2003). The study of tracer or self-diffusion requires measurements under equilibrium conditions whereas the study of transport diffusion necessarily involves measurements under nonequilibrium condition. Pulsed field gradient NMR (PFG NMR) and quasi-elastic neutron scattering (QENS) are regarded as microscopic equilibrium techniques. The estimation of self-diffusivity from such measurements are performed by determining the mean square molecular jump length in a known time interval (Kärger et al. 2012). The PFG NMR method relates with the nuclear spins of molecules and provides estimation of the molecular jump or displacement from the attenuation of spin echo response signals. The self-diffusivity (D_i^*) is then determined from the Einstein equation as $D_i^* = \lambda^2/2n\tau$ where n is the dimensionality of the pore structure, τ is the average time between molecular jump and λ is the mean jump distance (Ruthven 2001).

Table 3.1. Classification of methods for measuring intracrystalline diffusion in porous adsorbents (Source: Kärger et al., 2012).

Microscopic Methods	**Mesoscopic Methods**	**Macroscopic Methods**	
		Transient	**Quasi-steady state**
QENS	Single crystal permeation	**Sorption Rate**	**Membrane**
PFG-NMR	IFM	Flow- ZLC	Wicke Kallenbach
	IRM	TZLC	Single Crystal
		Batch- Gravimetric	
		Piezometric	
		FTIR	
		Chromatographic	
		Gas phase	
		Liquid phase	
		Frequency Response	

The mesoscopic techniques such as single-crystal IR microscopy (IRM), interference microscopy (IFM) and single crystal permeation allow direct measurement of diffusion on an individual crystals. Such measurement methods are based on the measurement of concentration integrals and referred as an intermediate method between microscopic and macroscopic measurements. Diffusivity data can be thus inferred indirectly by applying mathematical model from the analysis of transient concentration profiles during molecular uptake or release.

The macroscopic techniques are widely applied to measure transport diffusion at the length scale of individual crystals by either transient measurement of adsorption/desorption rates or steady-state measurement of flow through a membrane. Under equilibrium and transient conditions self-diffusion can be studied via Tracer ZLC (TZLC) by introducing isotopically labeled tracers into the sample and monitoring their equilibration over the sample. Under transient nonequilibrium conditions transport diffusion studies can be developed by sorption rate (flow or batch) and chromatographic measurements. Sorption rate (uptake rate) measurement is the most widely used method for transport diffusivity studies. Such measurements are performed in closed system where the adsorbent is exposed to uniform sorbate concentration. Fitting the experimental sorption curve to the theoretical curve the transport diffusivity is then calculated from an appropriate mathematical model for the relevant boundary conditions. Transient sorption rate measurements in batch system can be performed by using gravimetric method,

pizeometric method or FTIR. Gravimetric method offers detecting the adsorbed amount directly from the change in weight of adsorbent by using a vacuum microbalance after subjected to sorbate gas. Piezometric measurements provides following the pressure change in a constant volume system by adding the sorbate gas (Kärger et al. 2012). As the piezometric system is sensitive to pressure changes, opening the valve to send a sorbate gas to system can cause sudden increasing in the pressure and mislead the initial portion of the response curve. Such methods can be strongly influenced by heat effects and be only appropriate for fast diffusing and strongly adsorbed species and small amount of adsorbent sample (Karge and Weitkamp 2008). FTIR technique has been introduced as an alternative to the gravimetric or piezometric methods and measures the IR adsorbance for an adsorbent at a defined frequency by changing the pressure of the sorbate gas. The zero length column (ZLC) technique is considered as both transient sorption rate and chromatographic measurements under flow conditions. The chromatographic technique where carrier and adsorbate gas stream flows through a packed adsorbent column is an alternative to sorption rate method. For a linear system Henry's law constant can be extracted by the retention time. Diffusion time constants can be determined by fitting an appropriate solution to the measured response curve (Kärger et al. 2012). The main drawback of this method is separation of the axial dispersion from intracrystalline diffusion and requirement of high amount of adsorbent sample. The axial dispersion can be prevented by packing the column with unaggregated well-dispersed particles (Ruthven 2001). Permeation measurements are steady state method to yield the intraparticle diffusivities in porous adsorbents. The flux of adsorbate through a pellet or membrane whose faces are subjected to known concentration is measured. The diffusivity of the adsorbate can be extracted by using the composition, flow rates of gas streams and concentration gradient. The Wicke-Kallenbach method is a type of permeation measurements involves constant pressure or pressure gradient (Schuring 2002). As this method is maintained under steady state conditions, heat resistances can be eliminated. Using macroporous adsorbents can cause deviation from the diffusivity values gained from transient sorption rate measurements as dead end pores do not contribute to steady state flux (Rodrigues et al. 1989).

3.4. Zero Length Column (ZLC) Method

The Zero Length Column (ZLC) method is a well-known chromatographic technique for measurement of diffusion of gases in solid adsorbents. ZLC method has been widely utilized to examine kinetic and equilibrium properties of gas adsorption systems. It is also a rapid and convenient method to derive kinetic parameters such as intraparticle diffusivities or equilibrium data, including Henry's constant and complete isotherms (Friedrich et al. 2015). Other diffusion measurement techniques necessarily require using high carrier flow rates to minimize the effects of both axial dispersion and external heat and mass transfer resistances, which inevitably deviates the kinetic data including diffusivity value (Kärger et al. 2012). The major advantages of ZLC technique over other methods are involving very shallow ("zero-length") column and very small amount of sample without any agglomeration. A thin layer of small amount of sample is dispersed as a monolayer between the sintered discs inside the ZLC column. Due to this factor the effect of axial dispersion and heat and mass transfer resistances can be eliminated by neglecting the influence of column properties (Karge and Weitkamp 2008). Using low adsorbate gas concentration can also allow to neglect the external mass and heat transfer resistances (Hu et al. 2014). ZLC column can be therefore considered as a well-mixed isothermal cell.

3.4.1. Mathematical Model

The representative ZLC column was schematized in Figure 3.7.

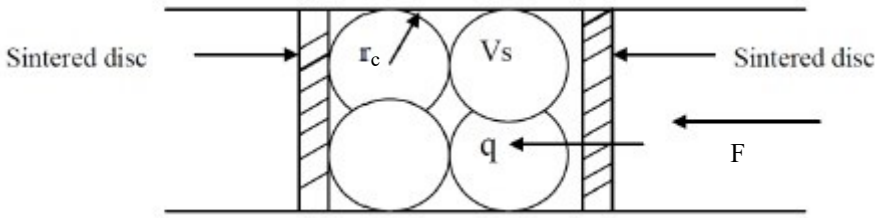

Figure 3.7. Representative ZLC column.

Eic and Ruthven (1988) are stated a mathematical model conforming the assumptions of uniform spherical particles, Fickian diffusion, linear sorption isotherm

and perfect mixing fluid phase, isothermal conditions and high flow rate of the gas phase without any hold-up in the fluid phase The ZLC theory therefore assumes that the system can be treated as a well mixed cell. The differential fluid phase mass balance can be written as in Equation 3.19 where V_g and V_s are the volume of gas and solid inside the column respectively, F is the volumetric flow rate, $\bar{q}$ is the average adsorbed phase concentration and c is the gas phase concentration (Ruthven et al. 2003, Friedrich et al. 2015).

$$V_s \frac{\overline{dq}}{dt} + V_g \frac{dc}{dt} + Fc = 0 \tag{3.19}$$

The dynamic behaviour of an isothermal system of uniform spherical particles with linear equilibrium between the adsorbed and fluid phase can be described by Equation 3.20 where r is the radius of the sphere, D_c is the intracrystalline diffusivity and q(r,t) is adsorbed amount as a function of time t and radial position r.

$$\frac{\partial q}{\partial t} = D_c \left(\frac{\partial^2 q}{\partial r^2} + \frac{2}{r} \frac{\partial q}{\partial r} \right) \tag{3.20}$$

Considering the initial conditions, $q(r,0)=q_0=Kc_0$ (for t=0) and $c(0)=c_0$, and the boundary conditions for t≠0 are $\left(\frac{\partial q}{\partial r}\right)_{r=o} = 0$ and $q(R,t)=K_c(t)$, the Equation 3.19 can be rewritten as given in Equation 3.21.

$$D_c \frac{\partial q}{\partial r}(R,t) + \frac{1}{3} \frac{FR}{V_S K} q(R,t) = 0 \tag{3.21}$$

Equation 3.22 represents the analytical solution of ZLC response curve for the effluent gas concentration in the column.

$$\frac{c}{c_0} = 2L \sum_{n=1}^{\infty} \frac{\exp\left(-\frac{\beta_n D_c t}{R^2}\right)}{\left[\beta_n^2 + L(L-1)\right]} \tag{3.22}$$

β_n is the positive roots of the transecendental equation given in Equation 3.23.

$$\beta_n cot\beta_n + L - 1 = 0 \tag{3.23}$$

The parameter L, ratio of the diffusional time constant (R^2/D_c) to the washout rate of the solid phase, defined as in Equation 3.24 in which r is the radius of the particle and K is the dimensionless Henry's Law constant (Ruthven and Vidoni 2012).

$$L = \frac{F}{3KV_S}\frac{R^2}{D_c} = \frac{1}{3}\frac{Purge\ flowrate}{Adsorbent\ volume}\frac{R^2}{D_c} \tag{3.24}$$

The L parameter defines how far the system is from equilibrium. The desorption rate is controlled by the diffusion of adsorbate at high purge flow rates, that is if the L values is high enough (L>10), the system is in the kinetically controlled regime (Mangano et al. 2013). For the long time region, only the first term of the summation become important and Equation 3.23 is simplified to exponential decay curves as stated in Equation 3.25 which defines the log time asymptote.

$$ln\left(\frac{c}{c_0}\right) \approx ln\left[\frac{2L}{\beta_1^2+L(L-1)}\right] - \beta_1^2\frac{D_c t}{R^2} \tag{3.25}$$

For the large L values β_1 closes to π ($\beta_1 \rightarrow \pi$). The plot of $\log(c/c_0)$ vs. t yield a linear long time asymptote (or linear tail) with slope $-\pi^2 D_c/R^2$ and intercept, yielding L values, obtained by the first term of Equation 3.25. By using L values obtained from the intercept, the Henry's Law constant can be extracted from Equation 3.25. In literature, the short time and intermediate time solution methods were also proposed but they are not widely used since L values can be deviated in that regions and the slope of the long time asymptote tail yields the accurate diffusional time constant value (Hufton and Ruthven 1993, Duncan and Möller 2000, Loos et al. 2000).

At low purge flow rate the residence or contact time is larger than the diffusion time constant and the desorption rate is under equilibrium control. Assuming the linear equilibrium, then Equation 3.26 is given as,

$$\bar{q} = q^* = Kc \tag{3.26}$$

$\bar{q}$ is the average gas concentration and q^* is the equilibrium value. An exponential decay is written as in Equation 3.27 where V_g is the dead volume of the system.

$$\ln\left(\frac{c}{c_0}\right) = -\frac{Ft}{KV_s+V_g} \tag{3.27}$$

The slope of the plot of $\ln(c/c_0)$ vs. time yields $-F/(KV_s+V_g)$. If the adsorbate is strongly adsorbed, K value is large (so $KV_s >> V_g$) and therefore the Equation 3.27 becomes as Equation 3.28.

$$\ln\left(\frac{c}{c_0}\right) = -\frac{Ft}{KV_s} \tag{3.28}$$

In that case, the slope of the plot of $\ln(c/c_0)$ vs. Ft yields directly the K value. If the adsorbate is weakly adsorbed, the value of KV_s is the same order of magnitude of V_g. Therefore, the value of V_g should be determined by performing the blank experiment with no adsorbent in the column at the same conditions. As there is no adsorbent presented in the ZLC column, $V_s=0$ and the Equation 3.28 simplified to Equation 3.29.

$$\ln\left(\frac{c}{c_0}\right) = -\frac{Ft}{V_g} \tag{3.29}$$

The slope of the plot of $\ln(c/c_0)$ vs. Ft produced directly V_g (Ruthven et al. 2003, Mangano et al. 2013).

3.4.2. ZLC Studies

Eic and Ruthven first introduced ZLC technique in 1988 to investigate intracrystalline diffusion in zeolite samples. A simple mathematical modal was proposed by Brandani et al. (2000). This technique was then adapted to study tracer self diffusivity, counter diffusion and macropore diffusional resistances in zeolite and biporous adsorbent (Ruthven and Stapleton 1993, Hufton et al. 1994, Brandani 1996, Brandani et al. 2000).

The gas adsorption kinetic studies using ZLC method on MOFs are very limited in literature. Traditional adsorbents, or zeolites, have been mostly chosen for kinetic

investigations. So far there is no adsorption kinetic studies on MIL-53(Al) has ever been reported. Ranking of CO_2 capacity of different MOFs containing Mg based MOF Mg/DOBDC (DOBDC= dioxybenzenedicarboxylate), Ni/DOBDC, etc. and several zeolite types revealed that Mg/DOBDC was an excellent candidate adsorbent for carbon capture applications (Hu et al. 2015). Hu et al. (2015) also performed more detailed investigations for the diffusion behavior of CO_2 in cobalt based MOF, Co/DOBDC, and nickel based MOF, Ni/DOBDC. The study indicated that Co/DOBDC has lower micropore diffusivity and CO_2 capacity than Mg/DOBDC due to experiencing macropore diffusion control (Gibson et al. 2016).

Several experimental parameters have an influence on the value of diffusional time constant and Henry's constant. The diffusional time constant or diffusivity obtained from the slope of the response curve is independent of the purge flow rate whereas it is directly proportional to temperature (Liu et al. 2013, Saha et al. 2008). Henry's constant decreases with increasing temperature and increases with flow rate (Vidoni and Ruthven 2012). Beside temperature and flow rate, diffusivity of propane to n-hexane in zeolite and NaCaA decreases from as chain length increases (Gunadi and Brandani 2006, Möller et al. 2009). Diffusional time constant is inevitably affected from the size distribution. (Duncan and Möller 2002). The dead volume experiments are performed to determine the experimental decay caused by the setup and ZLC cell. The blank run for n-decane in silicalite represents 30 s concentration decay (Guimarães et al. 2010).

Beside kinetic studies, equilibrium data including adsorption isotherms and equilibrium constant (Henry's constant) can also be accessed by ZLC technique. Maintaining the measurements at very low flow rates, thus low L parameter ($L<5$), provides an equilibrium controlled system and a response curve containing without any kinetic information such as Henry's constant (Ruthven and Brandani 2000). Silva et al. (2012) studied the gas adsorption equilibrium of CO_2 and CH_4 gases in zeolite at a temperature range.

Ruthven and Vidoni (2012) derived the extended mathematical model for the gas adsorption kinetics dictated by the combined effect of intracrystalline diffusion and surface resistance. The effects of surface barrier and bed diffusion on the response curve were understood from an observable jump at the begining of the response curve with an asymptotic tailing obviously seen in the study of (Eić et al. 2002). The slope of the long time asymptote is not influenced by the surface resistance whereas the intercept of the

asymptote, which gives the dimensionless parameter L, is considerably affected by the surface resistance (Ruthven and Vidoni 2012). For the diffusion of C_2H_6 and C_2H_4 in DDRI studied by (Vidoni and Ruthven 2012), as the intercepts are constant with flow rate but decreased with temperature which implied a higher activation energy, the surface resistance was formed due to the blockage of pore entrances. Ruthven and Brandani (2005) also studied the gas adsorption kinetics controlled by both surface resistance and internal diffusion control for linear or nearly linear systems by investigating the ratio of slope to intercept of response curves (Ruthven and Vidoni 2012). Decreasing diffusivity with increasing temperature can be explained by the intrusion of surface diffusion (molecular or Knudsen diffusion) to macropore diffusion or by the micropore diffusion with nonlinear trend (Zaman et al. 2015). To control whether the system is under macropore diffusion control, the experimental conditions, such as the bead radius, molecular diffusivity or using different carrier gas, can be adjusted. If the system is controlled by macropore diffusion, changing each experimental conditions must yield different diffusivity values. Different diffusivity values of CO_2 in 13X zeolite with two different carrier gas revealed that the diffusion process had been maintained under macropore diffusion control (Hu et al. 2014). The diffusion mechanism of CO_2 in 13X zeoilte was dictated by macropore diffusion at increasing CO_2 concentrations since the obtained micropore diffusivities are six orders of magnitude smaller than intracrystalline self-diffusivities (Mangano et al. 2013, Hu et al. 2014).

CHAPTER 4

EXPERIMENTAL STUDIES

4.1. Materials

In the synthesis of Al-TPA, aluminum nitrate nonahydrate ($Al(NO_3)_3.9H_2O$, ≥99.5% purity), benzene-1,4-dicarboxylic acid or terephthalic acid (TPA, BDC or H_2BDC, C_6H_4-1,4-$(COOH)_2$, ≥99.6% purity), N,N-dimethylformamide (DMF, $(CH_3)_2NCOH$, ≥99.8% purity) and methanol (CH_3OH, ≥99.9% purity) were used. Methanol and DMF was purchased from Merck. Aluminum nitrate nonahydrate was purchased from Sigma Aldrich and terephthalic acid was provided by PETKİM.

4.2. Synthesis of Al-TPA

Aluminum Terephthalate (Al-TPA) can be synthesized either by means of hydrothermal or solvothermal synthesis routes. Both of the synthesis route consist of three main steps, crystallization, purification and activation.

4.2.1. Hydrothermal Synthesis of Al-TPA

ALTPA was synthesized by means of a hydrothermal treatment proposed by Loiseau et al. (2004) starting with aluminum nitrate nonahydrate ($Al(NO_3)_3 \cdot 9H_2O$), terephthalic acid (Benzene-1,4- dicarboxylic acid, BDC, TPA) and deionized water. The molar ratio of the starting materials (Al:BDC:H_2O) was 1:0.5:80. Initially 4.04 g of BDC (0.024 mol) was stirred in 70 mL of water (3.89 mol) for 5 h at 330 rpm at room temperature. 18.2 g of $Al(NO_3)_3 \cdot 9H_2O$ (0.049 mol) was added into the solution and stirred with magnetic stirrer (IKA-Werke RT5 Power) for 10 minutes at 330 rpm at room temperature. For crystallization step the solution was loaded into a Teflon-lined stainless steel autoclave and heated to 220°C for 72 h in an oven (BINDER-ED 53). After the

autoclave was cooled down to room temperature, the solution was centrifuged (Hettich Rotofix32 Zentrifugen) at 3000 rpm for 25 minutes to seperate solid and liquid part of the solution. After filtering off the solution, the remaining solid was washed and purified for 2 h with 50 mL of deionized water for 5 times (pH was measured after each washing step) at room temperature to remove nitric acid and neutralize the acidic medium. The pH of the solution was approximately 3.93. Activation step can be performed by either calcination method or solvent extraction method introduced by Bajaj et al. (2010).

Activation by calcination method: After purification step, the solution was centrifuged and the filtered product was transferred to porcelain crucible and calcined at 330°C for 72 h for complete removal of remainin impurities (unreacted BDC, nitric acid, etc.) entrapped in the pores. (Figure 4.1)

Activation by solvent extraction method: The filtered product was dissolved in 50 mL of DMF by stirring with magnetic stirrer at 330 rpm for 24 h at room temperature. The solution was centrifuged and 50 mL of DMF was added into the filtered product. The solution was loaded into a Teflon-lined stainless steel autoclave and heated to 130°C for 24 h. The previous washing step with hot DMF was performed once again. After that, the solution was centrifuged and the filtered product was purified with 200 mL of methanol by means of Soxhlet extractor for 20 h. Finally, the product was delivered to porcelain crucible and heated to 200°C for 72 h in a vacuum drying oven (VACIOTEM-T P-Selecta Oven) (Figure 4.2).

An initial pre-crystallization step can also be added in the hydrothermal synthesis of Aluminum terephthalate. Aluminum nitrate nonahydrate was directly added into the solution containing dissolved BDC in water. The molar ratio of the starting materials (Al:BDC:H_2O) was 1:0.5:80. Briefly, 4.04 g of BDC (0.024 mol) was dissolved in 70 mL of water (3.89 mol) for 1 h at room temperature. Then, the solution was loaded into a Teflon-lined stainless steel autoclave and heated to 220°C for 24 h. After the autoclave was cooled down to room temperature, 18.2 g of $Al(NO_3)_3 \cdot 9H_2O$ (0.049 mol) was added directly into the solution and stirred for 5h at room temperature. For crystallization step, the solution was placed in the autoclave and heated to 220°C for 72 h. The remaining purification (washing with water) and activation steps (calcination at 330°C for 72 h) were performed as stated in hydrothermal synthesis route in experimental part.

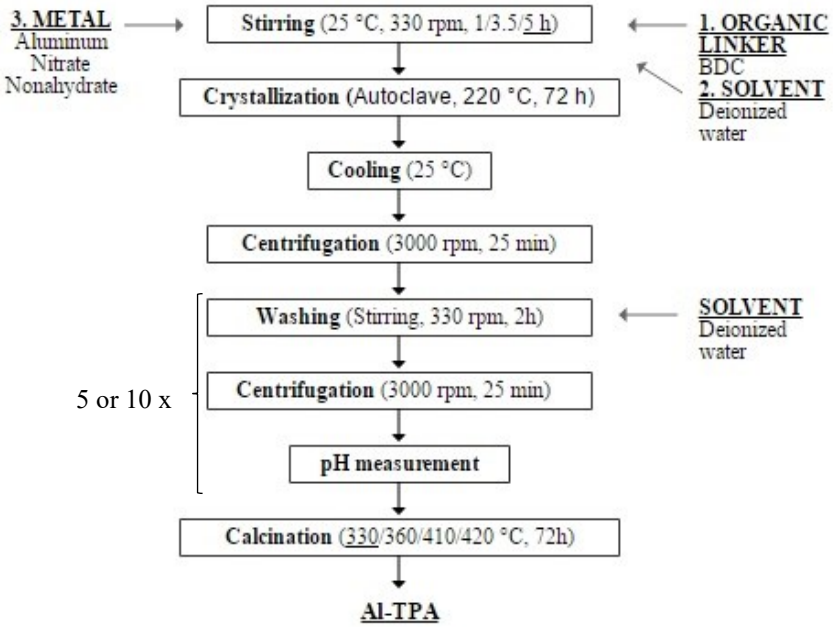

Figure 4.1.The synthesis of Al-TPA by hydrothermal synthesis method (Activation by calcination method).

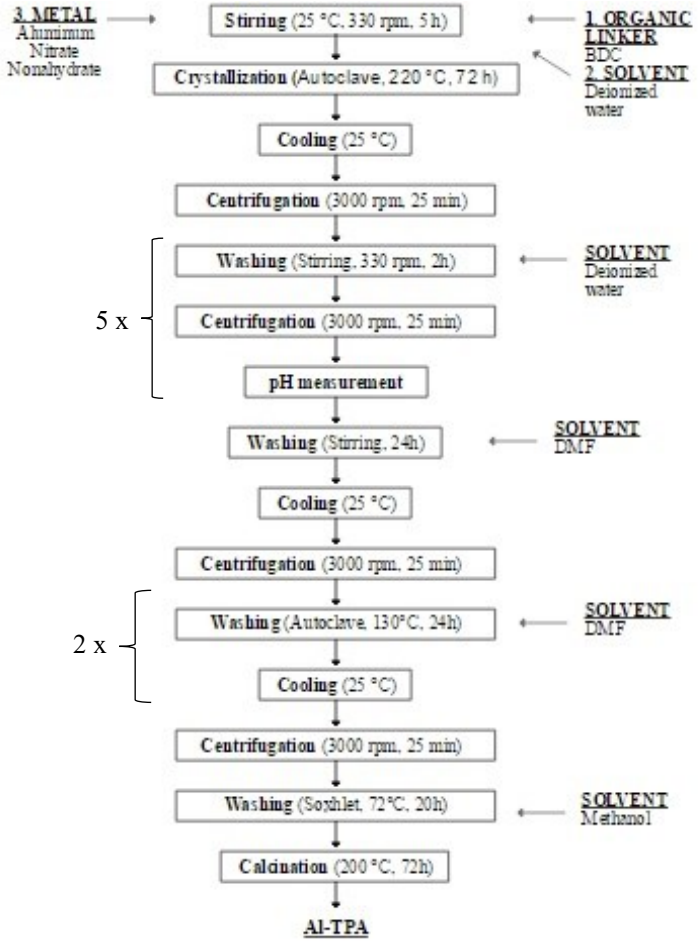

Figure 4.2.The synthesis of Al-TPA by hydrothermal synthesis method (Activation by solvent extraction method).

4.2.2. Solvothermal Synthesis of Al-TPA

The synthesis of Al-TPA was carried out under solvothermal conditions introduced by Rodrigue et al. (2012) using aluminum nitrate nonahydrate ($Al(NO_3)_3 \cdot 9H_2O$), Terephthalic acid (Benzene 1,4-dicarboxylic acid, BDC, TPA) and dimethylformamide (DMF). The starting materials with molar composition of 1 $Al(NO_3)_3 \cdot 9H_2O$ (1.85 g, 0.0049 mol): 1.48 BDC (1.21 g, 0.0073 mol): 184.5 DMF (70 mL, 0.91 mol) were stirred at 330 rpm for 24 h at room temperature. The resulting mixture was loaded into a Teflon-lined stainless steel autoclave and heated to 130°C for 72 h. At the end of the crystallization step, the solution was centrifuged at 3000 rpm for 25 minutes and the filtered product was dissolved in 50 mL of DMF. The solution was transfered to Teflon-lined stainless steel autoclave and heated to 130°C for 24 h, and centrifuged. The latest step was performed once more. DMF was used to eliminate unreacted BDC remaining in the pores of the structure. Then, impurities such as unreacted DMF was removed by methanol Soxhlet extraction for 20 h. Lower boiling boint solvent methanol was exchanged with higher boiling point dmf solvent and in the activation step lower activation temperature is enough. Finally, the solids were activated at 130°C for 72 h to vaporize the remaining trace amount of impurities from the framework structure (Figure 4.3).

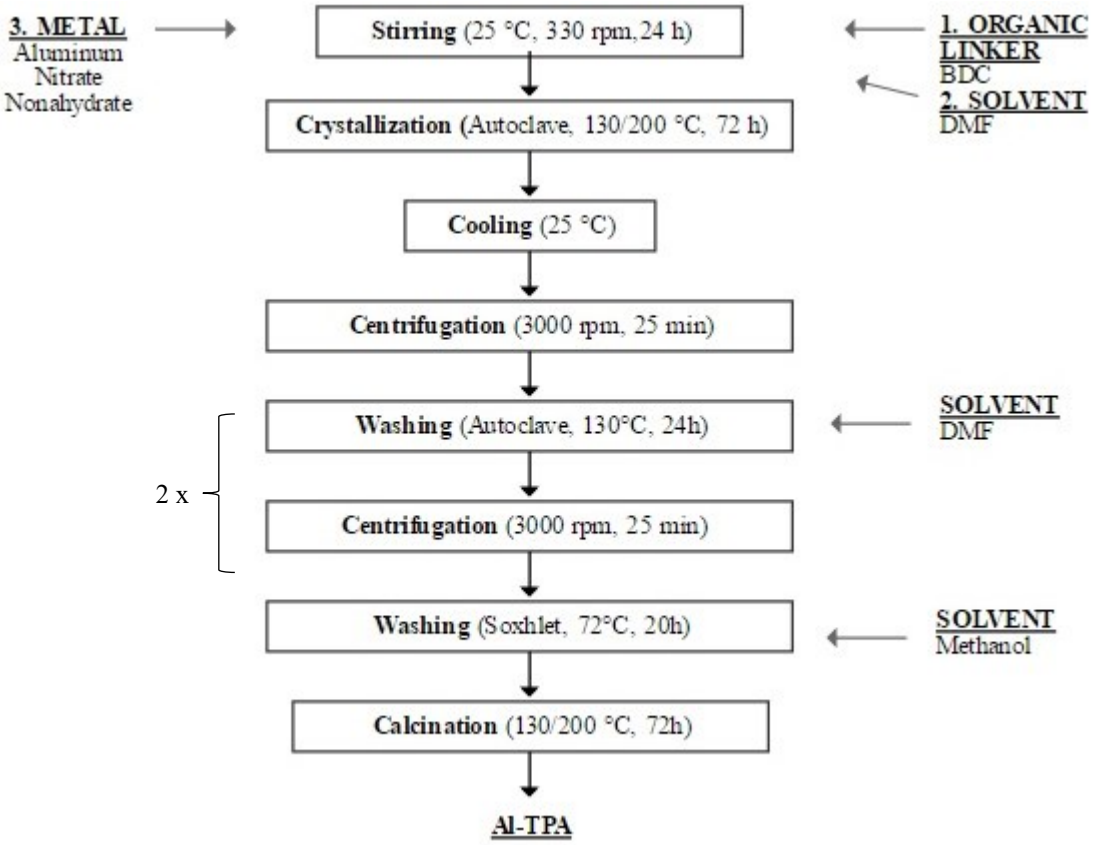

Figure 4.3. The synthesis of Al-TPA by solvothermal synthesis method.

4.2.3. Hydro-solvothermal Synthesis of Al-TPA

The synthesis of Al-TPAs via hydro-solvothermal method were accomplished according to the procedures described by Zhu et al. (2016) and Zhou et al. (2013) and summerized in Figure 4.4. The molar composition of the starting materials are 1.5 $Al(NO_3)_3.9H_2O$:1 BDC:95 DMF:153 H_2O. 4.22 g of $Al(NO_3)_3.9H_2O$ (0.011 mol) and 1.245 g of BDC (0.0075 mol) were dissolved in the mixed solvent of 20 mL of deionized water and 55 mL of DMF under magnetically stirring (330 rpm) at 40°C for 40 min. The mixture was placed into a Teflon-lined steel autoclave and heated in an oven to 150°C (130°C for the procedure of Zhou et al. 2013) for 48 h. After centrifugation, the solid portion was washed with deionized water for 5 times to eliminate the acidic medium (due to nitric acid by-product) and neutralize the solution. The product was filtered and washed with 50 mL of DMF in Teflon-lined steel autoclave at 130°C for 6 h (130°C for 24 h for Zhou et al. 2013) for the removal of unreacted BDC entrapped in the pores. To exchange

the DMF solvent with a solvent possessing lower boiling point, the white powder was washed with methanol via Soxhlet extractor at 72°C for 20 h. Finally, the fine powdered Al-TPAs was thermally activated at 180°C (150°C for Zhou et al. 2013) under vacuum for 12 h to remove any remaining impurities from the cavities of the Al-TPA structure.

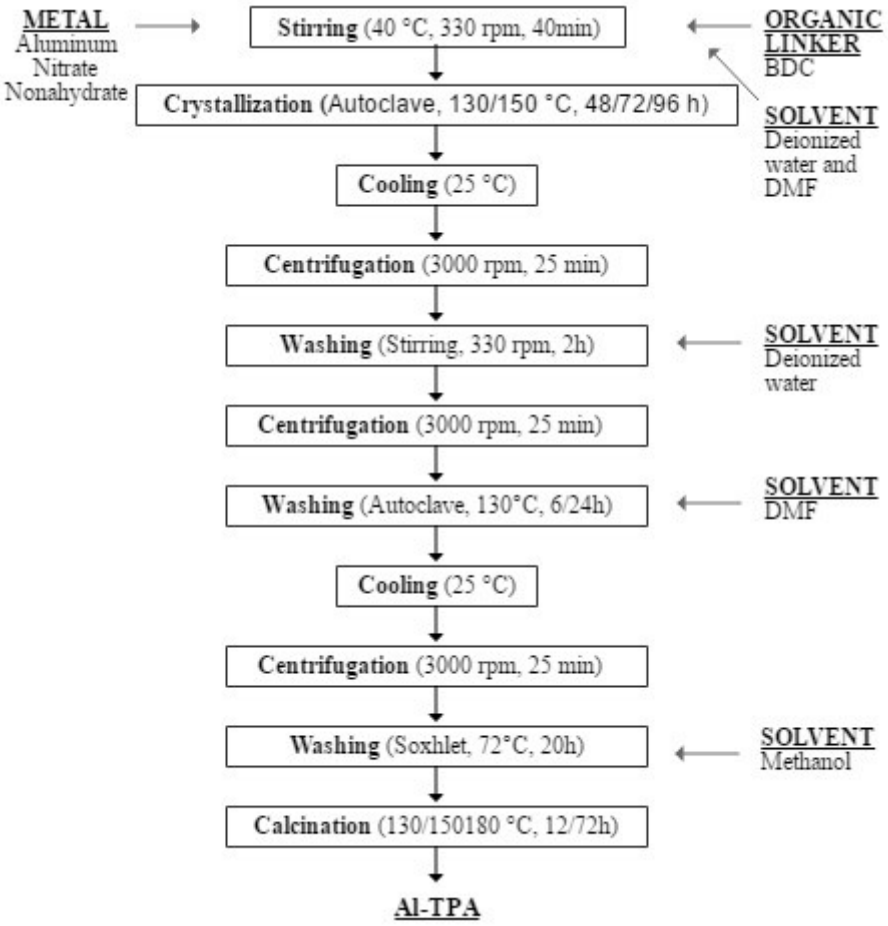

Figure 4.4. The synthesis of Al-TPA by hydro-solvothermal synthesis method.

4.3. Characterization Methods of Al-TPA

The morphologies and particle size of the synthesized Al-TPAs were observed by scanning electron microscope (SEM, FEI QUANTA 250 FEG) with magnification ranging from 2500X to 80000X under secondary electron (SE) and back scatter electron (BSE) detectors. Crystallographic structure of Al-TPAs were evaluated by X-ray diffraction (XRD, Philips X' Pert Pro Diffractometer) with a standart scan speed of 2

°/min and a step size of 0.002° in the range of 5-85° under CuKα radiation. Thermal stability and the impurities presented in the Al-TPAs were investigated by Thermogravimetric analysis (TGA, Shimadzu TGA-51) with the heating rate of 10 °C/min under dry air flow rate of 40 mL/min. Interaction between atoms presented in the structure of Al-TPAs were examined by Fourier Transform Infrared spectrophotometer (FTIR, Shimadzu 8201) requiring preparation of the pellets consisting of Al-TPA sample (1.5 mg) and KBr (148.5 mg). Textural properties of Al-TPAs were investigated performing nitrogen adsorption and desorption isotherms at 77.35 K at low pressure of 10 cm^3/g STP by volumetric adsorption instrument (Micromeritics ASAP 2010 M). Al-TPAs were degassed for each measurements at 200°C for 24 h considering the thermal stabilities. The surface areas were calculated by Brunauer-Emmett-Teller (BET) and Langmuir method, and pore diameters were calculated using Barrett-Joyner-Halenda (BJH) model and Horvath-Kawazoe method.

4.4. Diffusion Measurement Studies

Adsorption of CO_2, CH_4, H_2 and CO gases on synthesized Al-TPA was studied in a home-made ZLC system. Simplified schematic diagram of the ZLC experimental system were indicated in Figure 4.5. The system consists of gas flow controllers (Aalborg DFC 26), valves (V1, V2 and V3), oven (Binder ED 53), zero length column containing Al-TPA adsorbent, soap bubble meter and mass spectrometer (MS, Hiden HPR 20). The ZLC cell consist of a small amount of Al-TPA (≈10 mg) powder sandwiched between two porous sintered discs (35 μm, Alltech) within 1/8-in Swagelok fitting union. The both ends of the ZLC cell was covered by quartz wool to prevent Al-TPA powders to escape the mass spectrometer. The ZLC cell is located in an oven to adjust the temperature during the experiments.

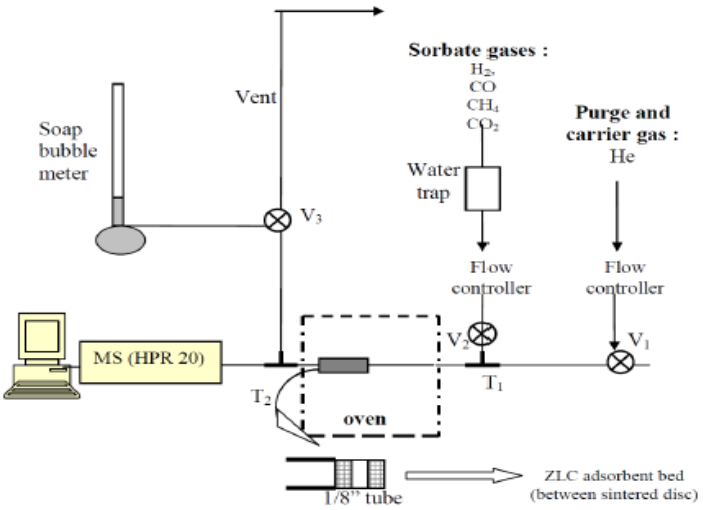

Figure 4.5. Experimental set-up of ZLC system.

Initially, oven is set to desired temperature and 70-90% volume pure inert Helium purge gas is send through the ZLC column by opening the V1 valve. Then, the dilute mixture of gases containing 10-30% volume of adsorptive gas (CO_2, CH_4, H_2 or CO) and 70-90% volume Helium carrier gas was send to DFC gas flow controller by adjusting the flow rates of gases. Helium purge gas was used for each measurement since it has inert nature and do not react with other gases and Al-TPA adsorbent without any contribution to adsorption or diffusion process. Adsorption process was established immediately after opening the V2 valve. During the adsorption, the stability of flow rate of gases which had been adjusted by DFC gas flow controller is continously checked by using soap bubble meter (containing soap and water) by switching the V3 valve in the direction of soap bubble meter. After checking, by switching the V3 valve in the direction of air vent some portion of gases is passed through the column and the surplus gas is released to prevent the mass spectrometer from high pressure. Once the stability of adsorption was ensured, desorption process is established by switching off the V3 valve and immediately sending only pure Helium purge gas (100% volume) at a flow rate through the ZLC column. After the adosrption and desorption process is completed, regeneration step was carried out by the flow of Helium carrier gas of 10 mL/min at 200°C for 3 h. During the adsorption and desorption process, mass spectrometer, comprising of Faraday detector, continously monitors the partial pressure of each gases and adsorption/desorption curves. The response curves used for diffusion measurements are obtained from the desorption process which proceeds under kinetic control.

CHAPTER 5

RESULTS AND DISCUSSION

5.1. Hydrothermal Synthesis of Al-TPA

The effect of several reaction conditions, including stirring time (1, 3.5, 5 hours), the amount of washing (5 and 10 times with water), the solvent type (water and water/dmf/methanol), activation temperature (330, 360, 410, 420 °C) and precrystallization step, on synthesized aluminum terephthalates were investigated during the hydrothermal synthesis of Al-TPA. The characterization results of synthesized aluminum terephthalates were compared with that of reported in literature (Loiseau et al. 2004).

Precrystallization step: Effect of stirring time

Aluminum terephthalates were stirred for 1, 3.5 and 5 h at ambient temperature before placing in the oven for crystallization step. The SEM images of Al-TPAs were given in Figure A.1. The morphologies of Al-TPA crystals are uniform, fine and long crystal structure having approximately 5 μm size. The XRD patterns for Al-TPAs given in Figure A.2, presenting characteristic peak at 2θ= 8.94, 12.3, 14.6, 17.5 and 28.4°. The crystal structures for aluminum terephthalates resemble each other.

TGA profiles given in Figure A.3 shows three main events between ambient temperature and 850°C. An initial decrease in mass up to 100°C is due to the departure of nitric acid and dehydration of H_2O molecules from the pores. Although Al-TPAs were washed with water for several times, pH=4 can be attained and the medium was still acidic, proved that nitric acid and H_2O molecules can not be completely removed from the aluminum terephthalates. The second region of loss within 350-550°C is originated from the unreacted free BDC entrapped in the pores. The boiling point of BDC is 300°C. Having a weight loss in that region unreacted BDC can not be eliminated by washing only with water since BDC and water are immiscible solvents at room temperature. Al-TPAs

keep their integrity up to 560°C and then thermal decomposition of Al-TPA in two steps to amorphous alumina was established by degradation of bridging bdc linkers (Loiseau et al. 2004).

The FTIR spectra of aluminum terephthalates, given in Figure A.4, stirred for different times overlap with each other. Al-TPA exhibits triplet peaks between 400-800 cm^{-1} correspond to C-H bond of 1,2,4 aromatic ring and the peak at 1000 cm^{-1} attributed to Al-O(H) bond. The peak at 990 cm^{-1} is attributed to the deformation mode of bridging OH groups. The sharp peak at 1508 cm^{-1} is due to the C-C ring vibrations. There are two important indicator in the FTIR spectrum demonstrating the complete formation of Al-TPA network structure. The first one is sharp and distinct peaks between 1400-1700 cm^{-1} corresponding to bond between Al and carboxylate group ($-COO^-$). The other important one is the broad band at 3500 cm^{-1} corresponding the bond between Al and bridging OH (or μ_2-OH) which did not formed in the synthesized aluminum terephthalates. Al-TPAs contain doublet discrete bands at 3100-3300 cm^{-1} attributed to (Al)O-H bond and the more groove between the doublet bands the more nitric acid presented in the cavities. The small shoulder at 3700 cm^{-1} arose from the excess water and Al-TPAs contain water molecules (Loiseau et al. 2004, Hadjiivanov et al. 2016).

Either characterization results or BET surface area results proved that the synthesized Al-TPAs do not possess the similar structure with the desired MIL-53(Al) structure reported in literature. To investigate the structure that we synthesized, the XRD patterns of Al-TPAs has been scanned by using MATCH! Database. The database guided us that the synthesized Al-TPAs have a similar structure with boehmite material (Figure A.5). Due to this, bond structure of synthesized Al-TPA was compared with that of boehmite. In Figure A.6, FTIR spectrum given of boehmite indicated three triplet peaks at 400-800 cm^{-1}, as also seen in the FTIR spectrum of Al-TPAs, attributed to the bond between Al-O_6 and also –OH bond. Boehmite also contains Al-OH bond at 1000 cm^{-1}. The primary indicator of boehmite formation is the doublet broad bands at 3100-3300 cm^{-1} due to the O-H bond can be observed in both boehmite and Al-TPA. On the contrary of boehmite, Al-TPA exhibits a little Al-COO^- formation at 1400-1700 cm^{-1} due to the presence of aluminum nitrate nonahydrate and terephthalic acid during the synthesis.

BET surface areas of aluminum terephthalates are less than 100 m^2/g. Al-TPA 1 (1 hour) has the highest BET and Langmuir surface area while Al-TPA (3.5 h) has the

smallest surface area results. The XRD patterns, FTIR spectra and surface area results demonstrated that synthesized Al-TPAs have a structure similar to boehmite.

Precrystallization step: Effect of precrystallization temperature

SEM images of Aluminum terephthalate synthesized via hydrothermal method with pre-crystallization step were given in Figure A.7. Crystals have three dimensional irregular cubic shaped particles having less than 5 μm diameter.

Figure A.8 shows the XRD patterns of Al-TPA performed with precrystallization step representing a different MOF structure other than boehmite and Al-TPA. The synthesized Al-TPA have CAU-13 MOF structure according to the MATCH! Database (Figure A.9). During the given initial precrystallization part, structure of BDC changed by hydrogenation of BDC in the presence of water at high temperature (220°C). As 1,4-cyclohexanedicarboxylic acid behaved as organic linker instead of BDC, a different type Aluminum based MOF structure called CAU-13 MOF was formed. The characteristic XRD peaks obtained from CAU-13 are 2θ angle of 9.5, 9.8, 11.6, 16.3 and 21.3° which also partially coincide with the literature value of the XRD peaks of CAU-13.

Weight loss and its derivative curves given in Figure A.10 shows that Al-TPA does not contain any trace of water and nitric acid considering the initial decrease in mass up to the temperature of 100°C. High temperature activation step used in Al-TPA provided to complete removal of H_2O and nitric acid molecules. The weight loss around 400°C depicts that purification with water was not sufficient for the removal of BDC since BDC cannot be dissolved in water at room temperature. The sharp decrease in mass starting approximately from 550°C is attributed to the decomposition of Al-TPA framework to amorphous Al_2O_3.

FTIR spectra of aluminum terephthalate with precrystallization step were illustrated in Figure A.11. The sharp peak located at 990 cm^{-1} associate with the stretching and bending vibrations of Al-OH which is found in the both boehmite and Al-TPA structure. The sharp peaks appearing in the range of 1400-1700 cm^{-1} suggest the interaction of $–COO^–$ of carboxylic group with the aluminum of framework were observed in Al-TPA. The small peak at 1693 cm^{-1} associates with the existence of protonated –COOH groups of BDC entrapped in the pores of network. High intensity of this peaks for Al-TPA prove that Al-TPA contain unreacted BDC as observed from TGA.

The broad band at 3500 cm^{-1} is ascribed to the bridging OH groups connected to Al which refers to the complete framework structure. Al-TPA does not indicate the broad adsorption band at 3500 cm^{-1}. Al-TPA does not contain doublet bands at 3090-3304 cm^{-1} which is the main cursor of boehmite formation refers to AlO-H stretching vibrations. The overall FTIR spectrum of synthesized Al-TPA differs from that of boehmite since applying the initial precrystallization step changes the structure of BDC to 1,4 cyclohexanedicarboxylic acid. Acting as organic linker, a new Al based MOF structure called CAU-13 was formed.

BET surface area of Al-TPA 11 with precrystallization was less than 100 m^2/g. Characterization studies revealed that the followed proposed procedures cause to produce Al-TPA in the form of CAU-13 MOF instead of desired Al-TPA MOF structure.

Purification step: Effect of the amount of washing

In the purification step, aluminum terephthalates have been reached to pH= 3.91 and pH= 4.06 after washing respectively with water for 5 and 10 times. The pH values of Al-TPA are not affected by the number of washing with water. The crystal morphologies of both Al-TPAs look similar with each other (Figure A.12). As seen in Figure A.13, XRD patterns, namely the crystal structures, of Al-TPAs representing 2Θ= 9.4, 12.5, 14.6, 17.8 and 28.3° overlap with boehmite. According to TGA curves represented in Figure A.14, both Al-TPAs contain same amounts of water and nitric acid in their pores. The medium is still acidic due to their pH values. Al-TPAs washed with 5 and 10 times degraded by two steps with weight loss of 26% and 30% at 550°C. The FTIR spectra of both Al-TPAs is identical with each other and with boehmite (Figure A.15). The two main peaks indicating the formation of Al-TPA framework, 1400-1700 cm^{-1} for Al-COO^- and 3500 cm^{-1} for Al-$OH_{bridging}$, can not be observed in the spectra of Al-TPAs. BET surface area for the aluminum terephthalates were lower than 100 m^2/g.

Purification step: Effect of solvent type

The effect of solvent type and the amount of washing time in the pufication step were investigated. Aluminum terephthalates washed with 5xWater/1xDMF/2xhotDMF/ 2xMethanol (5w/1d/2hd/2m) and 5xWater/1xdmf/2xhotdmf/2xmethanol/2xmethanol

(5w/1d/2hd/2m/2m) were compared with the Al-TPA washed with 5 times water (5w). The crystal morphology of Al-TPAs were identical in spite of washing with different solvents (Figure A.16). The crystal size of Al-TPA 6 washed only with water (~10 μm) is larger than that of Al-TPA 7,8 washed with dmf and methanol (~2.5-3 μm). Altering the amount and type of solvent did not affect the crystal structure of Al-TPAs given in the XRD pattern of Figure A.17. The TGA curves of Al-TPAs washed with dmf and methanol are identical and degraded at 520°C (Figure A.18). According to the FTIR spectra presented in Figure A.19, there is observed little amount of decomposition in the C-H bonds of Al-TPA washed with additional methanol because of washing for many times. The peaks attributed to the bond between Al and $–COO^-$ and –OH bridging of the framework can not be observed in Al-TPAs. The doublet bands at 3100-3300 cm^{-1} correspond to (Al)O-H which are the characteristic peaks of boehmite can be apparently observed in the structure of each Al-TPAs.

BET surface area of aluminum terephthalates washed with dmf and methanol is slightly higher than that of Al-TPA 6 washed with only water, as using dmf and methanol provide removal of impurities from the pores of Al-TPA and yielding more free pores. Considering the characterization results of Al-TPA washed with different solvents there is no any difference between the structure of Al-TPAs and boehmite.

Activation step: Effect of activation temperature

As the volatilization temperature of BDC is 300°C, it may require higher temperature in the last step to remove unreacted BDC from the pores. Aluminum terephthalates were therefore synthesized by changing the activation temperatures as 330, 360, 410 and 420°C. According to the SEM images illustrated in Figure A.20, the crystal morphology of Al-TPA activated at 330 and 360°C appear similar but the crystal size of Al-TPA activated at 330°C (approximately 10 μm) is larger than that of Al-TPA activated at 360°C (~5 μm). Containing less impurity the crystals for Al-TPA activated at 360°C are clearer than Al-TPA activated 330°C. The XRD patterns (Figure A.21) and crystal structure of both Al-TPA activated at 330 and 360°C are identical, but different from that of Al-TPAs activated at 410 and 420°C. The structure of Al-TPA activated at 410 and 420°C were changed into different alumina form due to high temperature. From Figure A.22, the amount of nitric acid entrapped in the pores of Al-TPA activated at 330 and

360°C is approximately same and they decomposed at approximately 550°C to amorphous structure. As Al-TPAs activated at 410 and 420°C had been transformed into a different alumina during the synthesis procedure, the weight loss associated with decomposition could not be observed between that temperature scales from the TGA curves.

None of the Al-TPAs represent the doublet band at 3500 cm^{-1} corresponded to Al-$OH_{bridging}$. The transformation of Al-TPA structure activated at 410 and 420°C can be apparently observed from the FTIR spectra of Figure A.23.

Al-TPA 10 activated at 360°C has higher BET surface area than Al-TPA 9 activated at 330°C as activation at 360°C is more effective for the removal of impurities. The Al-PA activated at 410 and 420°C were changed into another alumina structure possessing higher BET surface area results than others.

Regarding the characterization results of aluminum terephthalates optimized experimental conditions for hydrothermal synthesis of Al-TPA was specified. Stirring the Al-TPAs for 5 h decreased the amount of water, nitric acid and unreacted BDC entrapped into the pores. The influence of washing amount and solvent type on the structure of Al-TPA can not be observed, so considering the time and performance consumption the purificaton step was performed by washing only with water instead of water, dmf and methanol. Activation temperature higher than 400°C altered and decomposed the structure of Al-TPA. The activation temperature of 330°C is sufficient for the removal of impurities from the pores. The BET results of Al-TPA were much smaller than that of MIL-53(Al). In addition the characterization results of each Al-TPAs synthesized by hydrothermal method overlap with that of boehmite. Performing a precrystallization step causes a new MOF structure called CAU-13 to form other than MIL-53(Al) or boehmite.

5.2. Solvothermal Synthesis of Al-TPA

The effect of crystallization temperature (130 and 200°C), solvent type (dmf/methanol and methanol) and activation temperature (130 and 200°C) on the crystal structure of aluminum terephthalates during the solvothermal synthesis of Al-TPA were evaluated. The characterization results were compared with the results discussed in literature (Loiseau et al. 2004, Rodrigue et al. 2012).

Crystallization step: Effect of crystallization temperature

Aluminum terephthalates were synthesized at different crystallization temperature, 130 and 200°C, via solvothermal synthesis. According to the SEM images in Figure 5.1, the crystals of Al-TPAs constitute of small particles and the crystal morphology of Al-TPAs resembles completely with that of MIL-53(Al) reported in literature.

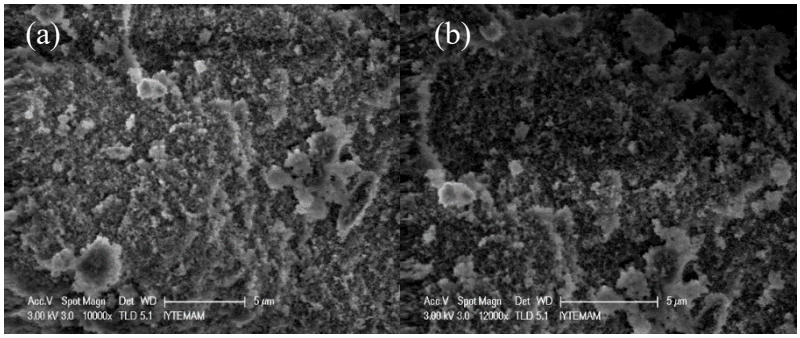

Figure 5.1. SEM images of Al-TPAs synthesized at a) 130 and b) 200°C.

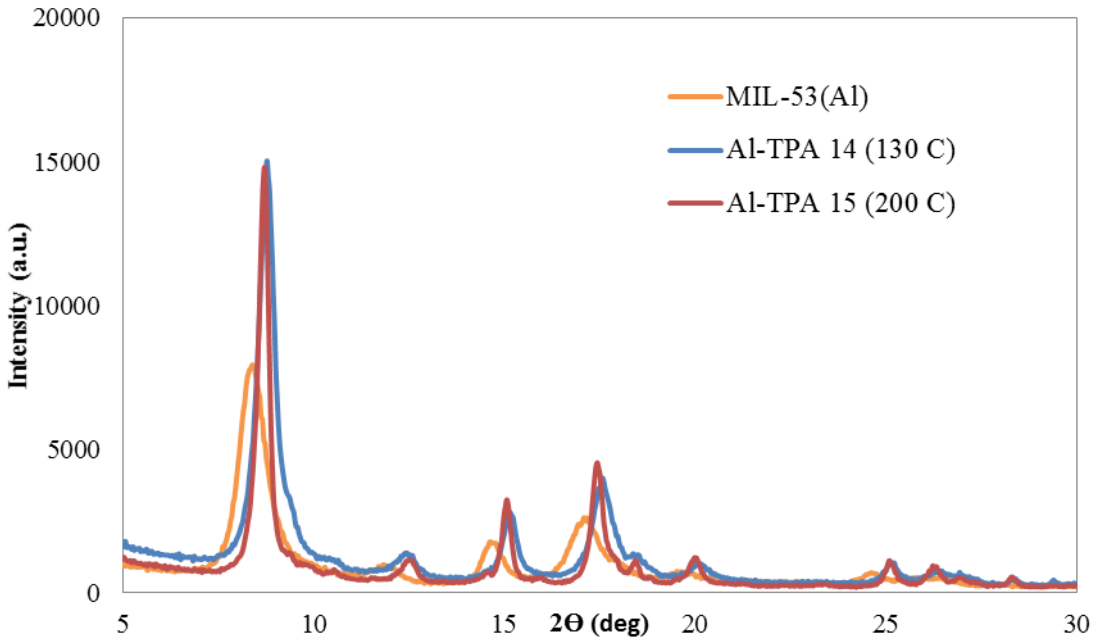

Figure 5.2. X-ray diffractometer patterns of Al-TPAs synthesized at 130 and 200°C.

Al-TPAs synthesized at different crystallization temperature have characteristic XRD peaks at 2θ= 8.45°, 12°, 14.7° and 17.2° which is same as MIL-53(Al). The sharp and high intensity peaks of XRD patterns illustrated in Figure 5.2 obviously demonstrated that the material is well crystalline and the peaks of synthesized Al-TPAs and MIL-53(Al) are in excellent agreement. XRD patterns of Al-TPAs are corresponded to that of MIL-53(Al) low temperature structure containing water molcules in their pores at room temperature. The solvothermal synthesis using DMF as solvent was efficient for the generation of desired MIL-53(Al) structure.

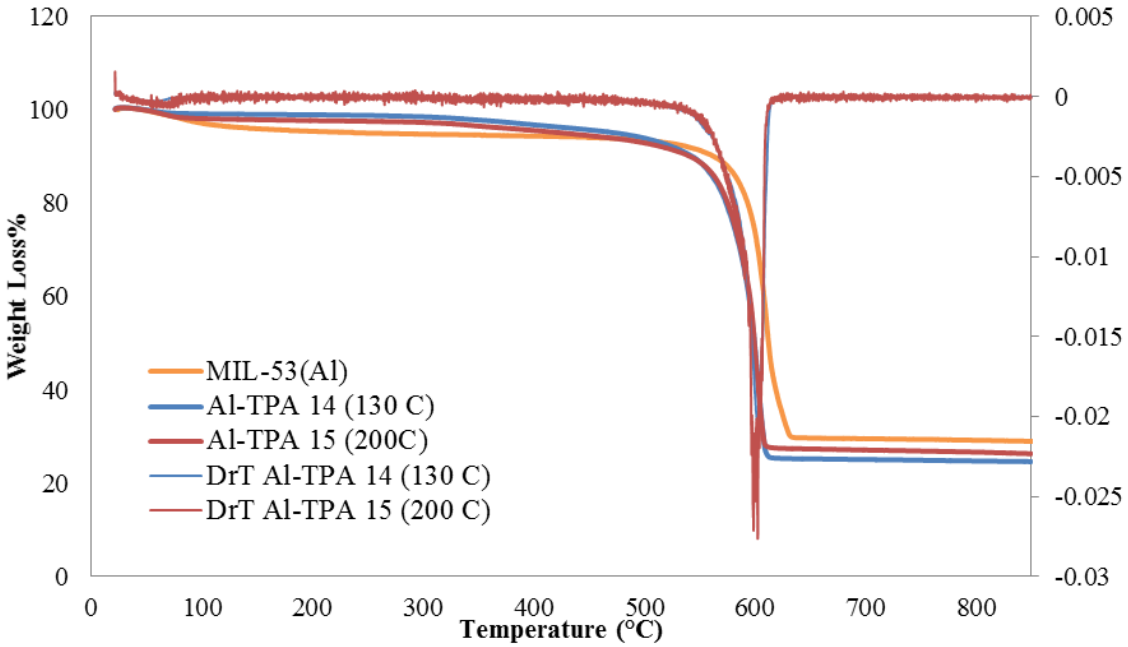

Figure 5.3. Thermogravimetric curves of Al-TPAs synthesized at 130 and 200°C.

Thermogravimetric profile of Al-TPAs given in Figure 5.3 match well with Al-TPA reported in literature. Al-TPAs does not contain any trace of nitric acid or unreacted BDC due to weight loss up to 550°C, proved that purification using dmf and water was efficient for the removal of impurities. Sharp decrease in weight loss at 550°C indicated the collapse of Al-TPAs to Al_2O_3 amorphous.

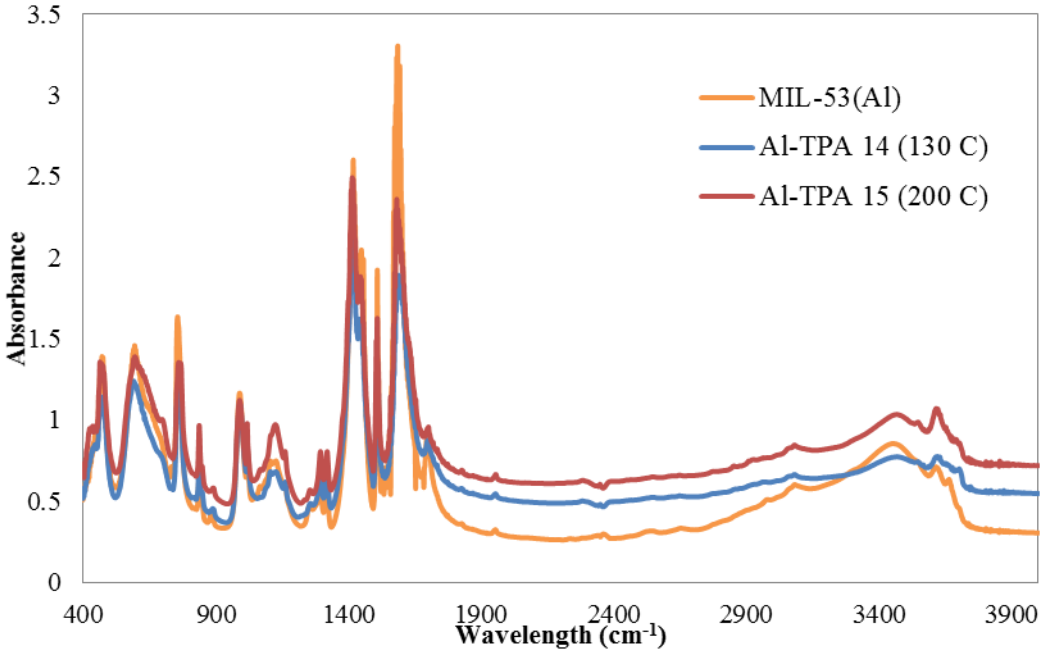

Figure 5.4. FTIR spectra of Al-TPAs synthesized at 130 and 200°C.

From Figure 5.4, MIL-53(Al) structure can be distinctively specified by bridging hydroxyls (μ_2-OH), located at the trans corner sharing $AlO_4(OH)_2$ octahedra, absorbing at 3500 cm^{-1} broad band. This broad band is obviously recognizable in the spectra of synthesized Al-TPAs. The low intensity shoulder at 3700 cm^{-1} near the broad band is attributed to OH groups in weak hydrogen bonding due to the unreacted BDC or water. The sharp and distinct peaks at 1400-1700 cm^{-1} are corresponded to symmetric (1505-1608 cm^{-1}) and antisymmetric (1420-1442 cm^{-1}) stretching modes of $–COO^-$ groups bonded with Al. The small and distinct peak at 1024 or 1019 cm^{-1} is due to the C-H modes of BDC. The position of this peak determines the large pore (1024 cm^{-1}) and narrow pore (1019 cm^{-1}) forms of Al-TPAs. That peak was observed at 1024 cm^{-1} for each Al-TPAs demonstrating that Al-TPAs are in the large pore form as Al-TPA is in the form of large pore structure at ambient temperature due to H_2O molecules presented in atmosphere (Loiseau et al. 2004, Hadjiivanov et al. 2016). Al-TPAs do not show any trace for the formation of boehmite structure specified from the doublet band at 3100-3300 cm^{-1}. The FTIR spectra of Al-TPAs was quite similar to Al-TPA reported in literature.

Table 5.1. BET surface areas of Al-TPAs synthesized at 130 and 200°C.

Crystallization Temperature (°C)	BET surface area (m^2/g)	Langmuir surface area (m^2/g)	Fixed experimental conditions
130	1133	1500	Solvothermal Synthesis t_{cry}= 72 h T_{act} = 200°C (72 h) $n_{Al/BDC/dmf}$=1/1.48/184.5
200	883	1250	
MIL-53(Al)	1140	1590	

The surface areas of Al-TPA synthesized at 130°C given in Table 5.1 are higher than that of Al-TPA synthesized at 200°C which contains more impurity into its pores as confirmed with FTIR spectra. Further experiments had been therefore proceeded by synthesis at 130°C. The BET surface areas of Al-TPAs are very high in the same manner of MIL-53(Al). The characterization results confirms that the synthesized materials are MIL-53(Al).

Purification Step: Effect of solvent type

Diminishing the amount of DMF solvent used during the solvothermal synthesis two Al-TPAs were purified with dmf/methanol and with only methanol in the purification step. The SEM images given in Figure 5.5 represent that the crystal morphologies of Al-TPAs resemble with each other and with MIL-53(Al) reported in literature. The crystals of Al-TPAs are smaller than 5 μm.

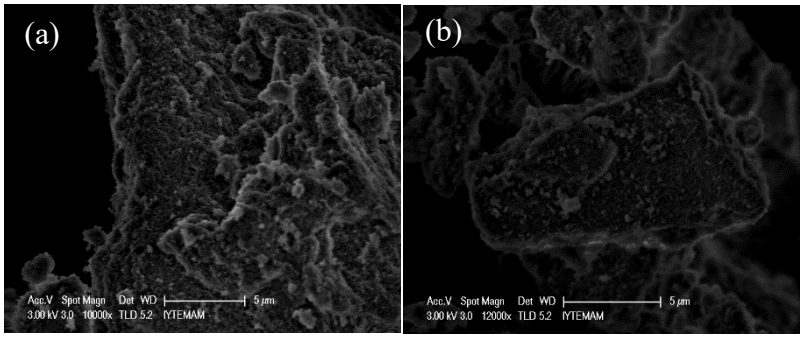

Figure 5.5. SEM images of Al-TPAs purified with a) dmf/methanol and b) methanol.

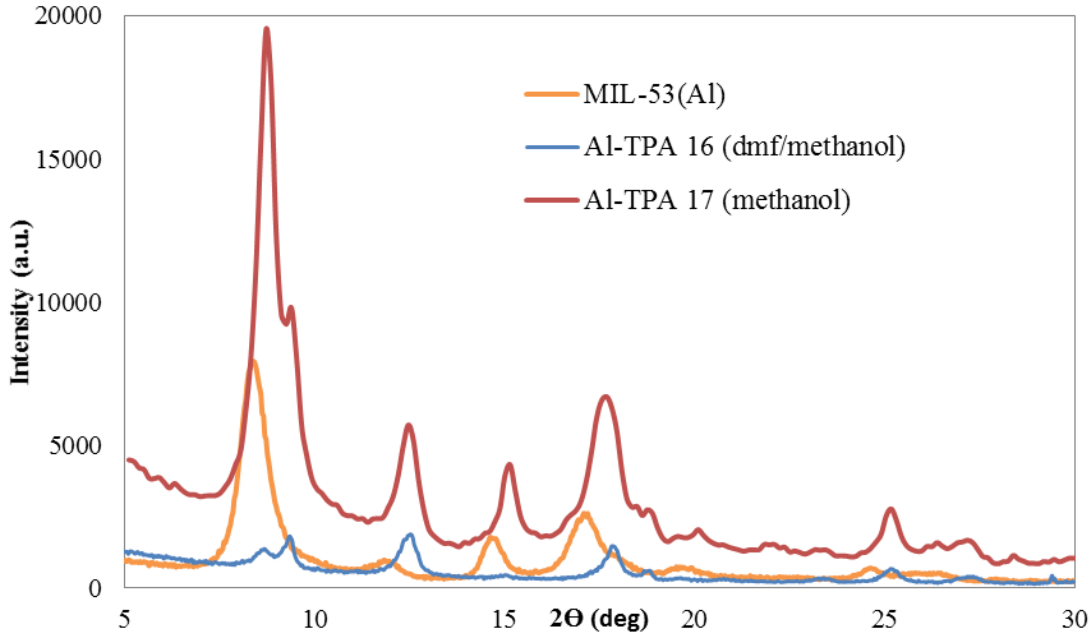

Figure 5.6. X-ray diffractometer patterns of Al-TPAs purified with dmf/methanol and with methanol.

The synthesized Al-TPAs and MIL-53(Al) show the similar peak positions in the XRD patterns illustrated in Figure 5.6. The patterns demonstrates that the synthesized material is MIL-53(Al).

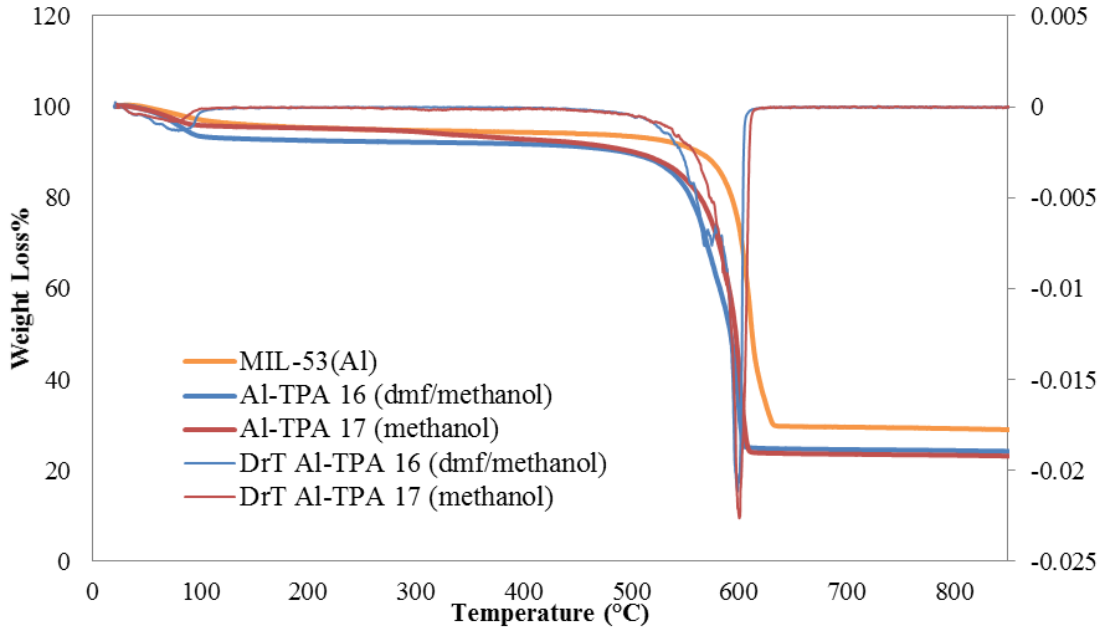

Figure 5.7. Thermogravimetric curves of Al-TPAs purified with dmf/methanol and with methanol.

TGA curves given in Figure 5.7 depicts initial weight loss due to dehydration process. Not containing unreacted BDC in its pores, washing only with methanol rather than using dmf solvent is effective for the removal of impurities. The second region of loss starting from 550°C is contributed by the disintegration of BDC linkers of Al-TPA framework.

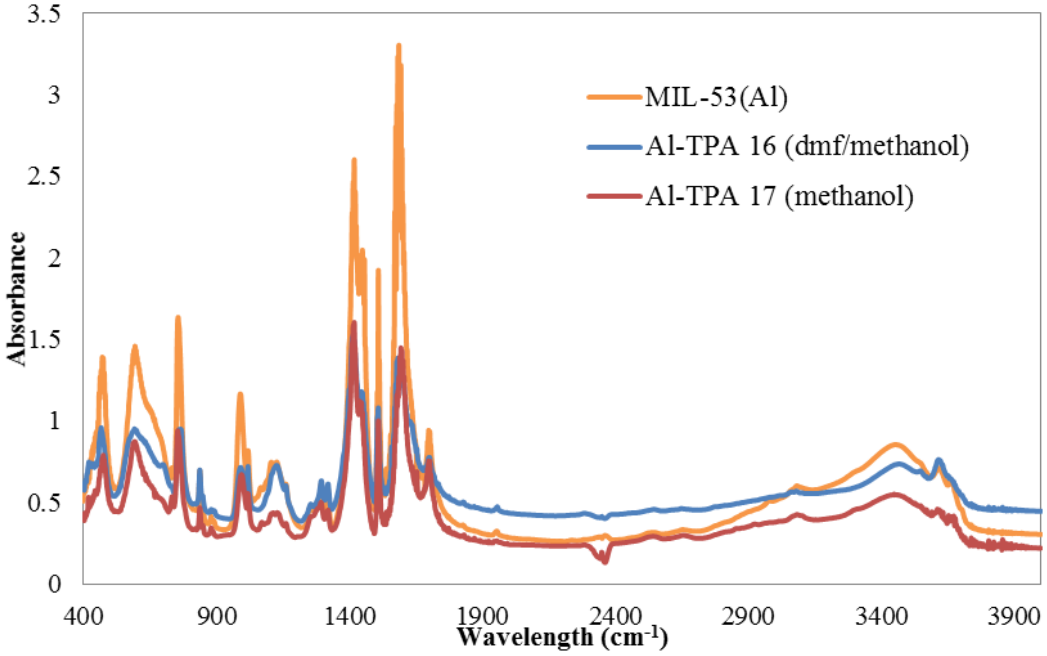

Figure 5.8. FTIR spectra of Al-TPAs purified with dmf/methanol and with methanol.

The broad band in the 3500 cm^{-1} range confirms the presence of bridging hydroxyl groups coordinated to aluminum. The sharp and distinct signals in the region of 1400-1700 cm^{-1} represented the coordination of aluminum and carboxylate (Figure 5.8).

Table 5.2. BET surface areas of Al-TPAs purified with dmf/methanol and with only methanol.

The amount of washing	BET surface area (m^2/g)	Langmuir surface area (m^2/g)	Fixed experimental conditions
Dmf/methanol	1051	1579	Solvothermal Synthesis T_{cry}= 130°C (72 h) T_{act} = 200°C (72 h) $n_{Al/BDC/dmf}$=1/1.48/184.5
methanol	1270	1330	
MIL-53(Al)	1140	1590	

The BET surface area of Al-TPA purified with methanol is higher than Al-TPA purified with dmf/methanol and MIL-53(Al). The complete removal of impurities was achieved by purification using methanol rather than using dmf solvent (Table 5.2).

Activation step: Effect of activation temperature

Al-TPAs were activated at different temperature, 130 and 200°C, in the thermal activation step. It can be seen from the SEM images given in Figure 5.9 that the crystal structure of Al-TPAs constitute of uneven particles smaller than 5 µm.

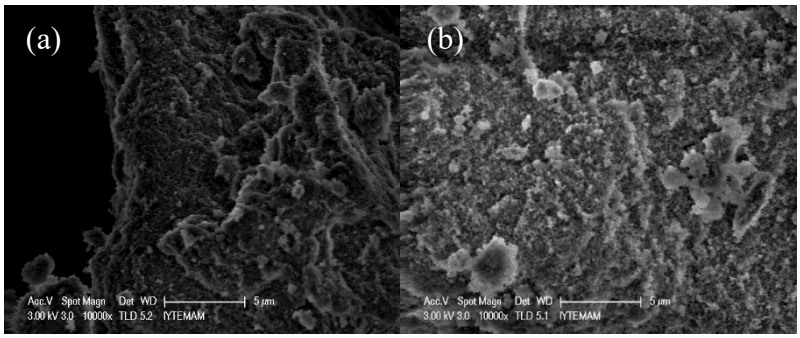

Figure 5.9. SEM images of Al-TPAs activated at a) 130 and b) 200°C.

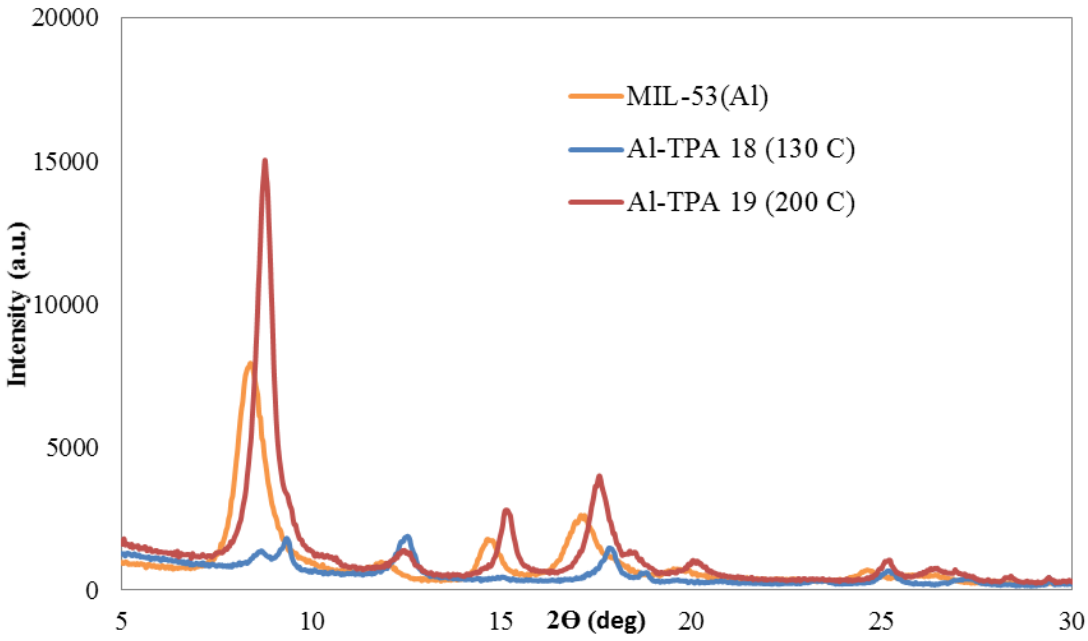

Figure 5.10. X-ray diffractometer patterns of Al-TPAs activated at 130 and 200°C.

It can be seen that XRD patterns presented in Figure 5.10 Al-TPAs exhibit similar peak positions, however, slightly different pattern due to the presence of remaining DMF or H_2O molecules in the pores. The crystal structure of Al-TPAs is similar to MIL-53(Al) as reported in literature.

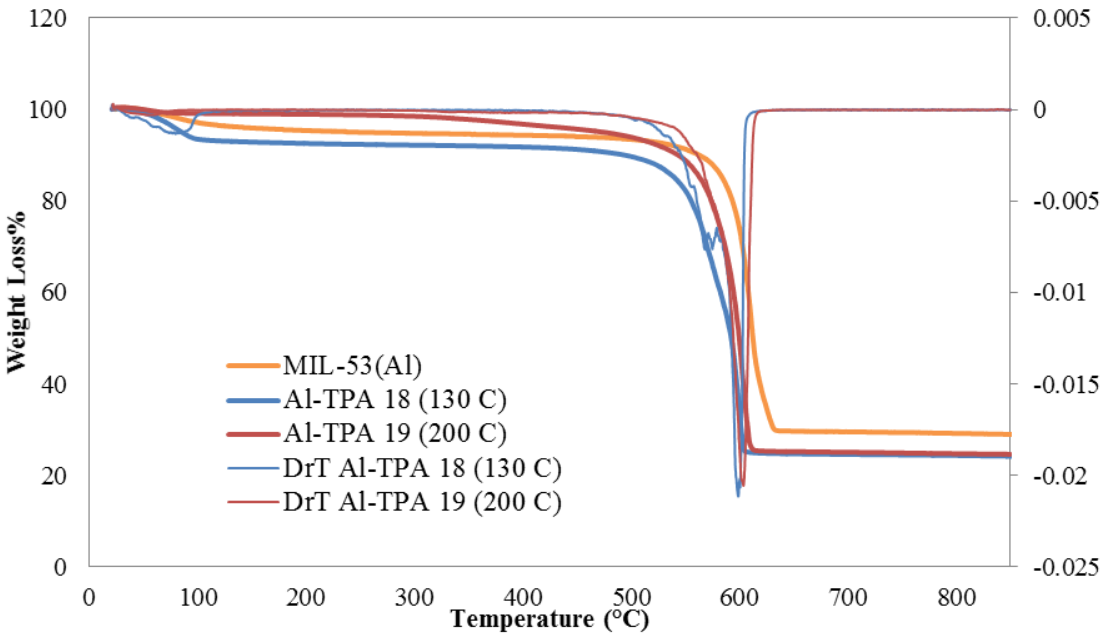

Figure 5.11. Thermogravimetric curves of Al-TPAs activated at 130 and 200°C.

Al-TPA 19 activated at 200°C contains less amount of water or nitric acid than Al-TPA 18 activated at 130°C as activation at higher temperature is more efficient for the elimination of such impurities. Each Al-TPAs does not contain any trace of unreacted BDC even activating at lower temperature than the volatilization temperature of BDC (300°C). This provide us that purification with dmf effectively removed the unreacted BDC. Consecutively, purification with methanol interchanged with dmf and was easily removed via heating. Drastic drop at 550°C marks the thermal degradation process of Al-TPA (Figure 5.11).

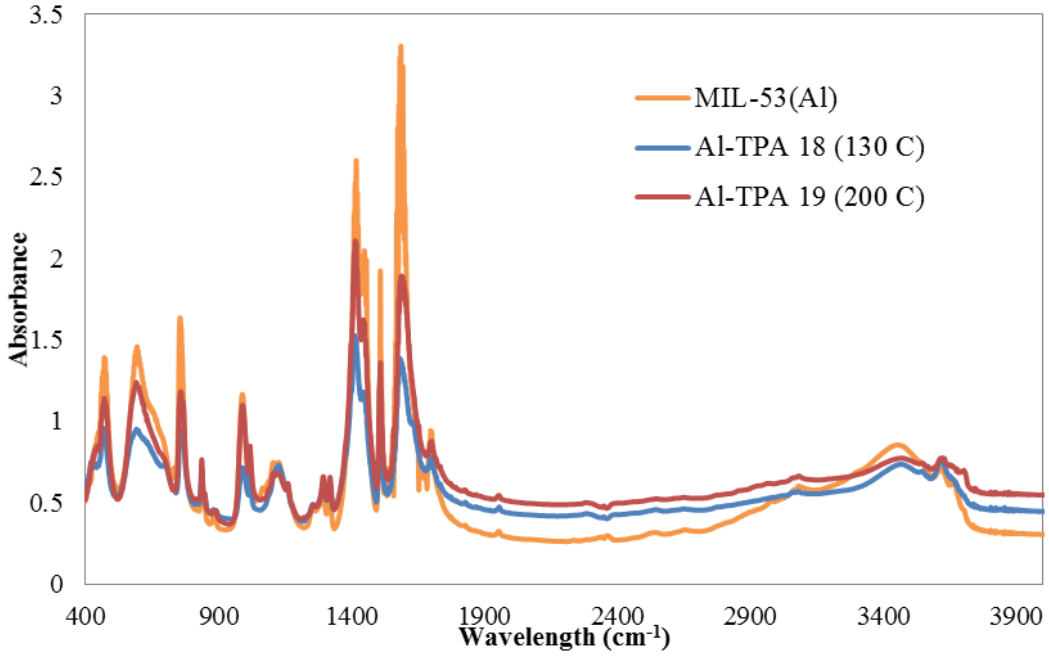

Figure 5.12. FTIR spectra of Al-TPAs activated at 130 and 200°C.

According to Figure 5.12 FTIR spectra of Al-TPAs exactly matched with that of Al-TPA reported in literature due to possessing the characteristic peaks between 1400-1700 cm^{-1} and 3500 cm^{-1}.

Table 5.3. BET surface areas of Al-TPAs activated at 130 and 200°C.

Activation Temperature (°C)	**BET surface area (m^2/g)**	**Langmuir surface area (m^2/g)**	**Fixed experimental conditions**
130	1051	1579	Solvothermal Synthesis T_{cry}= 130°C (72 h) t_{act} = 72 h $n_{Al/BDC/dmf}$=1/1.48/184.5
200	1133	1500	
MIL-53(Al)	1140	1590	

Al-TPA 19 activated at 200°C has higher BET surface area than Al-TPA 18 activated at 130°C. The surface area of Al-TPA The removal of impurities from the cavities of Al-TPA can be also accomplished even activation at lower temperature (Table 5.3).

The characterization and surface area results match well with the literature reports. Al-TPA has been successfully synthesized via solvothermal synthesis route. The XRD patterns of Al-TPA corresponded to MIL-53(Al) low temperature structure (Louiseau et al) indicated that Al-TPAs were changed into their narrow pore domain containing water molecules at ambient temperature after activation step. The optimized experimental conditions were determined considering the characterization results. Crystallization at 130°C rather than 200°C yields Al-TPA with higher surface area. Both Al-TPA purified with dmf/methanol and methanol represents high surface area, however, purification using only methanol is more favorable due to environmental and time-related concerns. The surface areas of Al-TPAs activated at 130°C and 200°C are found to be very close to each other. Due to energy consumption, activation at 130°C is more preferable in the activation step. The XRD patterns and surface area results confirmed that the synthesized Al-TPA has a typical MIL-53(Al) structure reported in literature.

5.3. Hydro-Solvothermal Synthesis of Al-TPA

Hydro-solvothermal synthesis of aluminum terephthalates were maintained following the two different procedures of Zhu et al. (2016) and Zhou et al. (2013). One of them suggested the 130°C crystallization time and washing with dmf for 6 h, whereas the other one offered that the 150°C crystallization time and washing with dmf for 20 h. For the first synthesis route, the effect of crystallization time (48 and 72 h), activation temperature (130 and 180°C) and activation time (12 and 72 h) and for the second synthesis route, the effect of crystallization time (48 and 72 h) and activation (12 and 72 h) on aluminum terephthalates were investigated.

Crystallization step: Effect of crystallization time

Al-TPAs were prepared in a mixed solvent of dmf and water during crystallization step. The crystallization step in a Teflon-lined steel autoclave was performed at 150°C for 48 and 72 h and then Al-TPAs were activated at 180°C for 12 h. SEM images of Al-TPA given in Figure 5.13 indicated that Al-TPA crystallized for 72 h has larger and aggregated three dimensonal particles possessing 5 μm size.

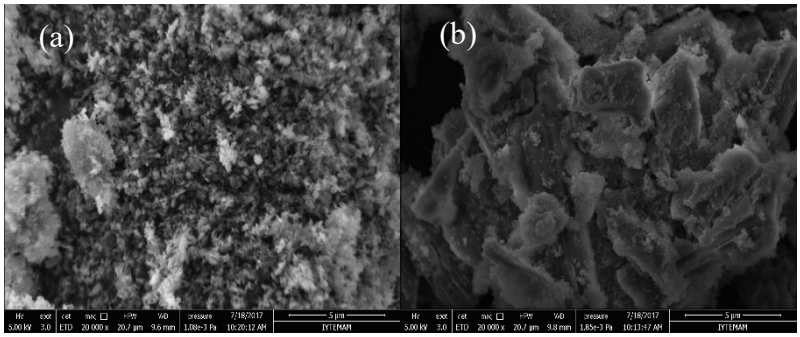

Figure 5.13. SEM images of Al-TPAs crystallized for a) 48 and b) 72 h.

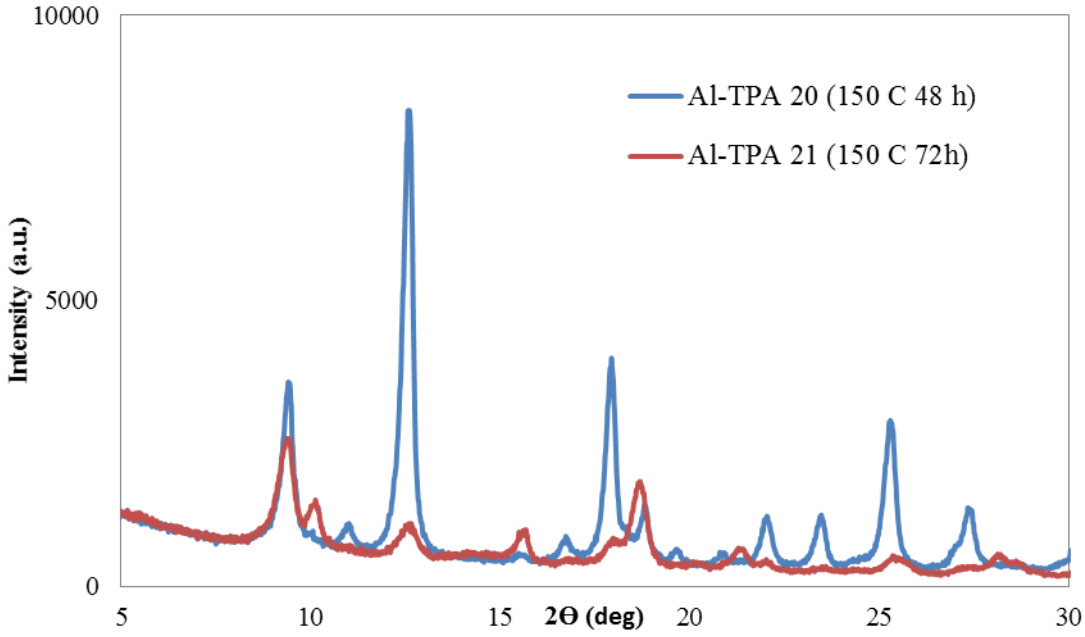

Figure 5.14. X-ray diffractometer patterns of Al-TPAs crystallized for 48 and 72 h.

According to the XRD patterns indicated in Figure 5.14, the patterns for Al-TPA 20 crystallized for 48 h is identical for MIL-53(Al) high temperature reported in literature. The characteristic peaks for Al-TPA synthesized for 48 h are 2θ= 9.45, 12.6, 17.9 and 25.3° and for Al-TPA synthesized for 72 h are 2θ= 9.47, 12.7, 15.7 and 18.7°. Difference in crystal directions indicate that different crystal structures were formed for each Al-TPAs. The small shoulder seen in the pattern of Al-TPA 21 crystallized for 72 h is due to retaining its narrow pore structure upon activation step.

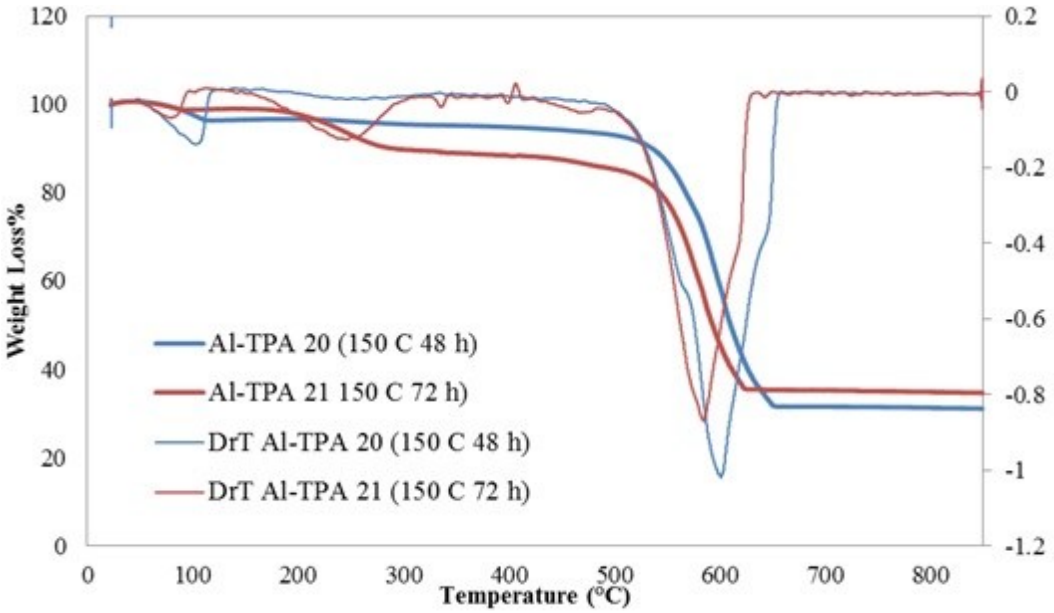

Figure 5.15. Thermogravimetric curves of Al-TPAs crystallized for 48 and 72 h.

According to the Figure 5.15, initial decrease in the weight up to 130°C indicates that Al-TPA crystallized for 48 h contains more water molecules in its pores. Due to the weight loss up to 360°C Al-TPA crystallized for 72 h contains more unreacted TPA in the cavities of the framework. Al-TPAs decomposed with 66% weight loss at about 440°C.

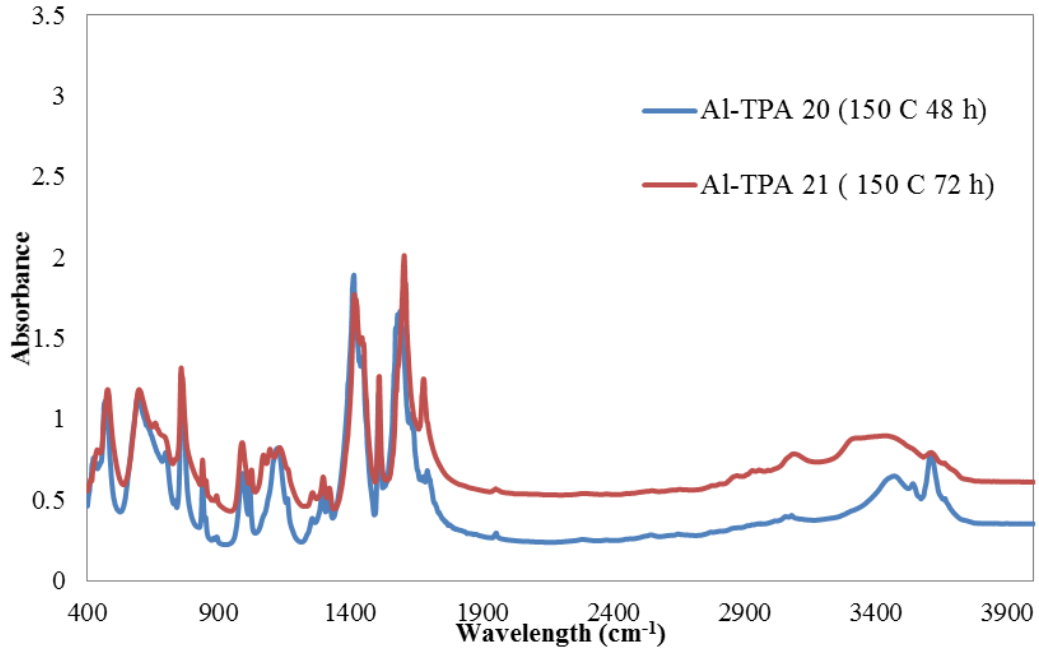

Figure 5.16. FTIR spectra of Al-TPAs crystallized for 48 and 72 h.

From Figure 5.16, IR spectra of synthesized Al-TPAs are in good agreement with that of MIL-53(Al) reported in literature. The peaks between 1400-1700 cm^{-1}, attributed to the coordination of aluminum and carboxylate ion, are effectively formed for both Al-TPAs. The characteristic broad band were seen for Al-TPAs at 3500 cm^{-1} assigning to bridging –OH. Conducting the synthesis in a mixture of dmf and water is effective for the formation of bonds required for Al-TPA framework. The small shoulder at 3600 cm^{-1} indicates that Al-TPA crystallized for 48 h contain more water molecules in the pores of its structure as also can be seen from TGA curves. The peak formed at 1019 cm^{-1} for Al-TPA crystallized for 72 h indicated that Al-TPA retain its narrow pore structure form after activation step, which can also be investigated from XRD spectra.

Table 5.4. BET surface areas of Al-TPAs crystallized for 48 and 72 h.

Crystallization Time (hours)	**BET surface area (m^2/g)**	**Langmuir surface area (m^2/g)**	**Fixed experimental conditions**
48	705	1009	Hydro-solvothermal T_{cry}= 150°C T_{act} = 180°C (12 h) Washing=5w/1d(6h)/1m(20h)
72	782	1112	
MIL-53(Al)$_{lt}$	950	-	

As can be observed from Table 5.4, BET surface area of the synthesized Al-TPAs are very close to MIL-53(Al) reported in literature. The BET surface area of Al-TPA crystallized for 72 h is higher than that of Al-TPA crystallized for 48 h. Regarding the characterization and BET surface area results, crystallization for 48 h is insufficient for the effective incorporation of complete Al-TPA framework.

Activation step: Effect of activation temperature

Two Al-TPAs were crystallized at 150°C for 72 h and then activated at 130 and 180°C for 72 h. Figure 5.17 representing the SEM images of Al-TPAs demonstrated that increasing activation temperature changed the crystal morphologies and decreased the size of uneven crystals.

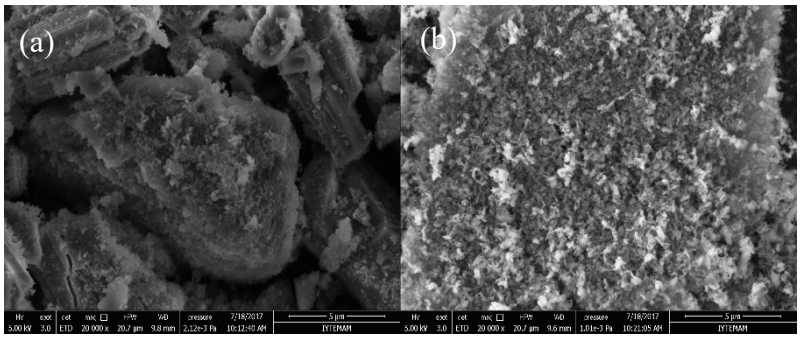

Figure 5.17. SEM images of Al-TPAs activated at a) 130 and b) 180°C.

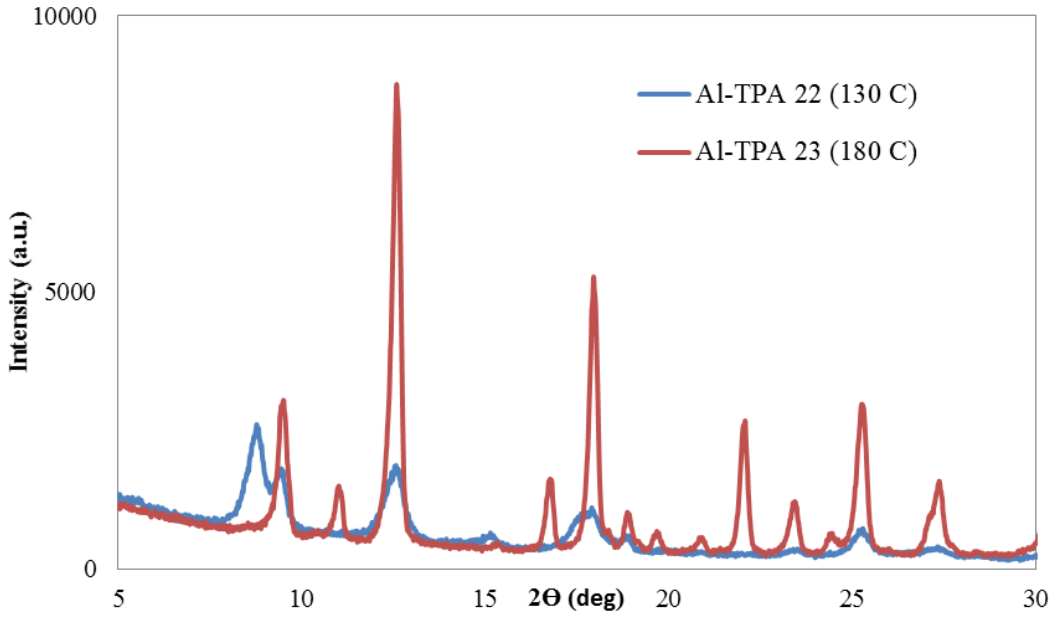

Figure 5.18. X-ray diffractometer patterns of Al-TPAs activated at 130 and 180°C.

The XRD pattern Al-TPA activated at 180°C is good agreement with MIL-53(Al) reported in literature. The characteristic peaks for Al-TPA 23 activated at 180°C are 2θ= 9.47, 12.6, 17.9, 25.3° as stated in literature. The Al-TPA 22 activated at 130°C has a shoulder at 2θ= 9.45° due to retaining its narrow pore structure upon activation. Difference in XRD patterns suggest that their crystal phase structure and degree of crystallinity are different (Figure 5.18).

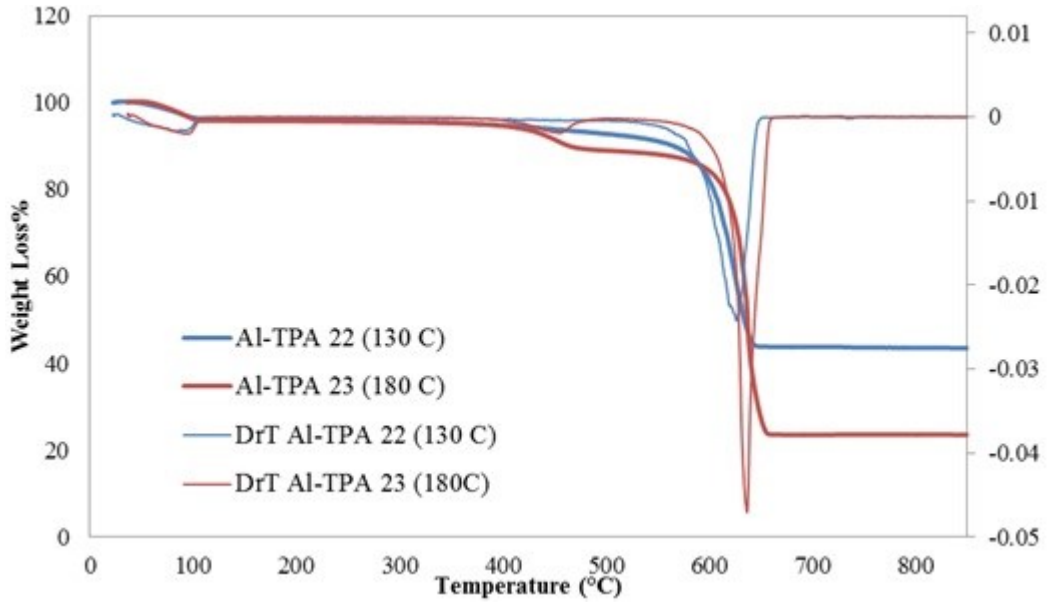

Figure 5.19. Thermogravimetric curves of Al-TPAs activated at 130 and 180°C.

Both Al-TPAs contain a little amount of water molecules in its pores. As can be seen from the Figure 5.19, drastic drop of loss at 520°C reveals the thermal decomposition process. Considering the decomposition weight loss Al-TPA 23 activated at 180°C possess more incorporated Al-TPA structure.

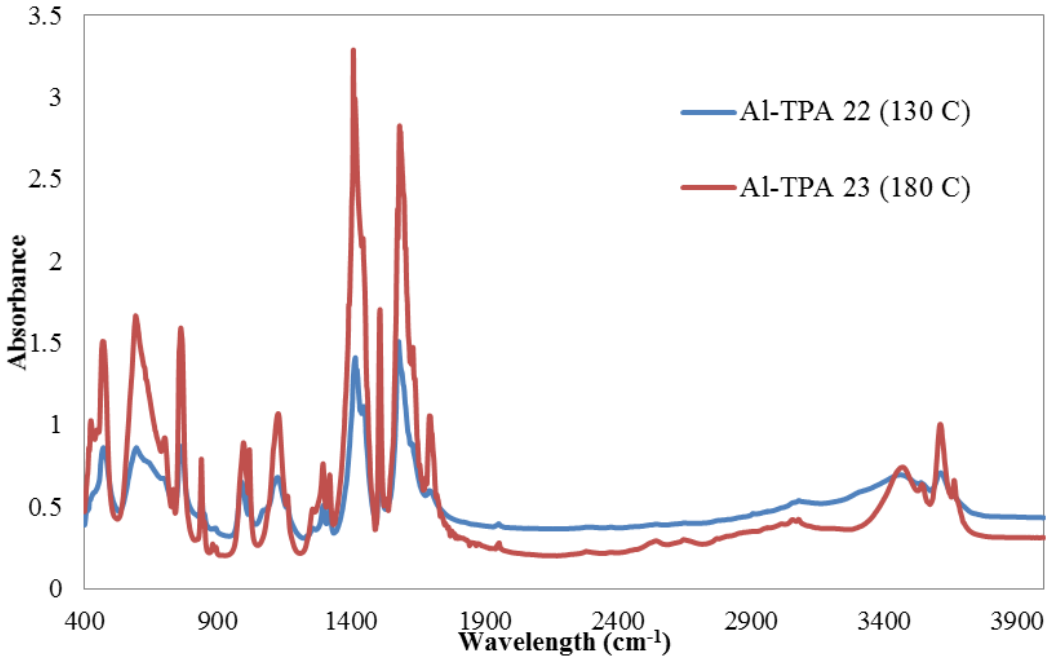

Figure 5.20. FTIR spectra of Al-TPAs activated at 130 and 180°C.

Both Al-TPAs represent the characteristic peaks of MIL-53(Al) structure which are the sharp peaks at 1400-1700 cm^{-1} corresponding to the bond between aluminum and carboxylate, and the broad band at 3500 cm^{-1} corresponding to bridging hydroxyl groups. (Figure 5.20).

Table 5.5. BET surface areas of Al-TPAs activated at 130 and 180°C.

Activation Temperature (°C)	BET surface area (m^2/g)	Langmuir surface area (m^2/g)	Fixed experimental conditions
130	902	1288	Hydro-solvothermal T_{cry}= 150°C (72 h) t_{act} = 72 h Washing=5w/1d(6h)/1m(20h)
180	653	947	
MIL-53(Al)$_{lt}$	950	-	

From Table 5.5, BET surface area of Al-TPA activated at 130°C, which is very close to that of MIL-53(Al) reported in literature, is higher than that of Al-TPA activated at 180°C. Activation at 130°C is more effective due to the energy concerns.

Activation step: Effect of activation time

Al-TPAs were synthesized in an autoclave at 150°C for 72 h and then activated at 180°C for 12 and 72 h. Maintaining the procedure with different activation time yielded Al-TPAs with disparate crystal structures as can be proved from SEM images in Figure 5.21. Al-TPA activated for 72 h possess very small uneven crystals.

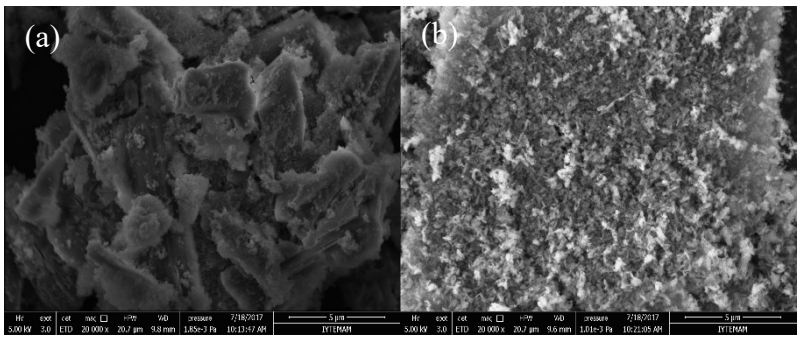

Figure 5.21. SEM images of Al-TPAs activated for a) 12 and b) 72 h.

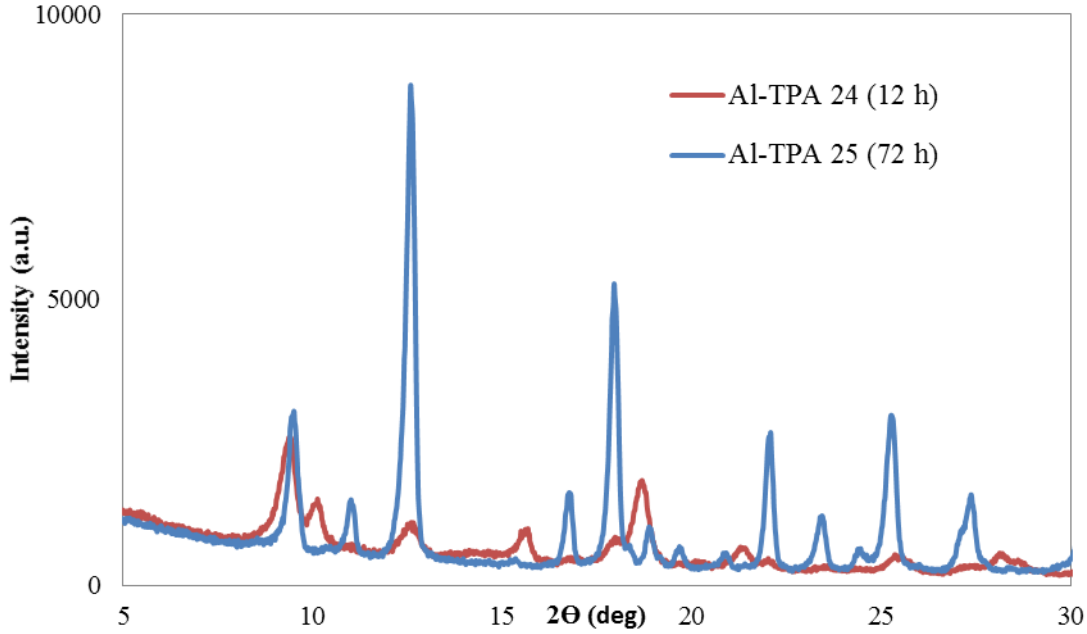

Figure 5.22. X-ray diffractometer patterns of Al-TPAs activated for 12 and 72 h.

As can be observed from Figure 5.22, XRD pattern of Al-TPA activated for 72 h, possessing large pore strucutre, is substantially in agreement with that of MIL-53(Al) high temperature reported in literature. The structure of Al-TPA activated for 12 h contains more impurity in its structure.

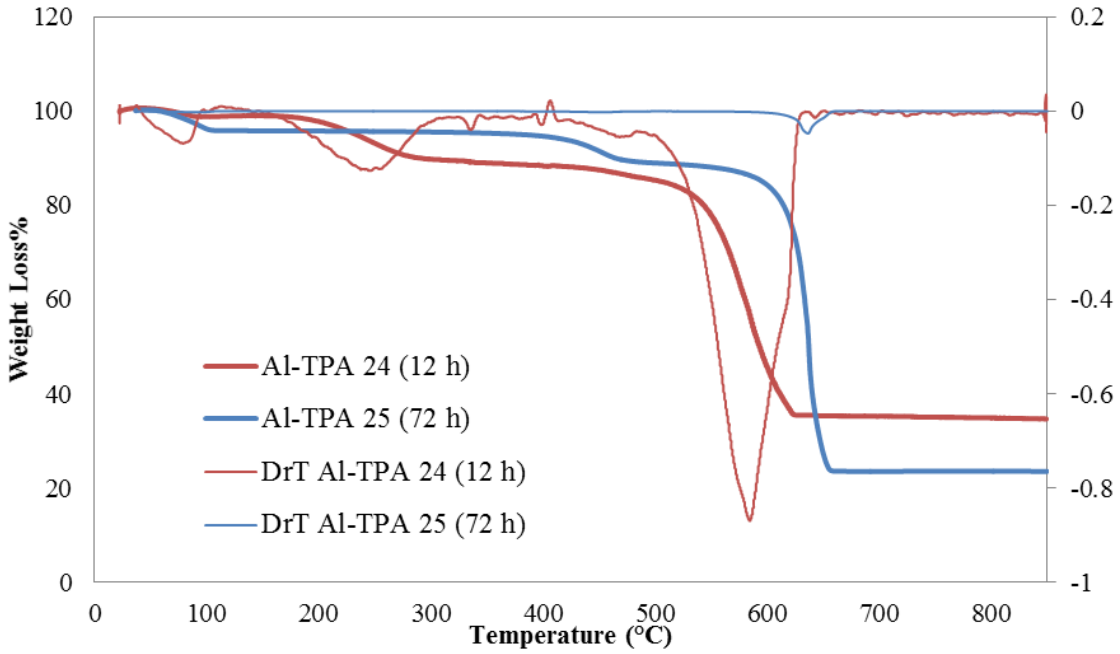

Figure 5.23. Thermogravimetric curves of Al-TPAs activated for 12 and 72 h.

According to the initial decrease in mass up to 100°C Al-TPA activated for 72 h contain more water molecules in its structure. Al-TPA activated for 12 h represented a weight loss in the 170-350°C range which arose from the removal of unreacted BDC from the pores whereas Al-TPA activated for 72 h does not contain any unreacted BDC. Activation for 72 h is therefore more effective for the elimination of impurities from the structure. Sharp decrease in weight loss at 515°C arose from the collapse of Al-TPAs (Figure 5.23).

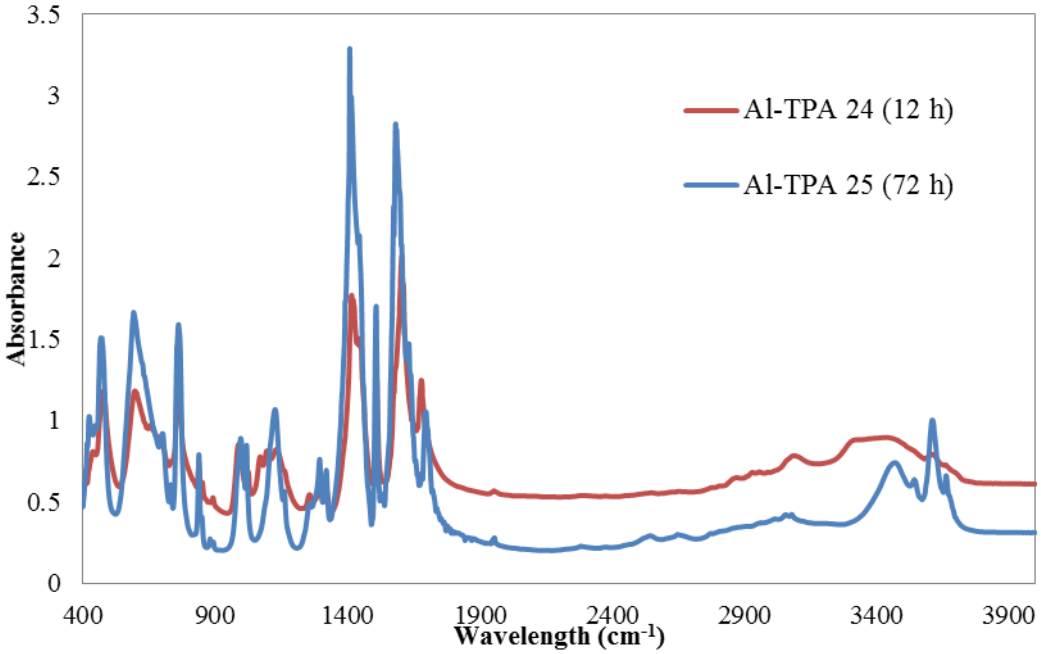

Figure 5.24. FTIR spectra of Al-TPAs activated for 12 and 72 h.

According to the FTIR spectra given in Figure 5.24, carboxylate groups (1400-1700 cm^{-1}), bridging hydroxyl groups (3500 cm^{-1}) and Al-OH bond (1020 cm^{-1}) can be seen clearly. The bond structure of Al-TPAs were formed properly. Al-TPA activated for 72 h contain more water molecules in its structure as also can be seen from the TGA curves.

Table 5.6. BET surface areas of Al-TPAs activated for 12 and 72 h.

Activation Time (hours)	BET surface area (m^2/g)	Langmuir surface area (m^2/g)	Fixed experimental conditions
12	782	1112	Hydro-solvothermal T_{cry}= 150°C (72 h), T_{act} = 180°C Washing=5w/1d(6h)/1m(20h)
72	653	947	
MIL-53(Al)$_{lt}$	950	-	

From Table 5.6, Al-TPA activated for 12 h has higher BET surface area than Al-TPA activated for 72 h. However, considering the characterization results activation for 72 h was more effective for the complete removal of impurities from the structure.

Crystallization step: Effect of crystallization time (for crystallization at °130 C)

Al-TPAs were synthesized at 130°C for 48 and 72 h and washed with water, dmf and methanol. They were then activated at 150°C for 12 h. Al-TPAs having different crystal morphologies were given in Figure 5.25. Al-TPA crystallized for 72 hour has larger three dimensional cubic shaped crystals.

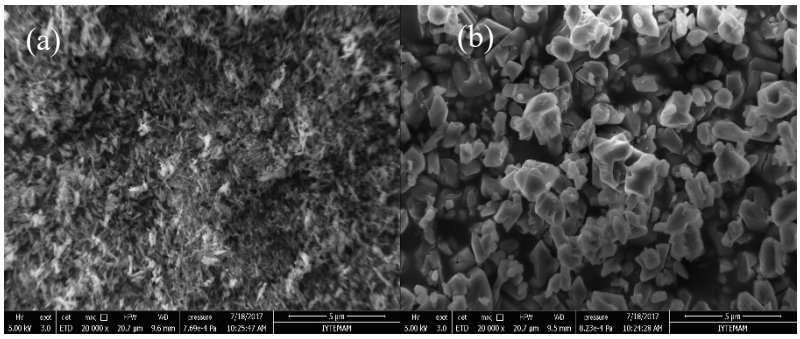

Figure 5.25. SEM images of Al-TPA crystallized for a) 48 and b) 72 h.

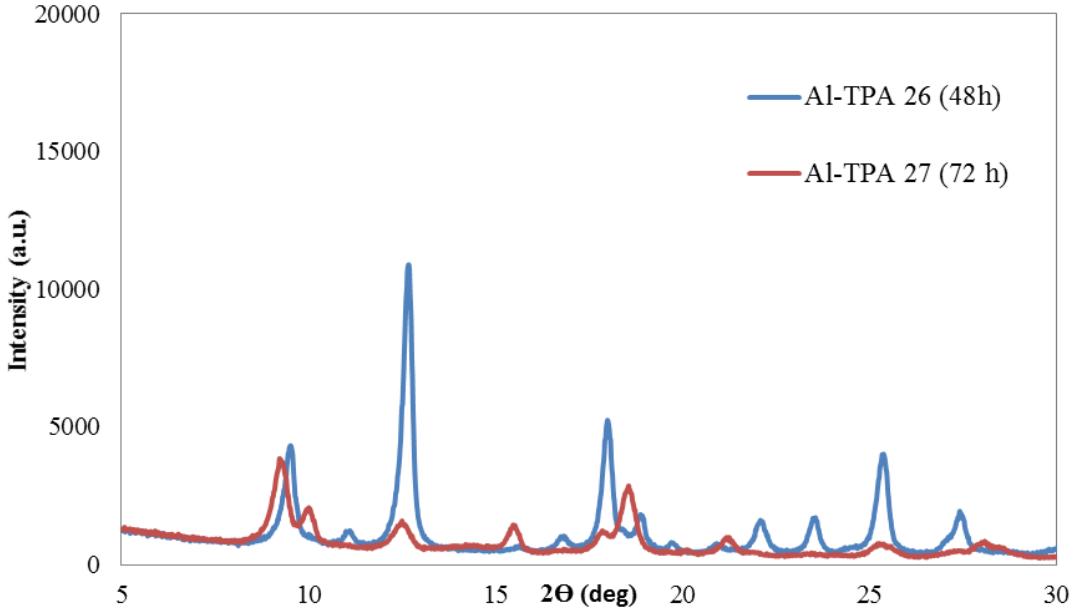

Figure 5.26. X-ray diffractometer patterns of Al-TPA crystallized for 48 and 72 h.

Figure 5.26 demonstrated that XRD pattern of Al-TPA crystallized for 48 h was similar to that of MIL-53(Al) high temperature (having large pore structure) reported in literature. Crystallization for 48 h was also proposed by Do et al. for the synthesis of Al-TPA. Increasing the crystallization time from 48 to 72 h changed the crystal structure of Al-TPA.

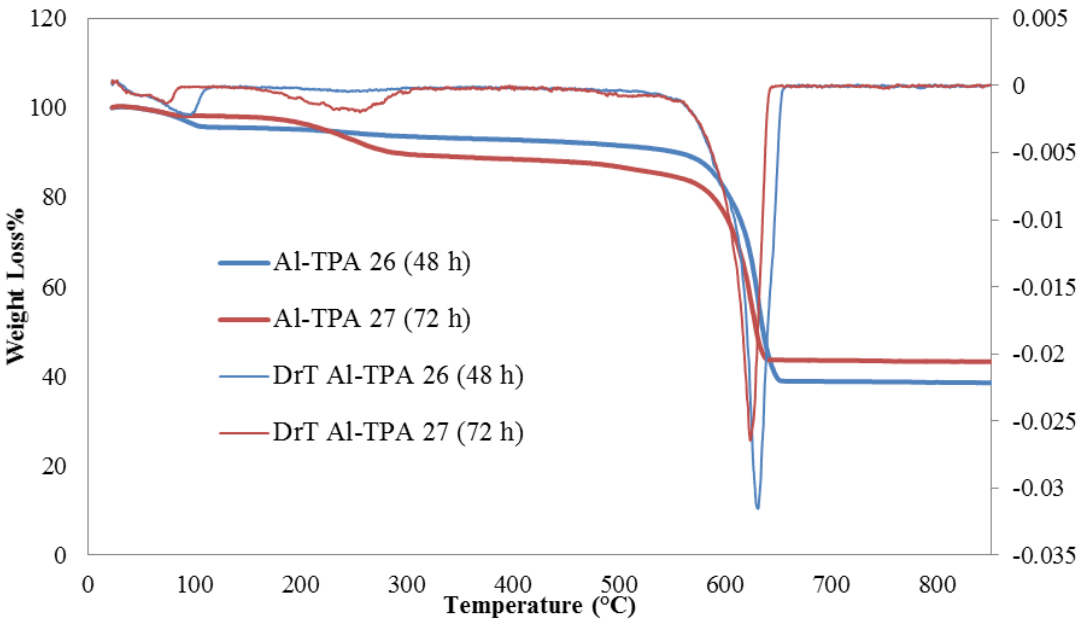

Figure 5.27. Thermogravimetric curves of Al-TPA crystallized for 48 and 72 h.

Al-TPA crystallized for 48 h contain less impurity than Al-TPA crystallized for 72 h. There remain more nitric acid and water molecules in Al-TPA crystalized for 72 h and for 48 h due to the weight loss at 73 and 96°C, respectively. Al-TPAs started to decompose at 550°C (Figure 5.27).

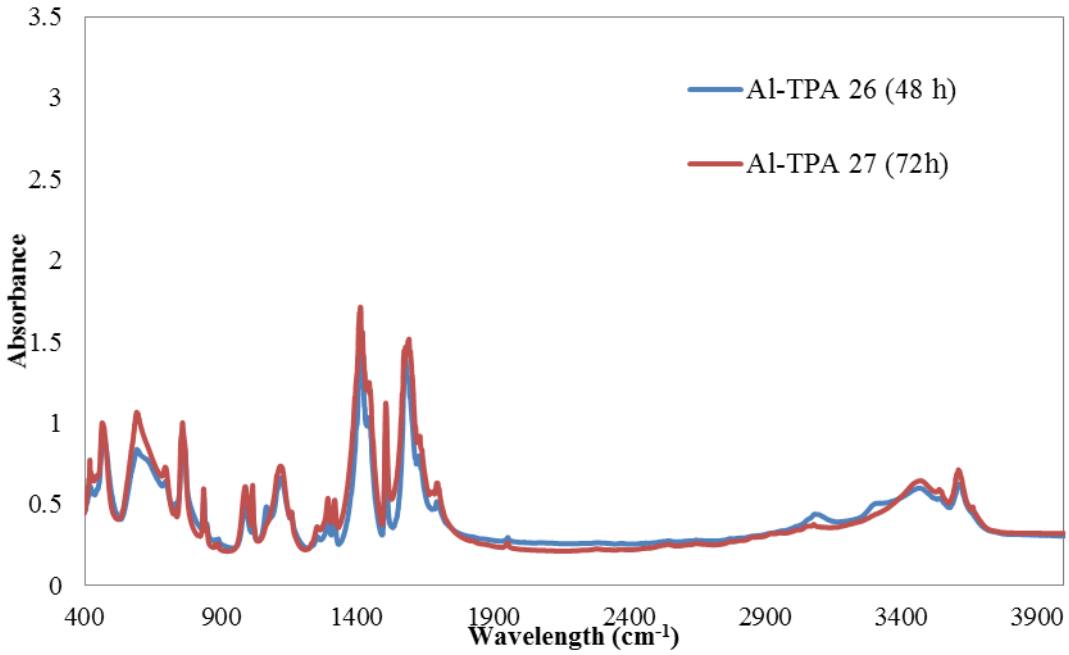

Figure 5.28. FTIR spectra of Al-TPAs crystallized for 48 and 72 h.

The FTIR spectra of Al-TPAs were consistent with that of MIL-53(Al). The sharp peaks between 1400-1700 cm^{-1} representing the $–COO^-$ groups coordinated to Al^{+3} metal center and broad band at 3500 cm^{-1} corresponding to the bridging hydroxyl groups approved the formation of Al-TPA structure (Figure 5.28).

Table 5.7. BET surface areas of Al-TPAs crystallized for 48 and 72 h.

Crystallization Time (hours)	BET surface area (m^2/g)	Langmuir surface area (m^2/g)	Fixed experimental conditions
48	703	1014	Hydro-solvothermal Synthesis T_{cry}= 130°C T_{act} = 150°C (12 h) Washing=5w/1d(24h)/1m(20h)
72	717	1027	
MIL-53(Al)$_{lt}$	950	-	

From Table 5.7 BET surface area of Al-TPA crystallized for 48 h is less than that of Al-TPA crystallized for 72 h. However, according to the characterization results the desired Al-TPA crystal structure was effectively formed via crystallization for 48 h.

Activation step: Effect of activation time (for crystallization at °130 C)

Al-TPAs were crystallized at 130°C for 72 h and then activated at 150°C for 12 and 72 h. Increasing activation time altered the crystal morphologies of Al-TPAs given in Figure 5.29 Al-TPA activated for 72 h has smaller and uneven crystals.

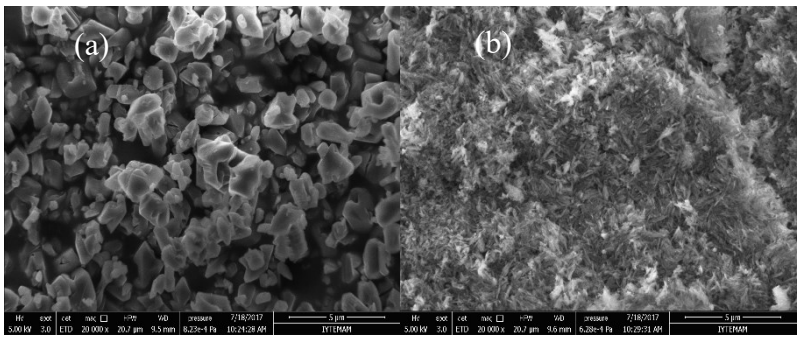

Figure 5.29. SEM images of Al-TPA activated for a) 12 and b) 72 h.

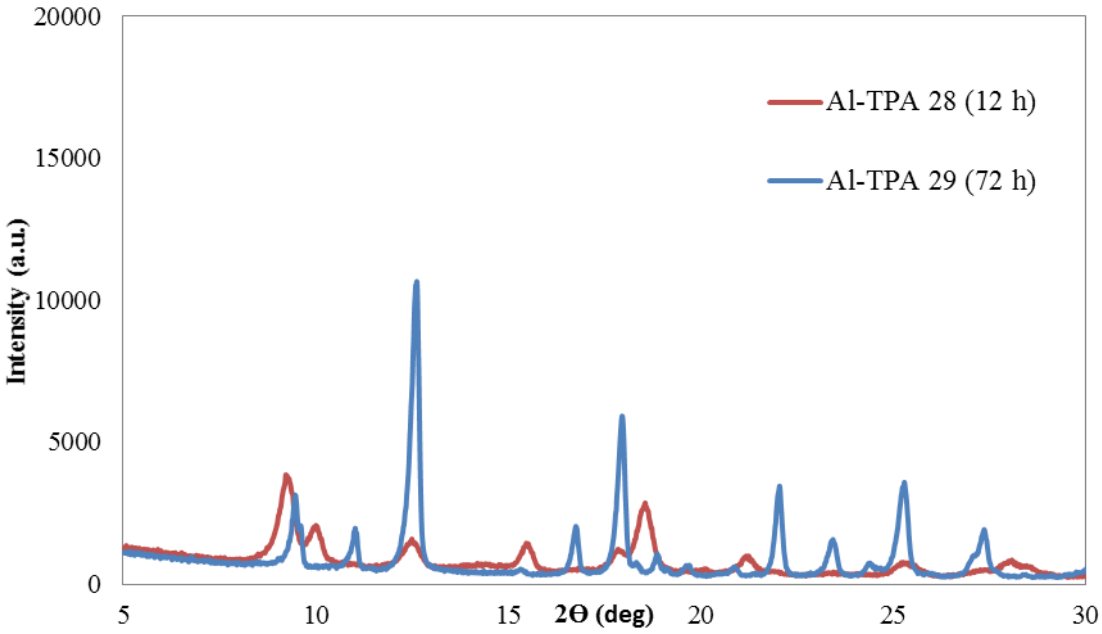

Figure 5.30. X-ray diffractometer of Al-TPA activated for 12 and 72 h.

Al-TPA activated for 72 h has characteristic peaks at 2θ= 9.49, 12.6, 17.9, 22 and 25.3° which are similar to that reported in literature. The desired crystal structure can not be achieved for Al-TPA activated for 12 h containing impurities into its pores (Figure 5.30).

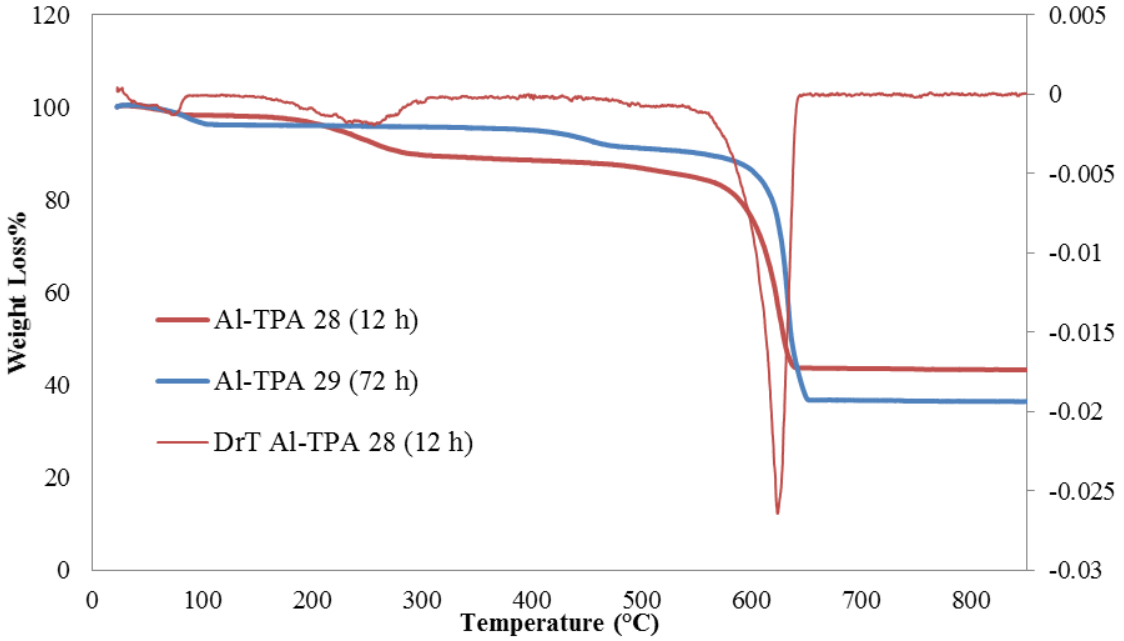

Figure 5.31. Thermogravimetric curves of Al-TPA activated for 12 and 72 h.

Considering the TGA curves in Figure 5.31 activation for 12 h contains more nitric acid, water molecules and unreacted BDC into its cavities. Increasing the activation time from 12 h to 72 h eliminated the unreacted BDC from the pores of the structure effectively.

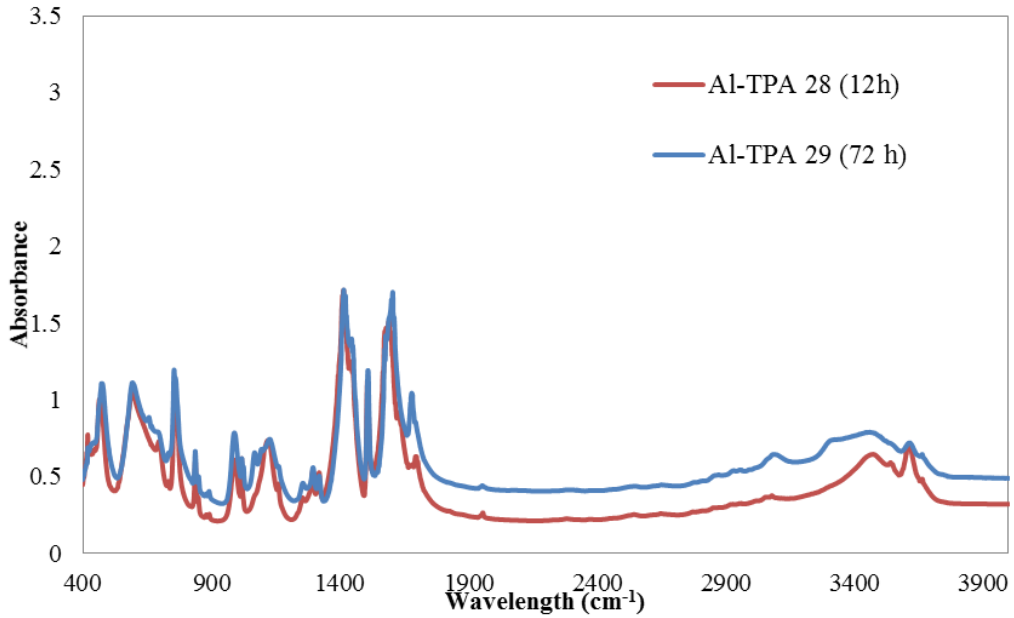

Figure 5.32. FTIR spectra of Al-TPA activated for 12 and 72 h.

As given in Figure 5.32 the spectra of synthesized Al-TPAs are quite similar that of MIL-53(Al). Al-TPAs exhibit vibrational bands between 1400-1700 cm^{-1} assigned to $–COO^-$ stretchings and broad band at 3500 cm^{-1} for the bridging hydroxyl groups. The small shoulder at 3650 cm^{-1} showed that more water molecules presented in the pores of Al-TPA activated for 12 h, which can be also obviously demonstrated from the initial weight loss in TGA curves.

Table 5.8. BET surface area of Al-TPAs activated for 12 and 72 h.

Activation Time (hours)	**BET surface area (m^2/g)**	**Langmuir surface area (m^2/g)**	**Fixed experimental conditions**
12	717	1027	Hydro-solvothermal Synthesis T_{cry}= 130°C (72 h) T_{act} = 150°C Washing=5w/1d(24h)/1m(20h)
72	650	940	
MIL-53(Al)$_{lt}$	950	-	

From Table 5.8, BET surface area results of Al-TPA activated for 12 h has higher than that of Al-TPA activated for 72 h. Considering the XRD and TGA results activation for 12 h cause formation of different crystal structre and can not effectively remove the impurities from the pores.

5.4. Adsorption Kinetics Studies: Zero Length Column (ZLC)

ZLC experiments are conducted to measure the adsorption kinetics governing the exponential decay, so-called long time asymptote region. ZLC method is an efficient analysis tool allowing to evaluate the existence of external mass transfer resistances and demonstrate whether the processes under kinetic control or eqilibrium control. Altering the temperature and flow rate the experiments can be dictated in different operational regimes, kinetic or equilibrium. The parameters including diffusivity were estimated by simultaneously fitting the experimental data to the developed model stated by Eic and Ruthven (1988). The diffusion of steam methane reformer (SMR) components on Al-TPA having the highest surface area were investigated under different flow rates (80, 168 and 175 mL/min), temperature (34, 70 and 100°C) and sorbate concentration (15% and 28%) via ZLC technique. The high surface area, micropore volume and pore diameter of Al-TPA provides easier penetration and diffusion of gas molecules into the pores. The parameters D_c and L were obtained by using the crystal size (R_c=31.5x10^{-4} cm) and volume (V_s= 5x10^{-3} cm^3). Slope and intercept of the plot of normalized concentration (C/C_0) vs. time yield diffusivity and L parameter using Equation 3.25, which was discussed in detail in the previous Chapter 4. The thermophysical properties of gases were indicated in Table 5.9.

Table 5.9. Thermophysical properties of gases.

Properties	**CO_2**	**CO**	**CH_4**	**H_2**
Boiling Point (°C)	216.55	81.66	11.66	20.27
T_c (K)	304.12	132.85	190.56	32.98
V_c (cm^{3}mol^{-1})	94.07	93.10	98.6	64.20
P_c (bar)	73.74	34.94	45.99	12.93
Kinematic diameter (Å)	3.3	3.690	3.758	2.89
Polarizability (x 10^{25}/cm^3)	29.11	19.5	25.93	8.042
Dipole moment (x 10^{18}/esu.cm)	0	0.10	0	0
Quadrupol moment (x10^{26}/esu.cm^2)	4.3	2.5	0	0.662
Thermal conductivity (W/mK)	0.0146	0.0232	0.035	0.168

Dead volume determination

Dead volume experiments for the blank system was carried out with no adsorbent in the ZLC cell. In Figure 5.33, the response curve for the blank system was fitted on the experimental response curve for CO_2 gas at 168 mL/min flow rates at 100°C.

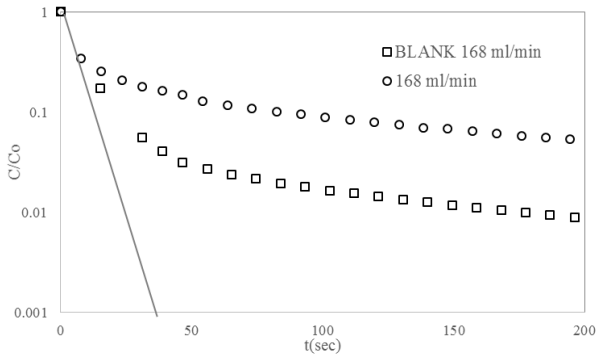

Figure 5.33. Experimental and blank ZLC response curve of CO_2 gas with 168 mL/min at 100°C.

For the blank response, the C/C_0 falls to 0.01 and the response curves are baselined after 30 s which represents the experimental decay over a time range due to the set-up of the ZLC instrument. To obtain reasonable diffusivity excluding the systematic error, the slope of the linear tail should be chosen between the concentrations of 0.1 to 0.01. The dead volume (V_g), the distance between the ZLC cell and MS, of the ZLC system calculated from the slope of the response curve using Equation 3.29 was determined as 14.4 mL (Figure 5.33).

Effect of flow rate of gases on diffusivity

At sufficiently high flow rates the change of concentration over time interval is dominated only by intraparticle diffusion by neglecting the contribution of axial dispersion and effect of external mass transfer resistance. The response curves displayed an initial decline in concentration relate to the fast and sudden purging of the system leading to a slower exponential decay. Long time asymptote region of the response curve is therefore always focused on. It is obvious that the surface resistance has a substantial influence on the tail of the response curve which provides determination of diffusion

coefficient by the long time method, that is increasing surface resistance decreases the slope of the tail (Duncan and Möller 2005).

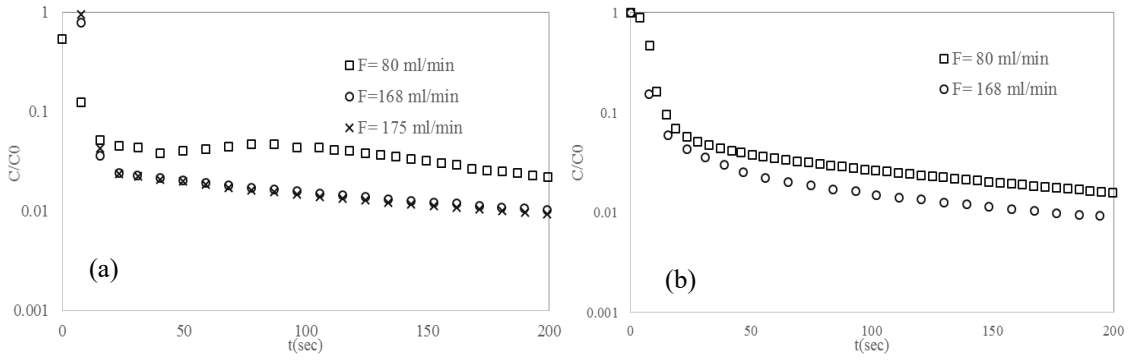

Figure 5.34. Effect of flow rate on the ZLC response curve of a. CH_4 b. CO_2 at 100°C.

Figure 5.34.a represented the response curves of CH_4 gas on Al-TPA at a flow rates of 80, 168 and 175 mL/min at 100°C and Figure 5.34.b showed the effect of flow rate on the response curves of CO_2 gas at 80 and 168 mL/min at 100°C. The effect of external mass transfer can be seen from Figure 5.34.a clearly indicates that the response curves for 80 mL/min diverge whereas the difference between 168 and 175 mL/min is negligible due to overlap of the curves. Therefore, to determine the diffusion coefficient accurately with eliminating the effect of mass transfer resistances the maximum volumetric flow for each gas can be determined as 168 mL/min (Djekic 2007, Hu et al. 2015).

Table 5.10. The effect of flow rate on the kinetic parameters of CH_4 and CO_2 on Al-TPA.

T (°C)	F (mL/min)	L	D/R^2 (s^{-1})	D (m^2/s)	KV_s (mL)	$Kx10^{-3}$
			CH_4			
100	80	32.6	0.00052	5.13×10^{-13}	26.4	5.3
	168	77	0.00052	5.13×10^{-13}	23.5	4.7
	175	80	0.00052	5.13×10^{-13}	23.5	4.7
			CO_2			
100	80	36	0.00081	8.04×10^{-13}	15.2	3.05
	168	55	0.00081	8.04×10^{-13}	21.0	4.19

Diffusion coefficients extracted from the slopes of the response curves should be same at a constant temperature (Liu et al. 2013). The diffusivities are independent of the purge flow rate which can be demonstrated from the Table 5.10. The diffusivity of CH_4 is 5.13 x 10^{-13} m^2/s for each flow rate at 100°C, which corresponds to diffusional time constant value (D/R^2) is 0.00052 s^{-1} (Hoang et al. 2005). The diffusivity of CO_2 at each flowrate was also found to be 8.04 x 10^{-13} m^2/s, proving that the diffusvitiy is independent of the flowrate and the contribution of external resistances were eliminated. The parameter L, the ratio between the diffusional time constant (D/R^2) and the convective desorption time (F/KV_s), represents the extent of the system from equilibrium control. Experiments at different flow rates yielding large and constant L values (L>>1) verified that the system is under kinetically controlled regime. The parameter L is directly proportional to the flow rate and increased with increasing flow rate (Table 5.10) (Guimarães et al. 2010). As the Al-TPA crystals are in the range of micrometers, the dimensionless Henry's law constant can be greater than 10^2-10^3 range. The K value of the measurements, extracted from the intercept of the response curve, at different purge flow rates was approximately 4 x 10^3 as expected.

Effect of adsorbate concentration on diffusivity

Adsorption process was performed with pure helium gas at a flow rate high enough to retain low diluted adsorbate gas concentration of CH_4 with He purge gas while the desorption process was established by pure He purge gas. The effect of the adsorbate gas concentration was determined by evaluating the diffusion of 15% and 28% CH_4 gas with 80 mL/min flow rate on Al-TPA at 100°C (Figure 5.35). Such high concentration values of adsorbate gas can cause nonlinearities in the tail of long time asymptote region, causing the macropore diffusion controlled system and deviation in the diffusivity value (or concentration dependent diffusivity).

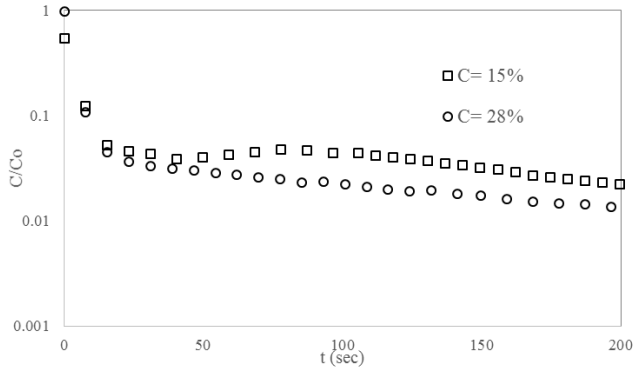

Figure 5.35. Effect of the sorbate gas concentration on the ZLC response curve CH_4 with 80 mL/min flowrate at 100°C.

Table 5.11. Effect of adsorbate gas concentration on the kinetic parameters of CH_4 on Al-TPA.

T (°C)	F (mL/min)	Conc. (%)	L	D/R^2 (s^{-1})	D (m^2/s)	KV_s (mL)	$Kx10^{-3}$
			CH_4				
100	80	15	32.6	0.00052	5.13×10^{-13}	26	5.28
		28	55	0.00052	5.13×10^{-13}	16	3.13

According to the Table 5.11, the diffusivity values for each CH_4 concentration have constant value (5.13×10^{-3} m^2/s), proving that the system is under micropore control even at high concentration ranges. The high values of parameter L can also demonstrated the kinetically controlled system (Friedrich et al. 2015).

Effect of temperature on diffusivity

The effect of temperature (34, 70 and 100°C) of on the response curves of CO_2, CH_4, H_2 and CO gases with 168 mL/min flowrate was illustrated in Figure 5.36. As the temperature increases the tail of the long time asymptote diverges downward.

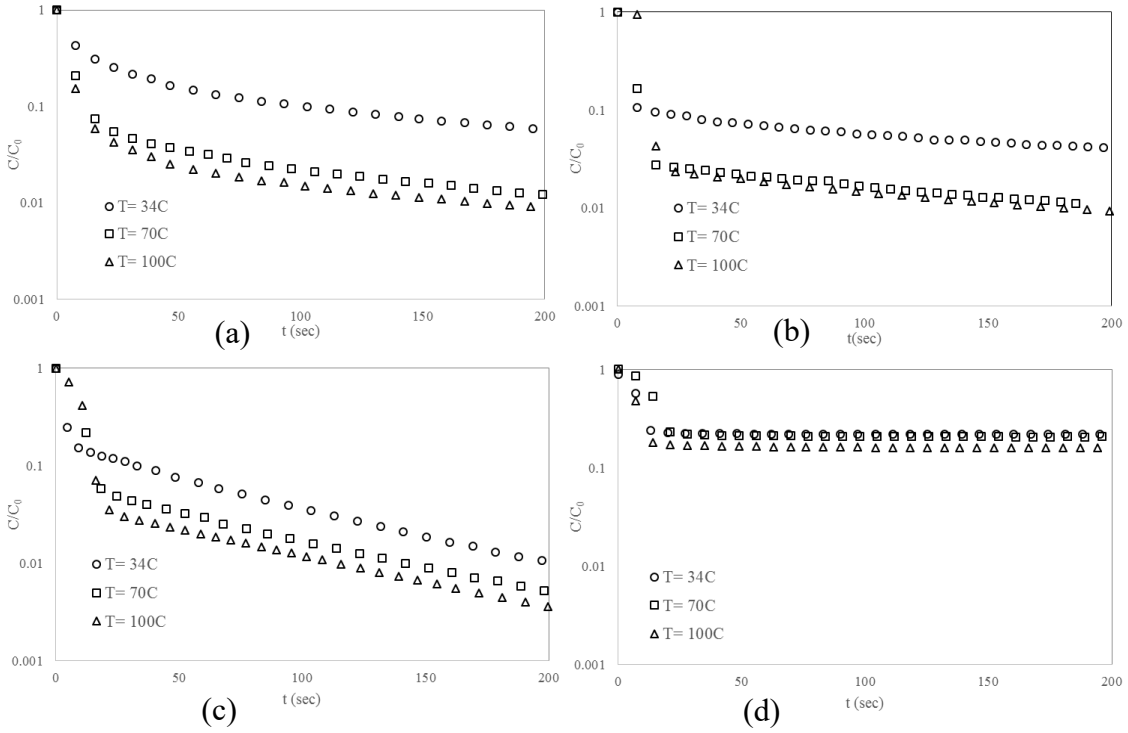

Figure 5.36. The effect of temperature on the ZLC response curves of a) CO_2 b) CH_4 c) H_2 d) CO with 168 mL/min flowrate.

The effect of the temperature on diffusional time constant, diffusivity, Henry's constant, and heat of adsorption were given in Table 5.12. The diffusivity values are strongly dependent on temperature and increases with temperature according to the Table 5.12. H_2 gas has the highest diffusivity of 1.56 x10^{-12} m^2/s and therefore faster and easier penetration and diffusion of H_2 gas in the pores as H_2 gas (2.89 Å) is smaller than other gases in accordance with kinematic diameters given in Table 5.9. High polarizibilty and quadrupole property of CO_2 cause stronger interaction of gases with hydroxyl groups of Al-TPA molecule, leading to slower diffusion as compared to H_2 gas. The diffusivity values of CH_4 and CO_2 gas are in the same order of magnitude as their kinetic diameters and polarizibilty are close.

The long time asymptote region of the response curve is in the Henry law region, that is the Henry's law constant can be extracted with good accuracy (Friedrich et al. 2015). The governing model reduces to an exponential decay in the long-time asymptote possessing the slope or diffusivity inversely proportional to Henry's constant demonstrated the presence of physical adsorption. CO gas has the highest Henry's constant value as CO gas possess dipole moment (0.1 x 10^{18} $esu^{-1}cm^{-1}$) as compared to

other gases. The heat of adsorption of gases calculated using Van't Hoff equation in Equation 3.4. Decreasing of K value with temperature and low values of heat of adsorption demonstrates that heat effects had been eliminated and physical adsorption was occured (Brandani et al. 1998). Heat of adsorption is associated with specific interactions relating with dipole-quadrupole supplemented by polarizability. Having highest dipole-quadrupole CO_2 gas has highest heat of adsorption value was found to be -29.1 kJ/mol. CO gas has close heat of adsorption with CO_2 due to possessing high dipole-quadrupole with polarizability. Having lower dipole-quadrupole and polarizibility as compared to CO_2, H_2 has lower heat of adsorption. Heat of adsorption of methane is lowest since it has no dipole-quadrupole and only polarizability contributes heat of adsorption.

Table 5.12. The effect of temperature on the kinetic parameters of CO_2, CH_4, H_2 and CO on Al-TPA.

T(°C)	F (mL/min)	L	D/R^2 (s^{-1})	D (m^2/s)	KV_s (mL)	$Kx10^{-3}$	ΔH (kJ/mol)	E_a (kJ/mol)
				CH_4				
34		21.7	0.00051	5.03×10^{-13}	40.4	8.09		
70	168	68.4	0.00059	5.83×10^{-13}	23.2	4.64	- 9.71	- 9.37
100		69	0.00067	6.64×10^{-13}	21.1	4.21		
				CO_2				
34		10.8	0.00058	5.73×10^{-13}	149.6	30		
70	168	40	0.00077	7.64×10^{-13}	30.3	6.06	- 29.1	- 5.05
100		55	0.00081	8.04×10^{-13}	21	4.19		
				H_2				
34		14	0.00137	1.36×10^{-12}	48.7	9.75		
70	168	28.7	0.00150	1.49×10^{-12}	21.7	4.34	- 16.7	- 3.07
100		38	0.00157	1.56×10^{-12}	15.6	3.13		
				CO				
34		8.8	0.00001	1.01×10^{-14}	10468	2094		
70	168	9	0.00004	4.02×10^{-14}	2559	511	- 28.2	- 29.8
100		12	0.00005	5.03×10^{-14}	1535	307		

Activation energies of gases, or namely energy barrier must be exceeded to intracrystalline diffusion, were extracted using Arrhenius equation in Equation 3.14 demonstrated that CO and CH_4 gases have highest activation energy strongly associated with their high kinematic diameter. Herein, possessing highest activation energy CO was more affected by surface characteristics of porous Al-TPA adsorbent. H_2 has the lowest activation energy due to being smallest gas among the components of SMR off-gases.

CHAPTER 6

CONCLUSION

This thesis was successfully accomplished within the scope of the TUBITAK (112M294) project executed in IYTE and Ege University. The aim of this thesis mainly was to synthesize aluminum based metal-organic frameworks (Al-TPA) and study diffusion behaviour of SMR off-gas components on Al-TPA via ZLC technique.

The synthesis of aluminum terephthalate was conducted by following hydrothermal, solvothermal and hydro-solvothermal synthesis route in three main step, crystallization, purification and activation. In hydrothermal synthesis, the reaction of water and $Al(NO_3)_3.9H_2O$ generate boehmite possessing very low surface area instead of Al-TPA MOF structure. Considering the time and energy consumption washing only with water instead of solvents sufficient for the removal of impurities in the cavities. Activation temperature higher than 400°C changed the structure of Al-TPA into different alumina phase. On the other hand, addition of precrystalization step altered the structure BDC organic linker and produced CAU-13 aluminum based MOF structure.

Solvothermal synthesis route yielded efficient Al-TPA MOF structure whose surface areas are extemely high and characterization results corresponded to Al-TPA low temperature structure reported by Louiseau et al. 2004. To lower the usage of DMF solvent purification step was performed washing with only methanol instead of DMF enhanced the BET surface area from 1051 to 1270 m^2/g. Regarding the environmental and energy concerns the optimized conditions for solvothermal synthesis were maintained by crystallization and activation at lower temperature (130°C) and purification with only methanol. Aluminum terephthalate synthesized by given conditions was then placed in the ZLC column for further diffusion studies.

In hydro-solvothermal synthesis method, surface areas of Al-TPA was slightly lower than that of Al-TPA synthesized by solvothermal method. Regardless of crystallization temperature, increasing the crystallization time or decreasing activation time and temperature enhances BET surface area. The highest surface area of Al-TPA crystallized at 150°C for 72 hours and activated at 130°C for 72 hours was found to be

902 m^2/g. For crystallization at 130°C, the highest surface area of Al-TPA was lowered to 717 m^2/g as compared with crystallization at 150°C.

The effect of gas flow rate (80, 168 and 175 mL/min), temperature (34, 70 and 100°C) and sorbate concentration (15% and 28%) on the diffusion behaviour of SMR off-gas components were investigated using ZLC technique by examining the long time asympote region of response curves derived from desorption process. Dead volume between the ZLC cell and mass spectrometer was determined as 14.4 ml causing experimental decay. Measurements represented the parameter L higher than 1 proved that desorption process had been maintained under kinetic control instead of equilibrium control. Diffusivity values of CH_4 and CO_2 at different purge flow rates remained constant respectively as 5.13×10^{-13} and 8.04×10^{-13} m^2/s, proving that the effect of external resistances to mass transfer was eliminated. Having constant diffusivity value (5.13×10^{-13} m^2/s) for each CH_4 concentration demonstrated that the system proceeded under micropore control instead of macropore diffusion. In accordance with kinematic diameter, the order of diffusivity values were found to be ranging from 1.36×10^{-12}-1.56×10^{-12} for H_2, 5.73×10^{-13}-8.04×10^{-13} for CO_2, 5.03×10^{-13}-6.64×10^{-13} for CH_4, and 1.01×10^{-13}-5.03×10^{-13} m^2/g for CO respectively with increasing temperature. Activation energy, associated strongly with kinematic diameter and diffusivity, for CO, CH_4, CO_2 and H_2 gases were determined as -29.8, -9.37, -5.05 and -3.07 kJ/mol. CO gas was more affected by surface characteristics of porous adsorbent due to possessing highest activation energy. Possessing highest dipole-quadrupole and polarizability CO_2 gas has the highest heat of adsorption value of - 29.1 kJ/mol. Decreasing of Henry's constant of gases with temperature and low values of heat of adsorption demonstrated that the process is reversible.

.

REFERENCES

Ahn, W.-S., Kim, J. and Kim, W. Y. 2012. "Amine-functionalized MIL-53(Al) for CO2/N2 separation: Effect of textural properties" *Fuel* 102:574-579. doi:http://dx.doi.org/10.1016/j.fuel.2012.06.016.

Arstad, B., Fjellvåg, H., Kongshaug, K. O., Swang, O. and Blom, R. 2008. "Amine functionalised metal organic frameworks (MOFs) as adsorbents for carbon dioxide" *Adsorption* 14:755-762. doi:http://dx.doi.org/10.1007/s10450-008-9137-6.

Baiker, A., Jiang, Y., Huang, J., Marx, S., Kleist, W. and Hunger, M. 2010. "Effect of dehydration on the local structure of framework aluminum atoms in mixed linker MIL-53(Al) materials studied by solid-state NMR spectroscopy" *The Journal of Physical Chemistry Letters* 1:2886-2890. doi:http://dx.doi.org/10.1021/jz1010835.

Bajaj, H. C., Rallapalli, P., Patil, D., Prasanth, K. P., Somani, R. S. and Jasra, R. V. 2010. "An alternative activation method for the enhancement of methane storage capacity of nanoporous aluminium terephthalate, MIL-53(Al)" *Journal of Porous Materials* 17:523-528. doi:10.1007/s10934-009-9320-5.

Boulicaut, L., Brandani, S. and Ruthven, D. M. 1998. "Liquid phase sorption and diffusion of branched and cyclic hydrocarbons in silicalite" *Microporous and Mesoporous Materials* 25:81-93. doi:https://doi.org/10.1016/S1387-1811(98)00175-9.

Brandani, F. 2002. "Development and application of the Zero Length Column (ZLC) technique for measuring adsorption equilibria" Doctoral Thesis, Chemical Engineering, The University of Maine.

Brandani, S. 1996. "Analytical solution for ZLC desorption curves with bi-porous adsorbent particles" *Chemical Engineering Science* 51:3283-3288. doi:http://dx.doi.org/10.1016/0009-2509(95)00399-1.

Brandani, S., Cavalcante, C., Guimarães, A. and Ruthven, D. 1998. "Heat effects in ZLC experiments" *Adsorption* 4:275-285. doi:http://dx.doi.org/10.1023/a:1008837801299.

Brandani, S., Hufton, J. and Ruthven, D. 1995. "Self-diffusion of propane and propylene in 5A and 13X zeolite crystals studied by the tracer ZLC method" *Zeolites* 15:624-631. doi:http://dx.doi.org/10.1016/0144-2449(95)00042-5.

Brandani, S., Jama, M. and Ruthven, D. 2000. "Diffusion, self-diffusion and counter-diffusion of benzene and p-xylene in silicalite" *Microporous and Mesoporous Materials* 35–36:283-300. doi:https://doi.org/10.1016/S1387-1811(99)00228-0.

Brandani, S., Jama, M. and Ruthven, D. M. 2000. "Counterdiffusion of p-Xylene/Benzene and p-Xylene/o-Xylene in silicalite studied by the Zero-Length Column technique" *Industrial & Engineering Chemistry Research* 39:821-828. doi:http://dx.doi.org/10.1021/ie990691b.

Brandani, S., Jama, M. A. and Ruthven, D. M. 2000. "ZLC Measurements under non-linear conditions" *Chemical Engineering Science* 55:1205-1212. doi:http://dx.doi.org/10.1016/S0009-2509(99)00411-X.

Brandani, S. and Ruthven, D. M. 1995. "Analysis of ZLC desorption curves for liquid systems" *Chemical Engineering Science* 50:2055-2059. doi:http://dx.doi.org/10.1016/0009-2509(95)00048-A.

Bu, X.-H., Tian, D., Zhou, X.-L., Zhang, Y.-H. and Zhou, Z. 2015. "MOF-derived porous Co3O4 hollow tetrahedra with excellent performance as anode materials for lithium-ion batteries" *Inorganic Chemistry* 54:8159-8161. doi:http://dx.doi.org/10.1021/acs.inorgchem.5b00544.

Calleja, G., Martínez, F., Orcajo, G., Briones, D. and Leo, P. 2017. "Catalytic advantages of NH2-modified MIL-53(Al) materials for Knoevenagel condensation reaction" *Microporous and Mesoporous Materials* 246:43-50. doi:https://doi.org/10.1016/j.micromeso.2017.03.011.

Chen, W.-H., Yang, S.-P., Chen, S.-R., Liu, S.-W., Tang, X.-Y., Qin, L., Qiu, G.-H. and Chen, J.-X. 2015. "Platforms formed from a three-dimensional Cu-based zwitterionic metal–organic framework and probe ss-DNA: selective fluorescent biosensors for human immunodeficiency virus 1 ds-DNA and sudan virus RNA sequences" *Analytical Chemistry* 87:12206-12214. doi:http://dx.doi.org/10.1021/acs.analchem.5b03084.

Corma, A., Luz, I. and Llabrés i Xamena, F. X. 2012. "Bridging homogeneous and heterogeneous catalysis with MOFs: Cu-MOFs as solid catalysts for three-component coupling and cyclization reactions for the synthesis of propargylamines, indoles and imidazopyridines" *Journal of Catalysis* 285:285-291. doi:https://doi.org/10.1016/j.jcat.2011.10.001.

Damirin, A., Gao, X., Zhai, M., Guan, W., Liu, J. and Liu, Z. 2017. "Controllable synthesis of a smart multifunctional nanoscale metal–organic framework for magnetic resonance/optical imaging and targeted drug delivery" *ACS Applied Materials & Interfaces* 9:3455-3462. doi:http://dx.doi.org/10.1021/acsami.6b14795.

Della Rocca, J., Liu, D. and Lin, W. 2011. "Nanoscale metal–organic frameworks for biomedical imaging and drug delivery" *Accounts of Chemical Research* 44:957-968. doi:http://dx.doi.org/10.1021/ar200028a.

Denayer, J. F. M., Couck, S., Baron, G. V., Rémy, T., Gascon, J. and Kapteijn, F. 2009. "An Amine-functionalized MIL-53 metal−organic framework with large

separation power for CO2 and CH4" *Journal of the American Chemical Society* 131:6326-6327. doi:http://dx.doi.org/10.1021/ja900555r.

Dias, E. M. and Petit, C. 2015. "Towards the use of metal-organic frameworks for water reuse: a review of the recent advances in the field of organic pollutants removal and degradation and the next steps in the field" *Journal of Materials Chemistry A* 3:22484-22506. doi:http://dx.doi.org/10.1039/C5TA05440K.

Dincă, M., Campbell, M. G., Liu, S. F. and Swager, T. M. 2015. "Chemiresistive sensor arrays from conductive 2D metal–organic frameworks" *Journal of the American Chemical Society* 137:13780-13783. doi:http://dx.doi.org/10.1021/jacs.5b09600.

Djekic, T. 2007. "Effective intraparticle diffusion coefficients of CoCl2 in mesoporous functionalized silica adsorbents" *Adsorption* 13:231-237. doi:http://dx.doi.org/10.1007/s10450-007-9070-0.

Do, D. D. 1998. *Adsorption Analysis: Equilibria and Kinetics*: Imperial College Press.

Drioli, E. and Barbieri, G. 2011. *Membrane Engineering for the Treatment of Gases*: RSC Publishing.

Duncan, W. L. and Möller, K. P. 2000. "A 'zero length' criterion for ZLC chromatography" *Chemical Engineering Science* 55:5415-5420. doi:http://dx.doi.org/10.1016/S0009-2509(00)00160-3.

Duncan, W. L. and Möller, K. P. 2002. "The effect of a crystal size distribution on ZLC experiments" *Chemical Engineering Science* 57:2641-2652. doi:http://dx.doi.org/10.1016/S0009-2509(02)00161-6.

Duncan, W. L. and Möller, K. P. 2005. "Diffusion in surface modified ZSM-5 studied using the ZLC method" *Adsorption* 11:259-273. doi:http://dx.doi.org/10.1007/s10450-005-5399-4.

Eić, M., Micke, A., Kočirík, M., Jama, M. and Zikánová, A. 2002. "Diffusion and Immobilization Mechanisms in Zeolites Studied by ZLC Chromatography" *Adsorption* 8:15-22. doi:http://dx.doi.org/10.1023/a:1015262222109.

Eic, M. and Ruthven, D. M. 1988. "Diffusion of linear paraffins and cyclohexane in NaX and 5A zeolite crystals" *Zeolites* 8:472-479. doi:http://dx.doi.org/10.1016/S0144-2449(88)80223-9.

Eubank, J. F. 2008. "Rational synthesis toward the design of functional metal-organic materials" Doctoral Thesis, Chemistry, University of South Florida.

Farha, O. K., Eryazici, I., Jeong, N. C., Hauser, B. G., Wilmer, C. E., Sarjeant, A. A., Snurr, R. Q., Nguyen, S. T., Yazaydın, A. Ö. and Hupp, J. T. 2012. "Metal–organic framework materials with ultrahigh surface areas: Is the sky the limit?" *Journal of the American Chemical Society* 134:15016-15021. doi:http://dx.doi.org/10.1021/ja3055639.

Ferey, G., Latroche, M., Serre, C., Millange, F., Loiseau, T. and Percheron-Guegan, A. 2003. "Hydrogen adsorption in the nanoporous metal-benzenedicarboxylate M(OH)(O2C-C6H4-CO2) (M = Al3+, Cr3+), MIL-53" *Chemical Communications* 2976-2977. doi:http://dx.doi.org/10.1039/B308903G.

Ferreira, A. F. P., Ribeiro, A. M., Kulaç, S. and Rodrigues, A. E. 2015. "Methane purification by adsorptive processes on MIL-53(Al)" *Chemical Engineering Science* 124:79-95. doi:https://doi.org/10.1016/j.ces.2014.06.014.

Friedrich, D., Mangano, E. and Brandani, S. 2015. "Automatic estimation of kinetic and isotherm parameters from ZLC experiments" *Chemical Engineering Science* 126:616-624. doi:http://dx.doi.org/10.1016/j.ces.2014.12.062.

Gibson, J. A. A., Mangano, E., Shiko, E., Greenaway, A. G., Gromov, A. V., Lozinska, M. M., Friedrich, D., Campbell, E. E. B., Wright, P. A. and Brandani, S. 2016. "Adsorption materials and processes for carbon capture from gas-fired power plants: AMPGas" *Industrial & Engineering Chemistry Research* 55:3840-3851. doi:http://dx.doi.org/10.1021/acs.iecr.5b05015.

Guimarães, A. P., Möller, A., Staudt, R., de Azevedo, D. C. S., Lucena, S. M. P. and Cavalcante, C. L. 2010. "Diffusion of linear paraffins in silicalite studied by the ZLC method in the presence of CO2" *Adsorption* 16:29-36. doi:http://dx.doi.org/10.1007/s10450-010-9205-6.

Gumma, S., Mishra, P., Edubilli, S., Uppara, H. P. and Mandal, B. 2013. "Effect of adsorbent history on adsorption characteristics of MIL-53(Al) metal organic framework" *Langmuir* 29:12162-12167. doi: http://dx.doi.org/10.1021/la4027128.

Gunadi, A. and Brandani, S. 2006. "Diffusion of linear paraffins in NaCaA studied by the ZLC method" *Microporous and Mesoporous Materials* 90:278-283. doi:https://doi.org/10.1016/j.micromeso.2005.11.027.

Hadjiivanov, K., Mihaylov, M., Chakarova, K., Andonova, S., Drenchev, N., Ivanova, E., Pidko, E. A., Sabetghadam, A., Seoane, B., Gascon, J. and Kapteijn, F. 2016. "Adsorption of CO2 on MIL-53(Al): FTIR evidence of the formation of dimeric CO2 species" *Chemical Communications* 52:1494-1497. doi:http://dx.doi.org/10.1039/C5CC08677A.

Hartmann, M., Himsl, D. and Wallacher, D. 2009. "Improving the hydrogen-Adsorption properties of a hydroxy-modified MIL-53(Al) structural analogue by lithium doping" *Angewandte Chemie International Edition* 48:4639-4642. doi:http://dx.doi.org/10.1002/anie.200806203.

Hirscher, M. and Panella, B. 2005. "Hydrogen physisorption in metal–organic porous crystals" *Advanced Materials* 17:538-541. doi:http://dx.doi.org/10.1002/adma.200400946.

Hirscher, M. and Panella, B. 2005. "Nanostructures with high surface area for hydrogen storage" *Journal of Alloys and Compounds* 404:399-401. doi:http://dx.doi.org/10.1016/j.jallcom.2004.11.109.

Hirscher, M., Panella, B. and Schmitz, B. 2010. "Metal-organic frameworks for hydrogen storage" *Microporous and Mesoporous Materials* 129:335-339. doi:http://dx.doi.org/10.1016/j.micromeso.2009.06.005.

Hoang, V.-T., Huang, Q., Eić, M., Do, T.-O. and Kaliaguine, S. 2005. "Structure and diffusion characterization of SBA-15 materials" *Langmuir* 21:2051-2057. doi:http://dx.doi.org/10.1021/la048349d.

Hu, X., Brandani, S., Benin, A. I. and Willis, R. R. 2015. "Development of a semiautomated Zero Length Column technique for carbon capture applications: Rapid capacity ranking of novel adsorbents" *Industrial & Engineering Chemistry Research* 54:6772-6780. doi:http://dx.doi.org/10.1021/acs.iecr.5b00513.

Hu, X., Brandani, S., Benin, A. I. and Willis, R. R. 2015. "Development of a semiautomated Zero Length Column technique for carbon capture applications: Study of diffusion behavior of CO2 in MOFs" *Industrial & Engineering Chemistry Research* 54:5777-5783. doi:http://dx.doi.org/10.1021/acs.iecr.5b00515.

Hu, X., Mangano, E., Friedrich, D., Ahn, H. and Brandani, S. 2014. "Diffusion mechanism of CO2 in 13X zeolite beads" *Adsorption* 20:121-135. doi:http://dx.doi.org/10.1007/s10450-013-9554-z.

Huang, Y., Qian, X., Yadian, B., Wu, R., Long, Y., Zhou, K. and Zhu, B. 2013. "Structure stability of metal-organic framework MIL-53 (Al) in aqueous solutions" *International Journal of Hydrogen Energy* 38:16710-16715. doi:http://dx.doi.org/10.1016/j.ijhydene.2013.07.054.

Hufton, J. R., Brandani, S. and Ruthven, D. M. 1994. "Measurement of intracrystalline diffusion by Zero Length Column tracer exchange" *Studies in Surface Science and Catalysis* 84:1323-1330. doi:http://dx.doi.org/10.1016/S0167-2991(08)63674-5.

Hufton, J. R. and Ruthven, D. M. 1993. "Diffusion of light alkanes in silicalite studied by the zero length column method" *Industrial & Engineering Chemistry Research* 32:2379-2386. doi:10.1021/ie00022a022.

Jhung, S. H., Bhadra, B. N., Cho, K. H., Khan, N. A. and Hong, D.-Y. 2015. "Liquid-phase adsorption of aromatics over a Metal–organic framework and activated carbon: Effects of hydrophobicity/hydrophilicity of adsorbents and solvent polarity" *The Journal of Physical Chemistry C* 119:26620-26627. doi:http://dx.doi.org/10.1021/acs.jpcc.5b09298.

Jiang, J. 2009. "Charged soc metal-organic framework for high-efficacy H2 adsorption and syngas purification: Atomistic simulation study" *AIChE Journal* 55:2422-2432. doi:http://dx.doi.org/10.1002/aic.11865.

Kaliaguine, S., Do, X.-D. and Hoang, V.-T. 2011. "MIL-53(Al) mesostructured metal-organic frameworks" *Microporous and Mesoporous Materials* 141:135-139. doi:https://doi.org/10.1016/j.micromeso.2010.07.024.

Karge, H. G. and Weitkamp, J. 2008. *Molecular Sieves Adsorption and Diffusion*: Springer Netherlands.

Karger, J. and Ruthven, D. M. 1992. *Diffusion in Zeolites and Other Microporous Solids*: Wiley.

Kärger, J., Ruthven, D. M. and Theodorou, D. N. 2012. *Diffusion in Nanoporous Materials*: Wiley.

Keller, J. and Staudt, R. 2005. *Gas adsorption equilibria experimental methods and adsorption isotherms*: Springer Netherlands.

Lee, C. 2003. *Adsorption Science and Technology*: World Scientific Publishing Company.

Li, J., Rudd, N. D., Wang, H., Fuentes-Fernandez, E. M. A., Teat, S. J., Chen, F., Hall, G. and Chabal, Y. J. 2016. "Highly efficient luminescent metal–organic framework for the simultaneous detection and removal of heavy metals from water" *ACS Applied Materials & Interfaces* 8:30294-30303. doi:http://dx.doi.org/10.1021/acsami.6b10890.

Li, Z., Wu, Y.-n., Li, J., Zhang, Y., Zou, X. and Li, F. 2015. "The metal–organic framework MIL-53(Al) constructed from multiple metal sources: Alumina, aluminum hydroxide, and boehmite" *Chemistry – A European Journal* 21:6913-6920. doi:http://dx.doi.org/10.1002/chem.201406531.

Liu, C., Wu, Y.-n., Morlay, C., Gu, Y., Gebremariam, B., Yuan, X. and Li, F. 2016. "General deposition of metal–organic frameworks on highly adaptive organic–inorganic hybrid electrospun fibrous substrates" *ACS Applied Materials & Interfaces* 8:2552-2561. doi:http://dx.doi.org/10.1021/acsami.5b10078.

Liu, Y., Her, J.-H., Dailly, A., Ramirez-Cuesta, A. J., Neumann, D. A. and Brown, C. M. 2008. "Reversible structural transition in MIL-53 with large temperature hysteresis" *Journal of the American Chemical Society* 130:11813-11818. doi:http://dx.doi.org/10.1021/ja803669w.

Liu, Z., Fan, W., Xue, Z., Ma, J. and Li, R. 2013. "Diffusion of n-alkanes in mesoporous 5A zeolites by ZLC method" *Adsorption* 19:201-208. doi:http://dx.doi.org/10.1007/s10450-012-9441-z.

Loiseau, T., Serre, C., Huguenard, C., Fink, G., Taulelle, F., Henry, M., Bataille, T. and Férey, G. 2004. "A Rationale for the large breathing of the porous aluminum terephthalate (MIL-53) upon hydration" *Chemistry – A European Journal* 10:1373-1382. doi:http://dx.doi.org/10.1002/chem.200305413.

Long, J. R., Levine, D. J., Runčevski, T., Kapelewski, M. T., Keitz, B. K., Oktawiec, J., Reed, D. A., Mason, J. A., Jiang, H. Z. H., Colwell, K. A., Legendre, C. M. and FitzGerald, S. A. 2016. "Olsalazine-based metal–organic frameworks as biocompatible platforms for H2 adsorption and drug delivery" *Journal of the American Chemical Society* 138:10143-10150. doi:http://dx.doi.org/10.1021/jacs.6b03523.

Long, J. R., Murray, L. J. and Dinca, M. 2009. "Hydrogen storage in metal-organic frameworks" *Chemical Society Reviews* 38:1294-1314. doi:http://dx.doi.org/10.1039/B802256A.

Loos, J.-B. W. P., Verheijen, P. J. T. and Moulijn, J. A. 2000. "Improved estimation of zeolite diffusion coefficients from zero–length column experiments" *Chemical Engineering Science* 55:51-65. doi:http://dx.doi.org/10.1016/S0009-2509(99)00189-X.

Madan, R. L. 1999. *Physical chemistry*: McGraw-Hill Education.

Mandal, B., Mishra, P., Uppara, H. P. and Gumma, S. 2014. "Adsorption and separation of carbon dioxide using MIL-53(Al) metal-organic framework" *Industrial & Engineering Chemistry Research* 53:19747-19753. doi:http://dx.doi.org/10.1021/ie5006146.

Mangano, E., Brandani, S. and Ruthven, D. M. 2013. "Analysis and interpretation of Zero Length Column response curves" *Chemie Ingenieur Technik* 85:1714-1718. doi:http://dx.doi.org/10.1002/cite.201300083.

Manos, M. J., Kumar, P., Pournara, A., Kim, K.-H., Bansal, V. and Rapti, S. 2017. "Metal-organic frameworks: Challenges and opportunities for ion-exchange/sorption applications" *Progress in Materials Science* 86:25-74. doi:https://doi.org/10.1016/j.pmatsci.2017.01.002.

Miao, Z., Qi, C., Wang, L., Wensley, A. M. and Luan, Y. 2017. "The synthesis of metal–organic framework Al-MIL-53-derived Brønsted acid catalyst and its application in the Mannich reaction" *Applied Organometallic Chemistry* 31:e3569-n/a. doi:http://dx.doi.org/10.1002/aoc.3569.

Miljanić, O. Š., Chen, T.-H., Popov, I. and Kaveevivitchai, W. 2014. "Metal–organic frameworks: Rise of the ligands" *Chemistry of Materials* 26:4322-4325. doi:http://dx.doi.org/10.1021/cm501657d.

Monge, M. Á., Aguirre-Díaz, L. M., Reinares-Fisac, D., Iglesias, M., Gutiérrez-Puebla, E., Gándara, F. and Snejko, N. 2017. "Group 13th metal-organic frameworks and

their role in heterogeneous catalysis" *Coordination Chemistry Reviews* 335:1-27. doi:https://doi.org/10.1016/j.ccr.2016.12.003.

Moulijn, J. A., Makkee, M. and Diepen, A. E. 2013. *Chemical Process Technology*: Wiley.

Möller, A., Pessoa Guimaraes, A., Gläser, R. and Staudt, R. 2009. "Uptake-curves for the determination of diffusion coefficients and sorption equilibria for n-alkanes on zeolites" *Microporous and Mesoporous Materials* 125:23-29. doi:https://doi.org/10.1016/j.micromeso.2009.04.029.

Nadeem, M. A., Khan, I. A., Qian, Y., Badshah, A. and Zhao, D. 2016. "Highly porous carbon derived from MOF-5 as a support of ORR electrocatalysts for fuel cells" *ACS Applied Materials & Interfaces* 8:17268-17275. doi:http://dx.doi.org/10.1021/acsami.6b04548.

Pearce, G. M. 2009. "Synthesis, adsorption and catalysis of large pore metal phosphonates" Doctoral Thesis, Chemistry, University of St Andrews.

Pham, M. 2013. "Nanoscale metal-organic frameworks: Synthesis and application of bimodal micro/meso-structure and nanocrystals with controlled size and shape" Doctoral Thesis, Chemical Engineering, University Laval.

Reinsch, H. and Stock, N. 2013. "High-throughput studies of highly porous Al-based MOFs" *Microporous and Mesoporous Materials* 171:156-165. doi:http://dx.doi.org/10.1016/j.micromeso.2012.12.024.

Rodrigue, D., Chen, X. Y., Vinh-Thang, H. and Kaliaguine, S. 2012. "Amine-functionalized MIL-53 metal–organic framework in polyimide mixed matrix membranes for CO2/CH4 separation" *Industrial & Engineering Chemistry Research* 51:6895-6906. doi: http://dx.doi.org/10.1021/ie3004336.

Rodrigues, A. E., LeVan, M. D. and Tondeur, D. 1989. *Adsorption: Science and Technology*: Springer Netherlands.

Rodríguez, J. F., Valverde, J. L. and Rodrigues, A. E. 1998. "Measurements of effective self-diffusion coefficients in a gel-type cation exchanger by the Zero-Length-Column method" *Industrial & Engineering Chemistry Research* 37:2020-2028. doi:http://dx.doi.org/10.1021/ie970684s.

Rosi, N. L., Eckert, J., Eddaoudi, M., Vodak, D. T., Kim, J., O'Keeffe, M. and Yaghi, O. M. 2003. "Hydrogen storage in microporous metal-organic frameworks" *Science* 300:1127-1129. doi:http://dx.doi.org/10.1126/science.1083440.

Ruthven, D. and Brandani, F. 2005. "ZLC response for systems with surface resistance control" *Adsorption* 11:31-34. doi:http://dx.doi.org/10.1007/s10450-005-1090-z.

Ruthven, D., Brandani, F. and Coe, C. G. 2003. "Measurement of adsorption equilibrium by the Zero Length Column (ZLC) technique part 1: Single-component systems"

Industrial & Engineering Chemistry Research 42:1451-1461. doi:http://dx.doi.org/10.1021/ie020572n.

Ruthven, D. M. 1984. *Principles of adsorption and adsorption processes*: Wiley.

Ruthven, D. M. 2001. Diffusion in zeolite molecular sieves. In H. Bekkum, E. M. Flanigen, P. A. Jacobs and J. M. Jansen (Eds.) *Studies in surface science and catalysis* 525-577.

Ruthven, D. M. 2006. *Transport in microporous solids: An historical perspective part I: Fundamental principles and sorption kinetics*: Springer Netherlands.

Ruthven, D. M. and Brandani, S. 2000. Measurement of diffusion in porous solids by Zero Length Column (ZLC) methods. In N. K. Kanellopoulos (Eds.) *Recent Advances in Gas Separation by Microporous Ceramic Membranes* 187-212.

Ruthven, D. M. and Stapleton, P. 1993. "Measurement of liquid phase counter-diffusion in zeolite crystals by the ZLC method" *Chemical Engineering Science* 48:89-98. doi:http://dx.doi.org/10.1016/0009-2509(93)80285-X.

Ruthven, D. M. and Vidoni, A. 2012. "ZLC diffusion measurements: Combined effect of surface resistance and internal diffusion" *Chemical Engineering Science* 71:1-4. doi:http://dx.doi.org/10.1016/j.ces.2011.11.040.

Saha, D. and Deng, S. 2010. "Ammonia adsorption and its effects on framework stability of MOF-5 and MOF-177" *Journal of Colloid and Interface Science* 348:615-620. doi:http://dx.doi.org/10.1016/j.jcis.2010.04.078.

Saha, D., Wei, Z. and Deng, S. 2008. "Equilibrium, kinetics and enthalpy of hydrogen adsorption in MOF-177" *International Journal of Hydrogen Energy* 33:7479-7488. doi:http://dx.doi.org/10.1016/j.ijhydene.2008.09.053.

Saha, D., Zacharia, R., Lafi, L., Cossement, D. and Chahine, R. 2012. "Synthesis, characterization and hydrogen adsorption properties of metal–organic framework Al-TCBPB" *International Journal of Hydrogen Energy* 37:5100-5107. doi:http://dx.doi.org/10.1016/j.ijhydene.2011.12.072.

Sayılgan, Ş. Ç. 2013. "Determination of characteristics of adsorbent for adsorption heat pumps" Master's Thesis, Chemical Engineering, Izmir Instute of Technology.

Schneemann, A., Bon, V., Schwedler, I., Senkovska, I., Kaskel, S. and Fischer, R. A. 2014. "Flexible metal-organic frameworks" *Chemical Society Reviews* 43:6062-6096. doi:http://dx.doi.org/10.1039/C4CS00101J.

Schuring, D. 2002. "Diffusion in zeolites : towards a microscopic understanding" Doctoral Thesis, Chemical Engineering, Technische Universiteit Eindhoven.

Serre, C., Horcajada, P., Maurin, G., Ramsahye, N. A., Balas, F., Vallet-Regí, M., Sebban, M., Taulelle, F. and Férey, G. 2008. "Flexible porous metal-organic

frameworks for a controlled drug delivery" *Journal of the American Chemical Society* 130:6774-6780. doi:http://dx.doi.org/10.1021/ja710973k.

Shadid, S. 2015. "Polymer-metal organic frameworks (MOFs) mixed matrix membranes for gas separation applications" Doctoral Thesis, Membrane Engineering, University of Twente.

Shah, D. B., Hayhurst, D. T., Evanina, G. and Guo, C. J. 1988. "Sorption and diffusion of benzene in HZSM-5 and silicalite crystals" *AIChE Journal* 34:1713-1717. doi:http://dx.doi.org/10.1002/aic.690341016.

Silva, J. A. C., Schumann, K. and Rodrigues, A. E. 2012. "Sorption and kinetics of CO2 and CH4 in binderless beads of 13X zeolite" *Microporous and Mesoporous Materials* 158:219-228. doi:https://doi.org/10.1016/j.micromeso.2012.03.042.

Somani, R. S., Patil, D. V., Rallapalli, P. B. S., Dangi, G. P., Tayade, R. J. and Bajaj, H. C. 2011. "MIL-53(Al): An efficient adsorbent for the removal of nitrobenzene from aqueous solutions" *Industrial & Engineering Chemistry Research* 50:10516-10524. doi:http://dx.doi.org/10.1021/ie200429f.

Stoddart, J. F., Hartlieb, K. J., Ferris, D. P., Holcroft, J. M., Kandela, I., Stern, C. L., Nassar, M. S. and Botros, Y. Y. 2017. "Encapsulation of Ibuprofen in CD-MOF and related bioavailability studies" *Molecular Pharmaceutics* 14:1831-1839. doi:http://dx.doi.org/10.1021/acs.molpharmaceut.7b00168.

Timofeeva, M. N., Panchenko, V. N., Khan, N. A., Hasan, Z., Prosvirin, I. P., Tsybulya, S. V. and Jhung, S. H. 2017. "Isostructural metal-carboxylates MIL-100(M) and MIL-53(M) (M: V, Al, Fe and Cr) as catalysts for condensation of glycerol with acetone" *Applied Catalysis A: General* 529:167-174. doi:https://doi.org/10.1016/j.apcata.2016.11.006.

Trens, P., Trung, T. K., Tanchoux, N., Bourrelly, S., Llewellyn, P. L., Loera-Serna, S., Serre, C., Loiseau, T., Fajula, F. and Férey, G. 2008. "Hydrocarbon adsorption in the flexible metal organic frameworks MIL-53(Al, Cr)" *Journal of the American Chemical Society* 130:16926-16932. doi:http://dx.doi.org/10.1021/ja8039579.

Truong, T., Nguyen, H. T. T. and Doan, D. N. A. 2017. "Unprecedented salt-promoted direct arylation of acidic sp2 CH bonds under heterogeneous Ni-MOF-74 catalysis: Synthesis of bioactive azole derivatives" *Journal of Molecular Catalysis A: Chemical* 426, Part A:141-149. doi:https://doi.org/10.1016/j.molcata.2016.11.009.

Verpoort, F., Chughtai, A. H., Ahmad, N., Younus, H. A. and Laypkov, A. 2015. "Metal-organic frameworks: versatile heterogeneous catalysts for efficient catalytic organic transformations" *Chemical Society Reviews* 44:6804-6849. doi:10.1039/C4CS00395K.

Vidoni, A. and Ruthven, D. M. 2012. "Diffusion of C2H6 and C2H4 in DDR zeolite" *Industrial & Engineering Chemistry Research* 51:1383-1390. doi:http://dx.doi.org/10.1021/ie202449q.

Wang, B., Han, Y., Qi, P., Feng, X., Li, S., Fu, X., Li, H., Chen, Y., Zhou, J. and Li, X. 2015. "In situ growth of MOFs on the surface of Si nanoparticles for highly efficient lithium storage: Si@MOF nanocomposites as anode materials for lithium-ion batteries" *ACS Applied Materials & Interfaces* 7:2178-2182. doi:http://dx.doi.org/10.1021/am5081937.

Wang, B., Wang, L., Feng, X., Ren, L., Piao, Q., Zhong, J., Wang, Y., Li, H. and Chen, Y. 2015. "Flexible solid-state supercapacitor based on a metal–organic framework interwoven by electrochemically-deposited PANI" *Journal of the American Chemical Society* 137:4920-4923. doi:http://dx.doi.org/10.1021/jacs.5b01613.

Yaghi, O. M., Gándara, F., Furukawa, H. and Lee, S. 2014. "High methane storage capacity in aluminum Metal–organic frameworks" *Journal of the American Chemical Society* 136:5271-5274. doi:http://dx.doi.org/10.1021/ja501606h.

Yan, Z., Zi, G., Wang, Y., Chen, Y., Guo, Y., Yuan, F., Gao, W., Wang, Y. and Wang, J. 2015. "Catalytic hydrothermal conversion of carboxymethyl cellulose to value-added chemicals over metal–organic framework MIL-53(Al)" *Carbohydrate Polymers* 115:146-151. doi:http://dx.doi.org/10.1016/j.carbpol.2014.08.065.

Yerkesikli, A. G. 2013. "Adsorption of reformer off-gas on NaX zeolite and metal organic framework (MIL53(Al)): Equilibria and Kinetics" Doctoral Thesis, Chemical Engineering, Izmir Instute of Technology.

Yi, F.-Y., Li, J.-P., Wu, D. and Sun, Z.-M. 2015. "A Series of multifunctional metal–organic frameworks showing excellent luminescent sensing, sensitization, and adsorbent abilities" *Chemistry – A European Journal* 21:11475-11482. doi:http://dx.doi.org/10.1002/chem.201500595.

Zaman, S. F., Loughlin, K. F. and Al-Khattaf, S. A. 2015. "Kinetics of desorption of 1,3-Diisopropylbenzene and 1,3,5-Triisopropylbenzene. 2. diffusion in FCC catalyst particles by Zero Length Column method" *Industrial & Engineering Chemistry Research* 54:4572-4580. doi:http://dx.doi.org/10.1021/ie504963e.

Zhang, Z., Ji, H., Song, Y., Zhang, S., Wang, M., Jia, C., Tian, J.-Y., He, L., Zhang, X. and Liu, C.-S. 2017. "Fe(III)-based metal–organic framework-derived core–shell nanostructure: Sensitive electrochemical platform for high trace determination of heavy metal ions" *Biosensors and Bioelectronics* 94:358-364. doi:https://doi.org/10.1016/j.bios.2017.03.014.

Zhou, H.-C., Li, J.-R. and Sculley, J. 2012. "Metal–Organic Frameworks for separations" *Chemical Reviews* 112:869-932. doi:http://dx.doi.org/10.1021/cr200190s.

Zhou, M., Wu, Y.-n., Qiao, J., Zhang, J., McDonald, A., Li, G. and Li, F. 2013. "The removal of bisphenol A from aqueous solutions by MIL-53(Al) and

mesostructured MIL-53(Al)" *Journal of Colloid and Interface Science* 405:157-163. doi:https://doi.org/10.1016/j.jcis.2013.05.024.

Zhu, H., Wang, L., Jie, X., Liu, D. and Cao, Y. 2016. "Improved interfacial affinity and CO2 separation performance of asymmetric mixed matrix membranes by incorporating postmodified MIL-53(Al)" *ACS Applied Materials & Interfaces* 8:22696-22704. doi:http://dx.doi.org/10.1021/acsami.6b07686.

Zikánová, A., Bülow, M. and Schlodder, H. 1987. "Intracrystalline diffusion of benzene in ZSM—5 and silicalite" *Zeolites* 7:115-118. doi:http://dx.doi.org/10.1016/0144-2449(87)90070-4.

APPENDIX A

DETAILS ABOUT HYDROTHERMAL METHOD

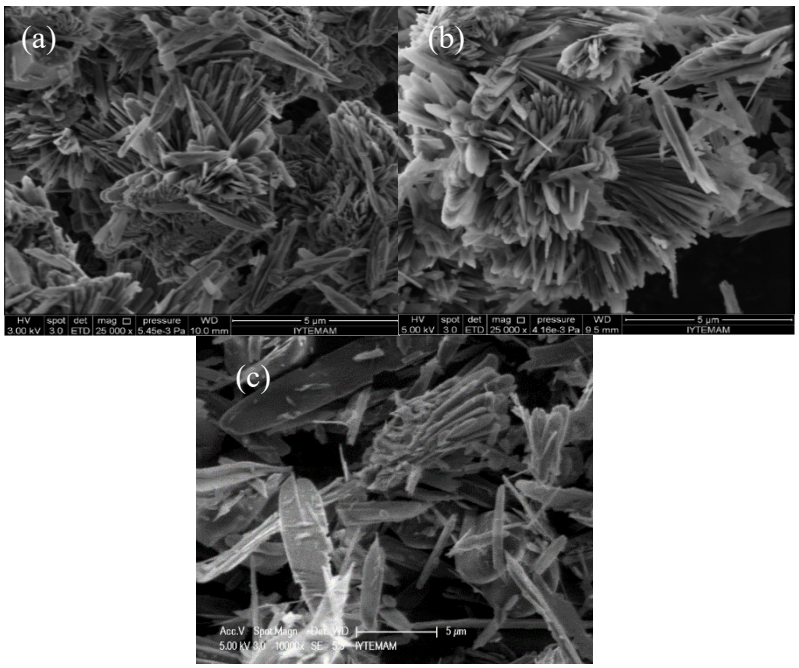

Figure A.1. SEM images of Al-TPAs synthesized by stirring for a) 1 h b) 3.5 h c) 5 h.

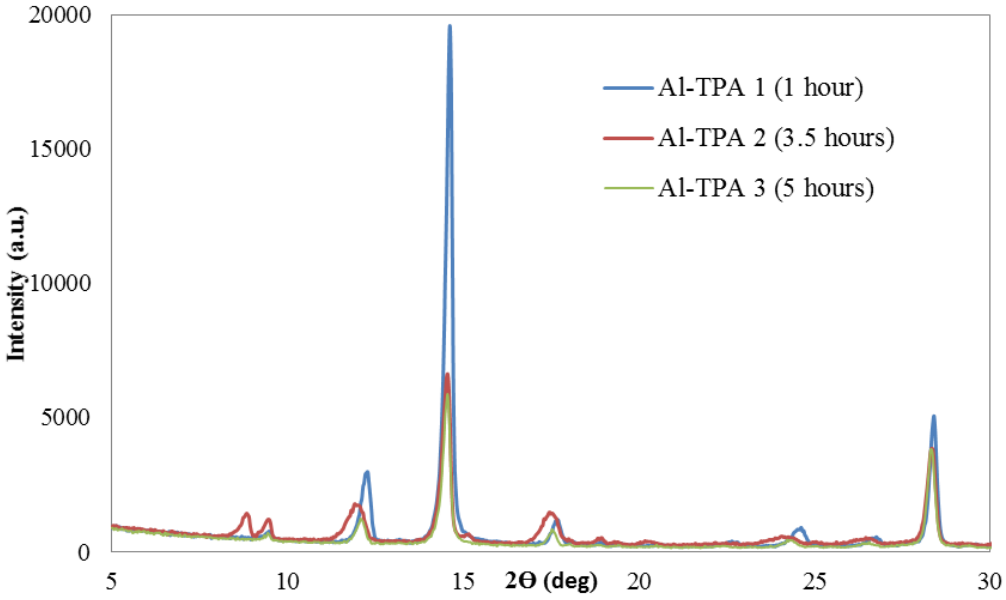

Figure A.2. X-ray diffractometer patterns for Al-TPAs synthesized by different stirring time.

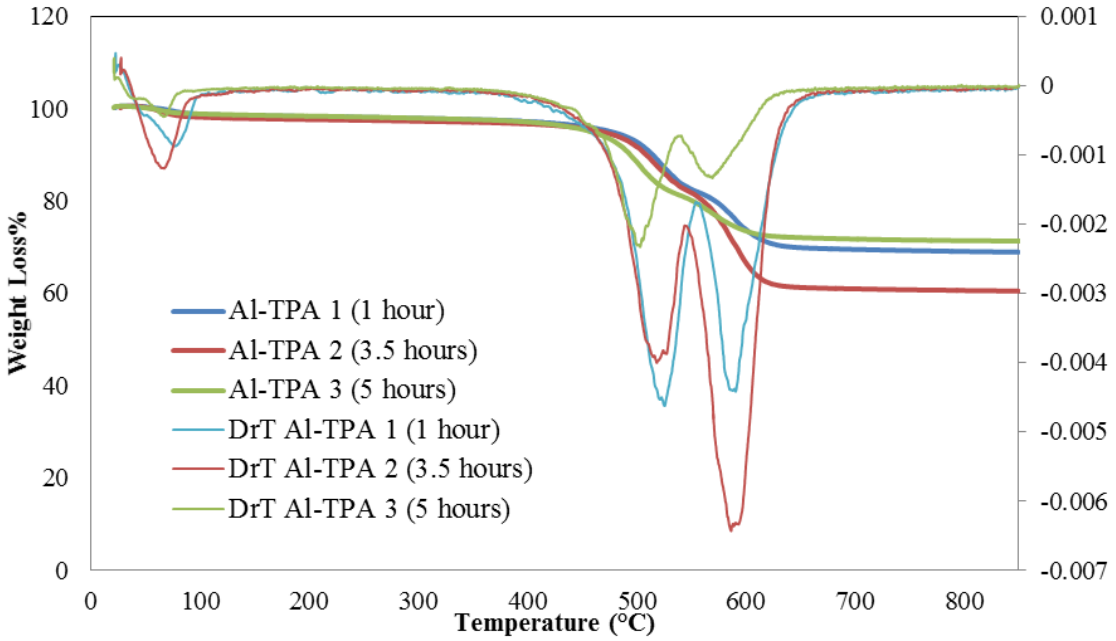

Figure A.3. Thermogravimetric curves for Al-TPAs synthesized by different stirring time.

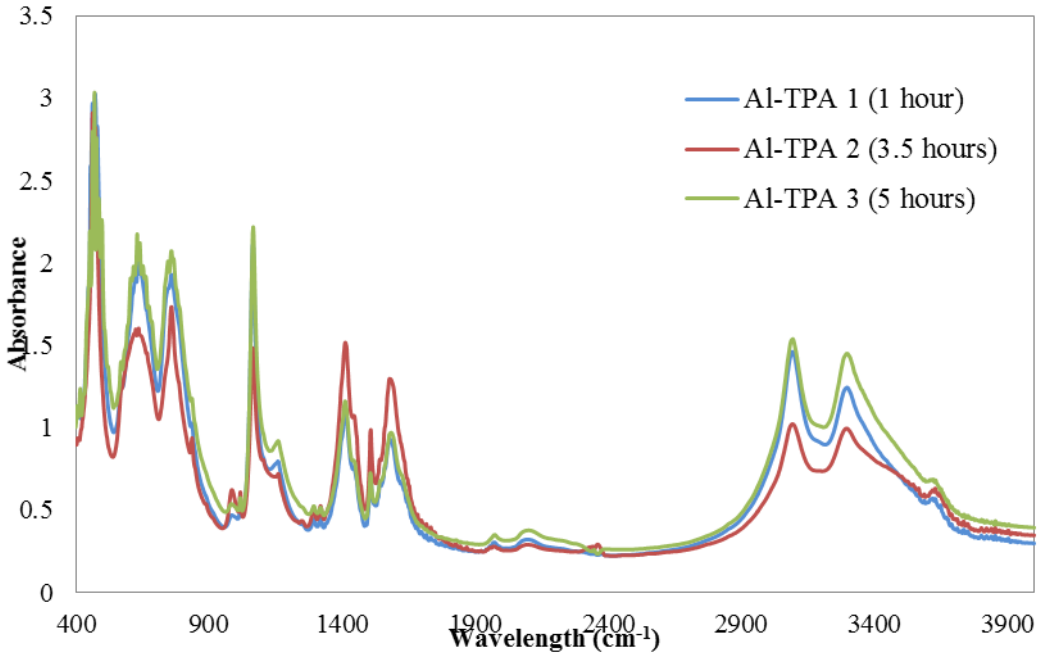

Figure A.4. FTIR spectra for Al-TPAs synthesized by different stirring time.

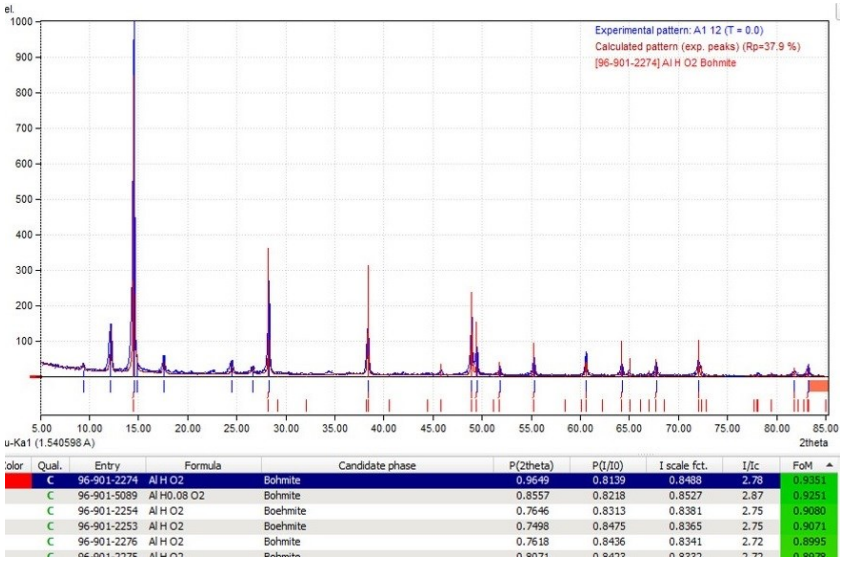

color	Qual.	Entry	Formula	Candidate phase	P(2theta)	P(I/I0)	I scale fct.	I/Ic	FoM
	C	96-901-2274	Al H O2	Bohmite	0.9649	0.8139	0.8488	2.78	0.9351
	C	96-901-5089	Al H0.08 O2	Bohmite	0.8557	0.8218	0.8527	2.87	0.9251
	C	96-901-2254	Al H O2	Boehmite	0.7646	0.8313	0.8381	2.75	0.9080
	C	96-901-2253	Al H O2	Boehmite	0.7498	0.8475	0.8365	2.75	0.9071
	C	96-901-2276	Al H O2	Bohmite	0.7618	0.8436	0.8341	2.72	0.8995

Figure A.5. X-ray diffractometer pattern of boehmite adopted from MATCH! Database

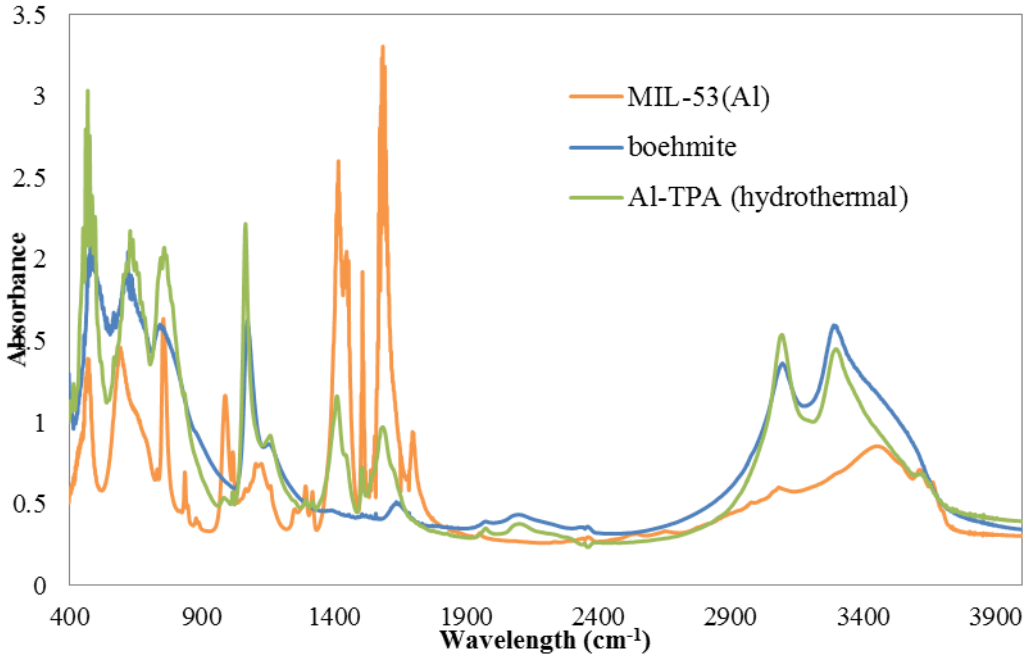

Figure A.6.The comparison of FTIR spectra of boehmite, synthesized Al-TPA and MIL-53(Al).

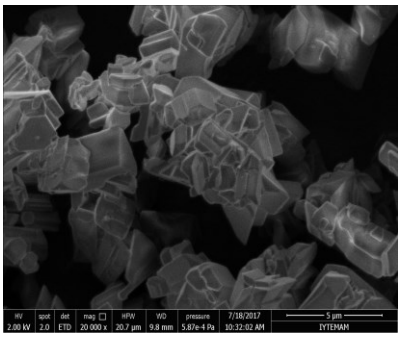

Figure A.7. SEM images of Al-TPA with precrystallization step.

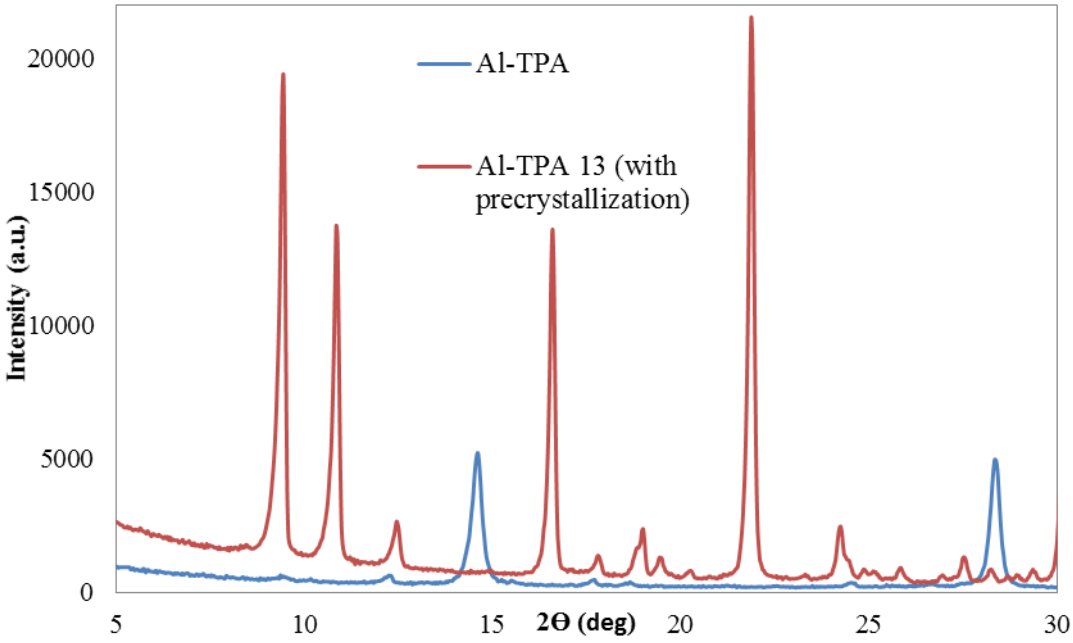

Figure A.8. X-ray diffractometer patterns of Al-TPA with precrystallization step.

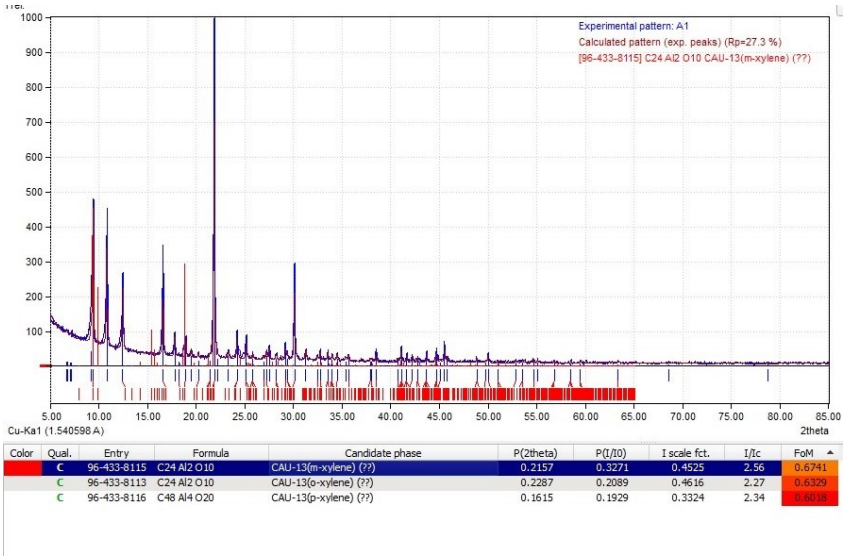

Figure A.9. X-ray diffractometer pattern of CAU-13 adopted from MATCH! Database

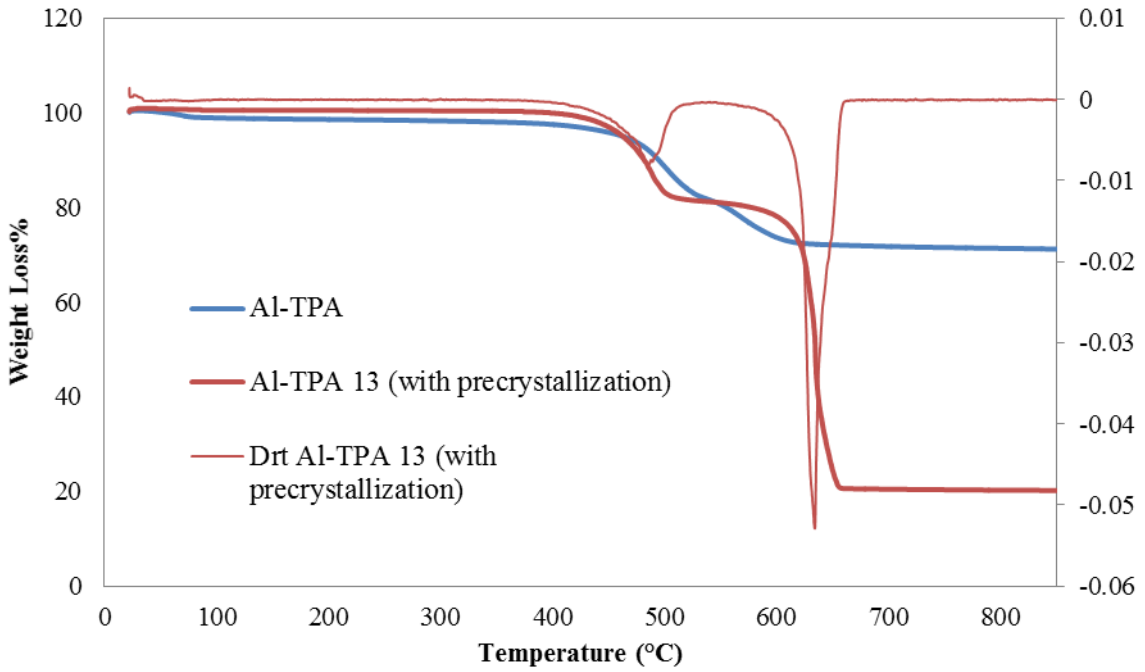

Figure A.10. Thermogravimetric curves of Al-TPA with precrystallization step.

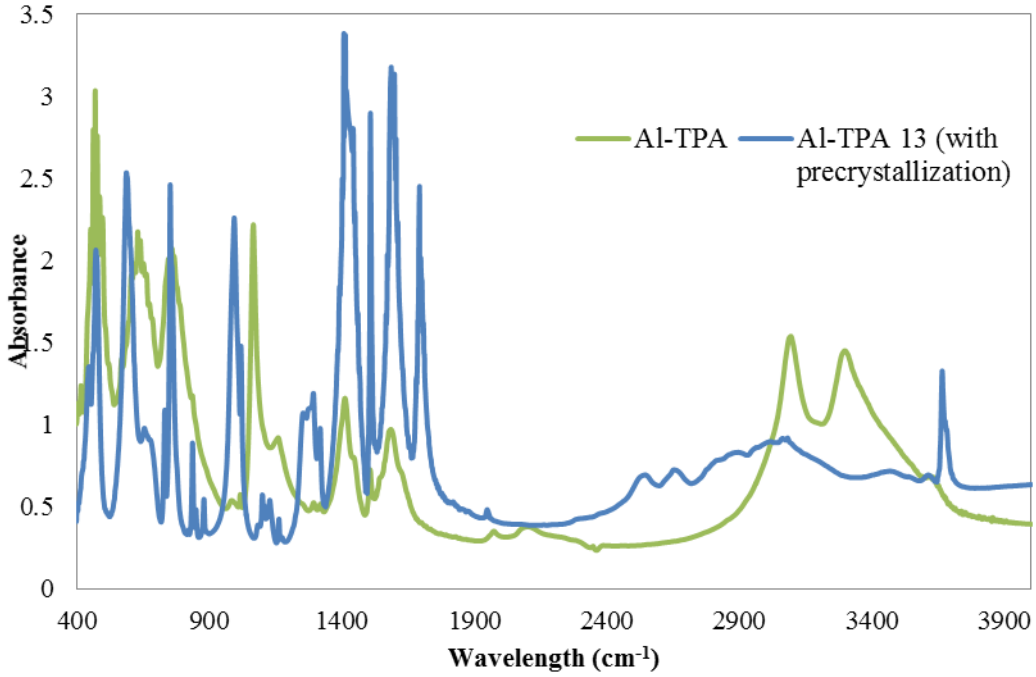

Figure A.11. The comparison of FTIR spectra of Al-TPA with precrystallization step.

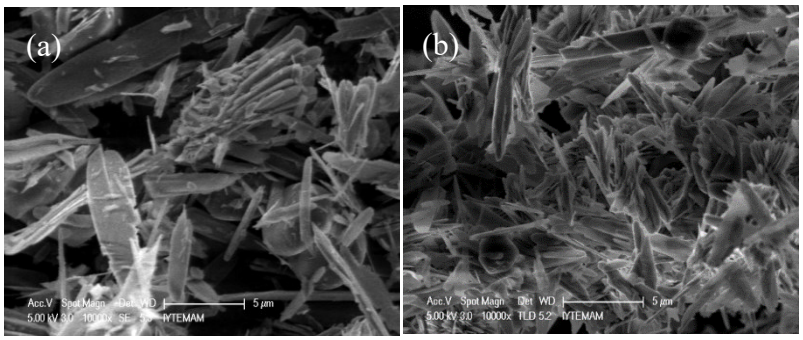

Figure A.12. SEM images of Al-TPAs washed with a) 5 times b) 10 times water.

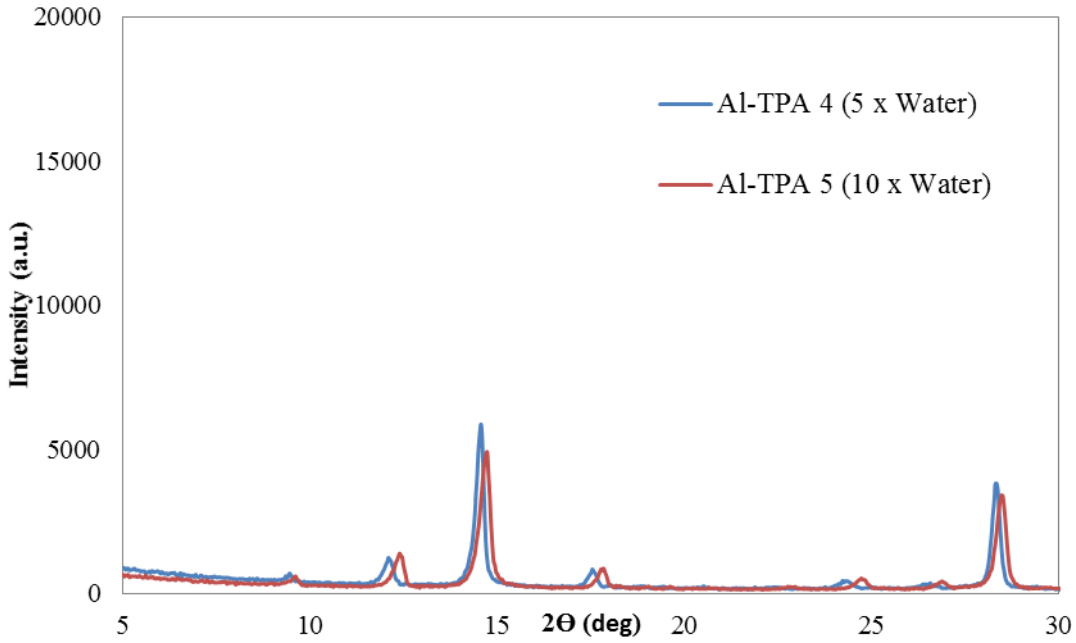

Figure A.13. X-ray diffractometer patterns of Al-TPAs washed with 5 times and 10 times water.

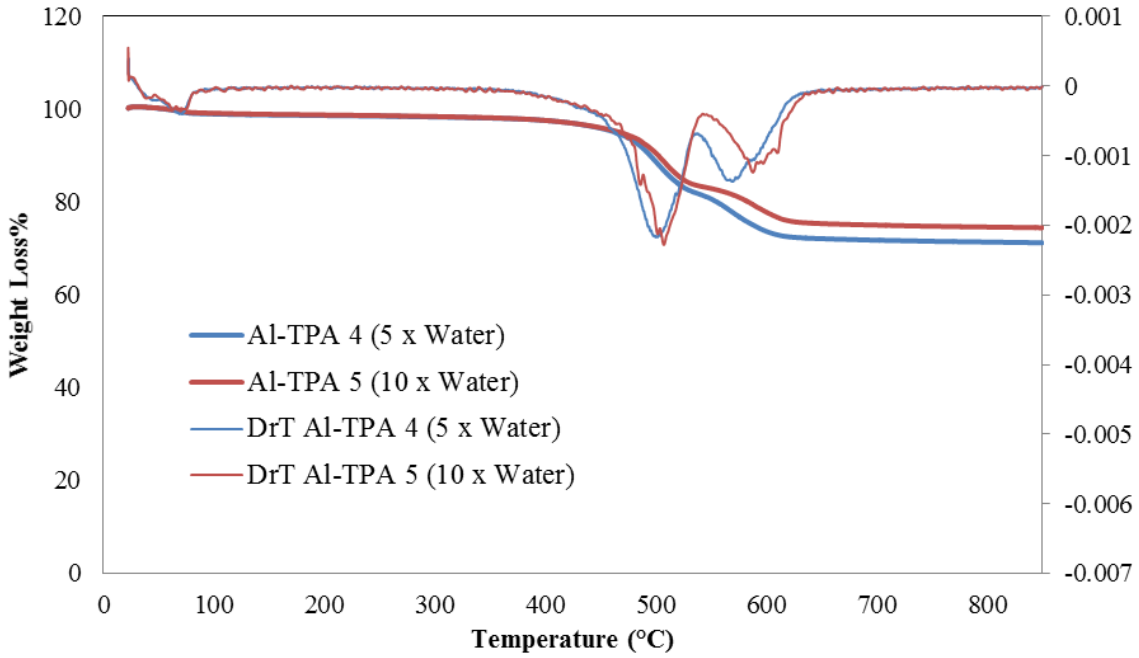

Figure A.14. Thermogravimetric curves of Al-TPAs washed with 5 times and 10 times water.

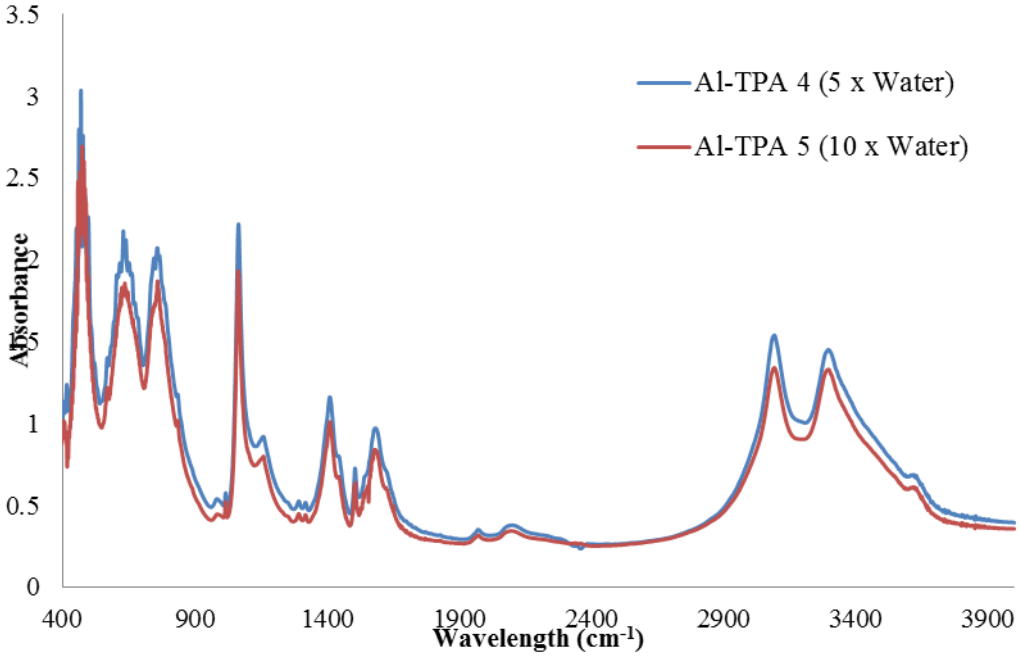

Figure A.15. FTIR spectra of Al-TPAs washed with 5 times and 10 times water.

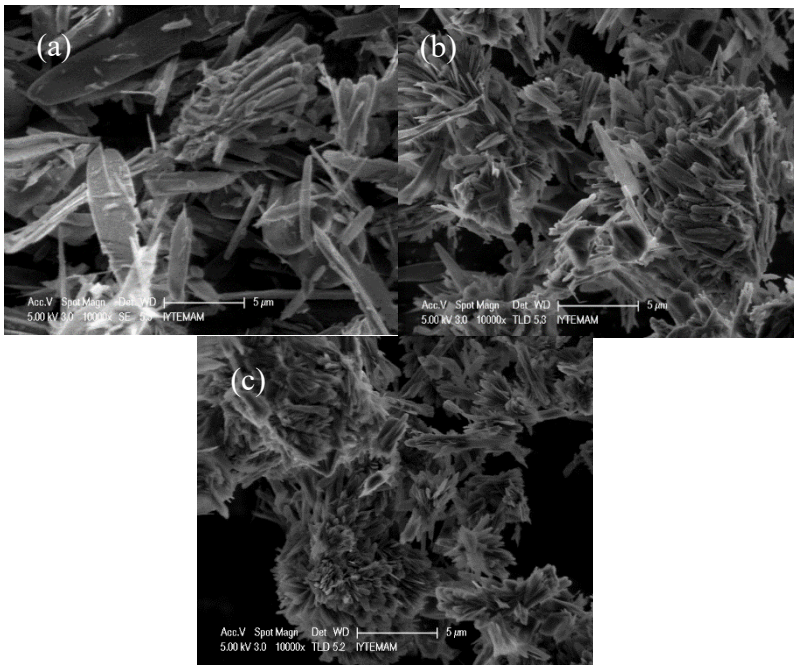

Figure A.16. SEM images of Al-TPAs washed with a) 5w, b) 5w/1d/2hd/2m and c) 5w/1d/2hd/2m/2m.

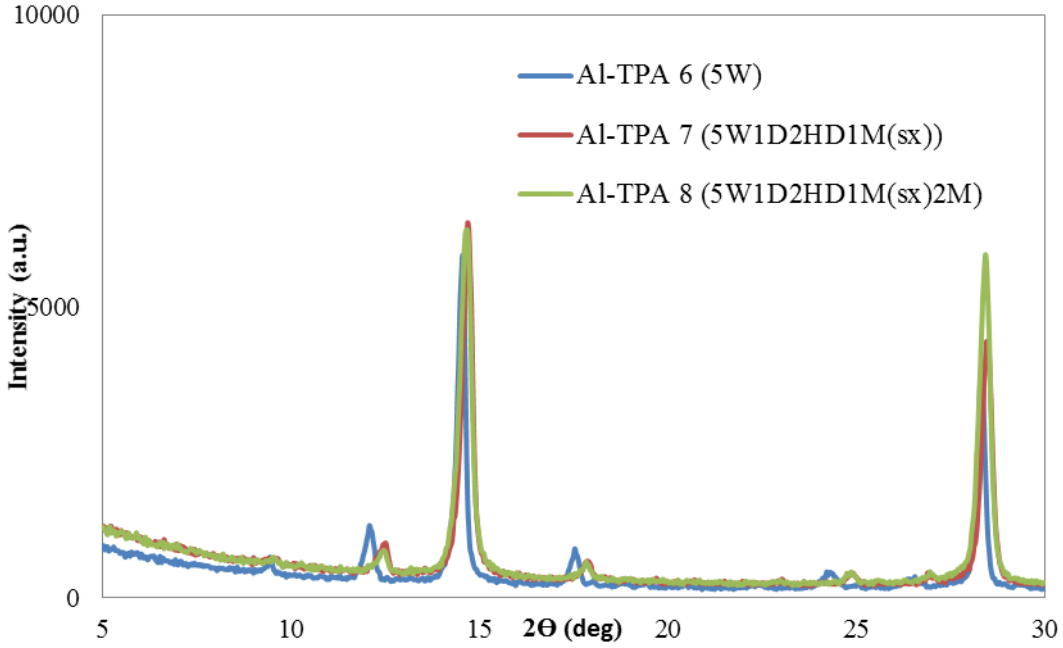

Figure A.17. X-ray diffractometer patterns of Al-TPAs washed with 5w, 5w/1d/2hd/2m and 5w/1d/2hd/2m/2m.

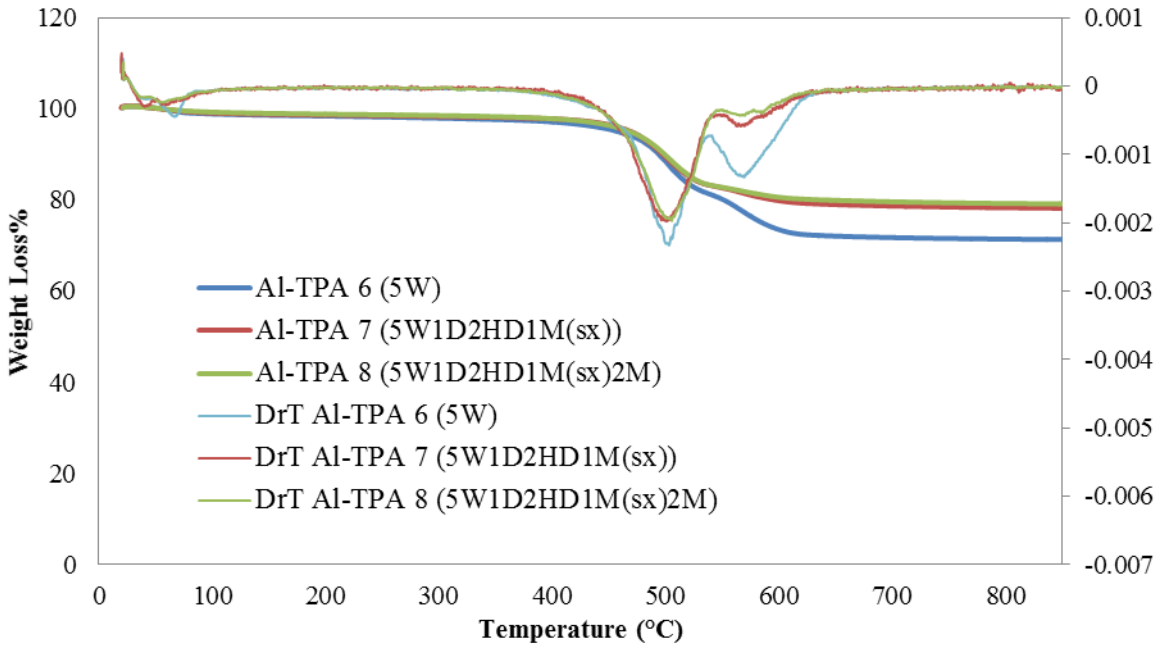

Figure A.18. Thermogravimetric curves of Al-TPAs washed with 5w, 5w/1d/2hd/2m and 5w/1d/2hd/2m/2m.

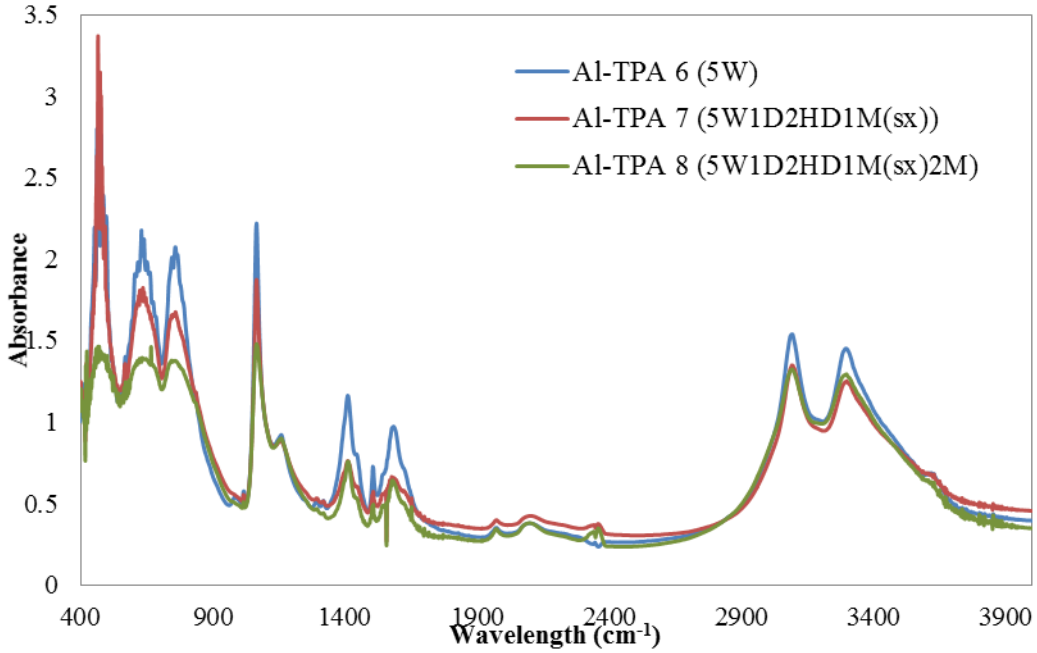

Figure A.19. FTIR spectra of Al-TPAs washed with 5w, 5w/1d/2hd/2m and 5w/1d/2hd/2m/2m.

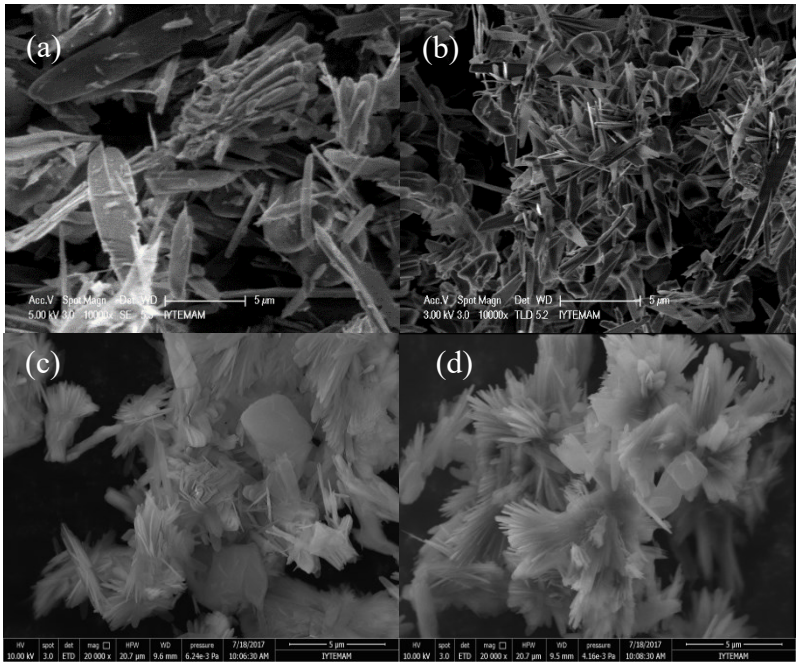

Figure A.20. SEM images of Al-TPAs activated at a) 330 b) 360 c) 410 and d) 420 °C.

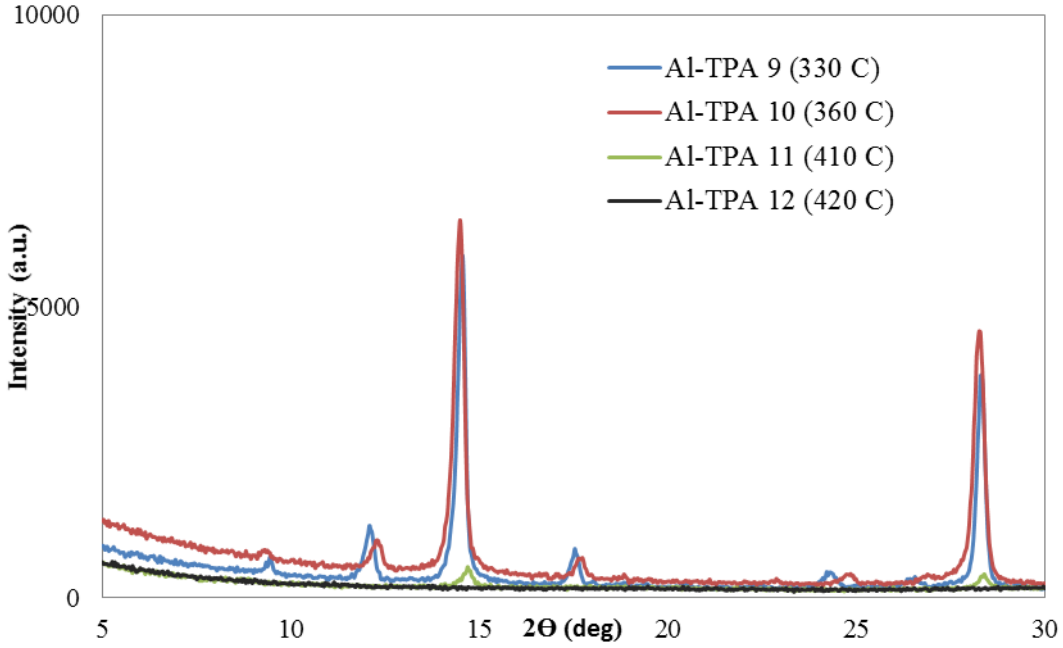

Figure A.21. X-ray diffractometer patterns of Al-TPAs activated at 330, 360, 410 and 420°C.

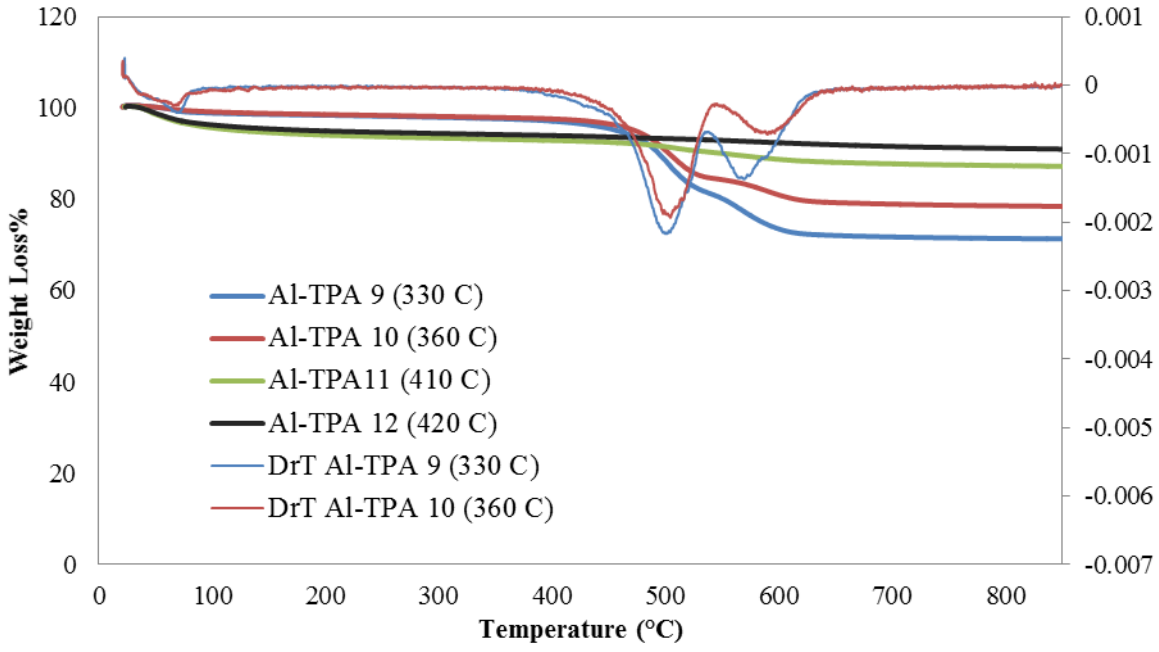

Figure A.22. Thermogravimetric curves of Al-TPAs activated at 330, 360, 410 and 420°C.

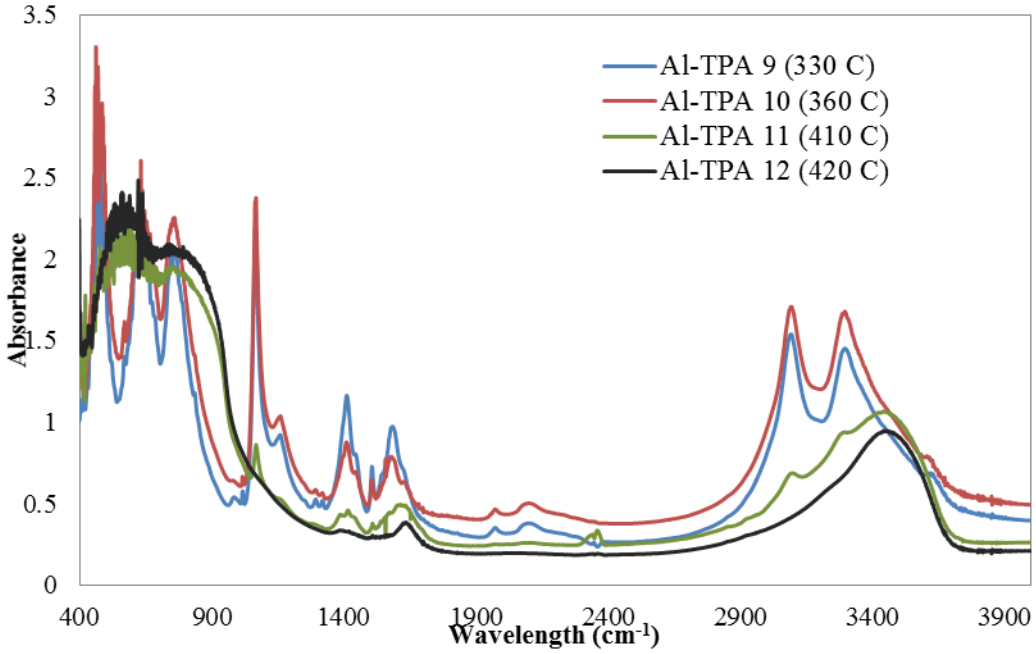

Figure A.23. FTIR spectra of Al-TPAs activated at 330, 360, 410 and 420°C.